# AN INVESTIGATION OF TWO BIOLOGICAL SOURCES CONTRIBUTING TO SIGNAL LOSS IN THE IMPLANTED BRAIN

By

Bhavna Gupta

A DISSERTATION

Submitted to
Michigan State University
in partial fulfillment of the requirements
for the degree of

Neuroscience – Doctor of Philosophy

2025

## ABSTRACT

Implantable electrodes have gained popular attention in research and clinical settings to treat and study a variety of neurological conditions. Detection of electrical and chemical signals drive the performance of implanted microelectrodes used for sensing and/or stimulating brain activity. However, signal instability and device failure over time in the implanted brain inhibit the therapeutic and biomedical promise of such microelectrodes. As the field of neurotechnology moves towards next-generation probes and sophisticated methodologies to improve signal detection in the brain, detailed explorations of the inherent biological response to implanted electrodes are warranted. The foreign body reaction to implanted probes can change over acute and chronic durations while experiencing structural, functional and genetic changes at the tissue level. Further, mechanical factors (for example, device material, flexibility, dimensions, etc.) can exacerbate or mitigate the inflammatory response, signal detection and overall integration of the device-tissue interface. This dissertation recognizes the diverse nature of the tissue response to implanted microelectrodes and conducts a deeper investigation of two biological sources contributing to signal loss – (1) protein adsorption, or biofouling, and (2) cellular encapsulation. The findings expand on – (1) assessments of a novel all-diamond boron-doped diamond microelectrode to tackle signal instability influenced by protein adsorption, and (2) gene expression changes brought about by cellular encapsulation of implanted devices. The results discussed herein take an interdisciplinary approach to investigate the biological sources influencing signal detection and employ numerous techniques including fast-scan cyclic voltammetry, electrophysiology and spatial transcriptomics. Overall, this work adds to the growing body of literature reporting on the basic science understanding of the multifaceted biological response to implantable microelectrodes.

This dissertation is dedicated to my family, friends, colleagues, and all those who support scientific inquiry. I specifically dedicate this dissertation to my parents, Baveen and Indranil Gupta, without whom I would not be where I am, and to my brother, Arjan Gupta, who has always appreciated the intricacies of science, and taught me to do so as well. I also dedicate this work to my amazing partner, Bradley Hunt, for endlessly supporting all my endeavors.

## ACKNOWLEDGEMENTS

I am extremely grateful to have the guidance and mentorship of my academic advisor, Dr. Erin Purcell, without whom I would not be where I am today. Dr. Purcell is a wise and elegant scientist, and it has been one of my greatest honors to learn from her academically and personally. She has remained reliable, supportive, steadfast and present throughout my journey as a graduate student, providing me with the help and resources that have shaped my capabilities as a scientific researcher. Time and again, she has placed my well-being and progress above all else, and I am profoundly grateful of her unwavering encouragement and compassion. I am deeply thankful for the opportunities she has provided me, and being part of her team has been one of the most cherished experiences of my life.

I would like to thank Dr. Caryl Sortwell, Dr. Greg Swain and Dr. Wen Li for their time serving on my graduate committee and providing expert advice, resources and insight. Their efforts, collaborations, and own works, have been foundational to my academic pursuits and the completion of this dissertation. I would also like to thank Dr. James Siegenthaler, whom I consider another mentor, for his time and dedication toward the diamond project, and for teaching me the skills to carry out fast-scan cyclic voltammetry as well as the many basics of electrochemistry. Dr. Siegenthaler is a brilliant and careful scientist, and I am very grateful to have had his expert guidance early-on in my graduate career. I would like to thank Dr. Alfred Robison, as well as the Neuroscience and Biomedical Engineering Programs at Michigan State University, for supporting and assisting my academic journey. I want to thank Dr. Romana Jarošová for her excellent mentorship, friendship and support prior to, and during my time as a PhD student. I also want to thank all my past and present lab members, with whom I have laughed, cried and shared countless memories that I will always cherish.

In 2022, our research group prepared a short report on the "Waveform Development for Neurotransmitter Detection on Novel Boron-Doped Diamond Microelectrodes" (doi: 10.1109/NER52421.2023.10123806) which was published as part of the at the *11th International IEEE/EMBS Conference on Neural Engineering (NER)*. This provided the groundwork for our comprehensive study published in April 2023 as "In Vitro biofouling performance of boron-doped diamond microelectrodes for serotonin detection using fast scan-cyclic voltammetry" (doi: 10.3390/bios13060576) in *Biosensors*. For these studies, I would like to thank the key efforts of Mason Perillo for experimental help, and Dr. James Siegenthaler for insightful feedback and conceptualization of the work. I would also like to sincerely thank the diamond fabrication team members at Fraunhofer USA Center Midwest – Coatings and Diamond Technologies Division. Recently, we have compiled and submitted another manuscript titled "All diamond boron-doped diamond microelectrodes for neurochemical sensing with fast scan-cyclic voltammetry", currently under peer-review for publishing. For this, I would like to thank Brandon Kepros for assistance with experiments and data collection.

In 2024, we were invited to publish a review article titled "Structural, functional and genetic changes surrounding electrodes implanted in the brain" (doi: 10.1021/acs.accounts.4c00057) in *Accounts of Chemical Research*. For this, I would like to thank the efforts from all of my past and present lab members. Currently, I am working on a large dataset of spatial transcriptomics of the device-tissue interface for novel biomarker identification via computational approaches. Here, I would like to acknowledge the prior findings and contributions by Dr. Quentin Whitsitt, whose work and legacy will continue to inspire us. I would also like to thank Dr. Akash Saxena, Anirban Chakraboty, and Dr. Michael Moore for their ongoing efforts and assistance with the computational approach to analyze the large datasets generated by spatial transcriptomics. I also want to thank Dr.

Melinda Frame, and the Center for Advanced Microscopy (CAM) at the Michigan State University, for aiding with tissue imaging. I would like to express my gratitude toward Dr. Maria Waselus, and the University of Michigan Advanced Genomics Core, for their assistance with RNA-sequencing and data analysis.

## TABLE OF CONTENTS

# CHAPTER 1 | TOWARDS NEXT GENERATION SENSORS: INTRODUCTION TO IMPLANTABLE ELECTRODES AND SIGNAL DETECTION

## 1.1 INTRODUCTION

Identification of neural communication, electrical and chemical in nature, as well as methods to detect brain signals have guided tremendous progress with implantable probes since the 20th century. Modern implantable neurotechnology faces newer challenges involving signal instability and device longevity that limit the clinical potential of stimulating and detecting probes to study and treat neurological conditions. This chapter discusses the history and recent developments in neurotechnology, with a focus on the underpinnings of robust methods to detect electrical and chemical signals in the brain. Later sections discuss various types of devices that are widely employed in the field for signal detection and introduce the topic of study in this dissertation: the biological response to implanted electrodes as a major, multifaceted challenge hindering device performance in acute and chronic brain implantation.

## 1.2 OVERVIEW OF IMPLANTABLE NEUROTECHNOLOGY: HISTORY AND RECENT DEVELOPMENTS

The concept of bioelectricity pre-dates the 1700s, when it became apparent that certain species of fish can generate voltage pulses, such as the cat fish from the Nile River in Ancient Egypt and the electric ray in the Mediterranean Sea[1,2]. In the 17th and 18th centuries, the existence of electric currents was known, but not fully understood, through experiments by early scientists including William Gilbert, who coined the term “electricity” and used lodestone therapy to treat pain or mental conditions. Pieter van Musschenbroek invented the Leyden jar,[1] a rudimentary charge storage device later used by Jean Jallabert to demonstrate electrical stimulation of muscle fibers. Benjamin Franklin’s work likewise demonstrated that electricity can be used to stimulate

muscle fibers[1]. By the 1800s, research by Luigi and Lucia Galvani, and Alessandro Volta, led to a deepening understanding of bioelectricity: Volta infamously self-stimulated the perception of sound through voltage applied to wires inserted in his ears[1,3]. Andre Marie Ampere studied the magnetic force between two electric currents, and Michael Faraday coined the phrases "ions", "anions" and "cations" while investigating electrolysis[4]. Faraday discovered electromagnetic induction in the following years, laying the groundwork for electromagnetism as well as modern day neurostimulation[1]. By late-1880, Richard Caton used a galvanometer to record electrical impulses in the brains of apes and rabbits[3], and Walter Nernst demonstrated that electric potentials arise from the diffusion of electrolytes in a solution[4]. These early inventions paved the way for more sophisticated developments in neurotechnology in the following decades.

The 20th century saw a remarkable emergence of methods for recording signals in the brain and furthering the basic understanding of neurophysiology on a cellular scale, despite periods of conflict and significant geopolitical developments. In 1924, Hans Berger recorded electrical signals from the human brain using an electroencephalogram (EEG)[5,6]. Alan Hodgkin and Andrew Huxley, founders of electrophysiology, published a first short report on the action potential (i.e. the electrical properties that govern how a nerve cell communicates or transmits signals to other cells or tissues) recorded in the giant axon of a squid in 1939[7]. After a decade, Hodgkin and Huxley continued their work by developing a voltage-clamp technique to study ionic movements, previously proposed in the "membrane hypothesis" by Julius Bernstein[4], as a basis of bioelectric potentials[7–9]. The Hodgkin-Huxley model quantitatively described the action potential in terms of voltage-gated permeabilities of the cellular membrane to sodium and potassium: their intuition that voltage-gated "particles" controlled the membrane potential laid the foundation for modern-day understanding of ion channel function. Their work, for which they shared the 1963 Nobel Prize in

Physiology or Medicine with synaptic physiologist John Eccles, revolutionized the field of neuroscience and physiology. Around this time, pioneering work by Ralph N. Adams resulted in the development of fast-scan cyclic voltammetry (FSCV), first introduced by Julian Millar in 1980[10], to record chemical signals in the brain. Mark Wightman popularized the method in 1988[11] as a powerful tool for real-time neurochemical detection. Meanwhile, building on the Hodgkin-Huxley model, Erwin Neher and Bert Sakmann created the patch-clamp technique enabling direct measurement of currents in single ion channels[12]. A notable tool during this time that facilitated most of these techniques and future implant work was the construction of wire electrodes encased in a glass micropipette.

Initially used in plant cells, and eventually in animal cells, the glass micropipette underwent numerous inventions, advances, regressions and evolutions as an electrode by multiple prominent scientists throughout the early 1900s. In 1947, Gilbert Ning Ling advanced prior work on the glass micropipette and produced the Gerard-Graham-Ling microelectrode (filled with salt solutions, often KCl) for precise measurements of electrical potentials in living cells[13]. Dowben and Rose (1953) filled the glass micropipette (tip diameter 10 μm) with wetting metals (such as gallium and indium) and electrodeposited platinum on the microelectrode tip to detect extracellular recordings in the thalamus of a cat[14]. Improving the mechanical durability of the glass micropipette, David Hubel (1956) made the first microwire-based microelectrode using tungsten as an easily prepared, sturdy implantable device to record single-unit action potentials from regions in the cat spinal cord, brain stem and cerebral cortex for up to 1 hour[15]. Shortly after, Strumwasser developed the first microwire bundle (or microelectrode array) composed of four to six stainless-steel insulated wires that was chronically implanted to record signals for up to one week in the reticular formation of hibernating squirrels[16]. These major advancements sparked a renaissance in neurotechnology,

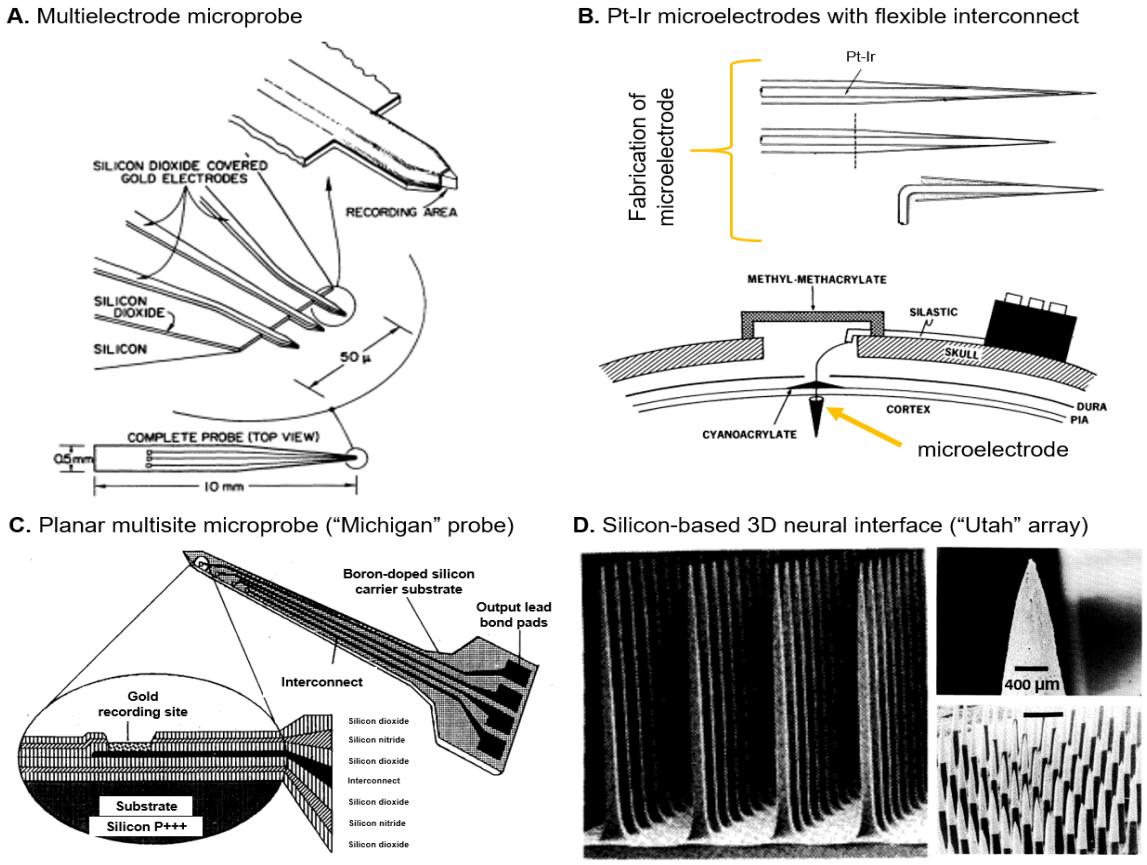


**Figure 1.1.** Early devices developed for cortical signal recordings. **A.** First multielectrode microprobe fabricated using micromachining (integrated-circuit) techniques reported by Wise et al. © 1970 IEEE[18]. **B.** Platinum-Iridium (Pt-Ir) glass microelectrodes with a flexible interconnection for cortical neuron recordings by Salcman et al. © 1973 IEEE[19]. **C.** Initial development of the modern-day silicon Michigan-style probe by Drake et al. © 1988 IEEE[22]. **D.** Initial scanning electron micrographs of the modern-day Utah array as a "three-dimensional" silicon-based electrode array by Campbell et al. © 1991 IEEE[26].

uncovering novel insights into the nervous system and igniting interest in the potential of implantable electrodes and devices.

In subsequent years, implantable probes with improved geometries, fabrication and materials were of particular interest to increase the duration, quality and processing of signal recording in animal models. Microwire arrays containing nichrome wires could record signals for 7 days in the rat hippocampus and midbrain tegmentum, and tungsten microelectrodes could record

spike potentials for up to one month in the cat hypothalamus[17]. In 1970, Wise et al. reported on the first multielectrode microprobe on a silicon substrate using integrated-circuit fabrication, or micromachining techniques (**Figure 1.1A**)[18]. Soon after, platinum-iridium (Pt-Ir) microelectrodes with a flexible interconnection from the device to the connector were developed as a first attempt to withstand cortical movements and maintain signal viability in the cat cortex (**Figure 1.1B**)[19]. These microelectrodes were later technically refined (based on mathematical modeling of the electrode tip motion relative to brain-skull displacement) for reproducibility and mass manufacture by utilizing pure gold wire, gold plating and parylene-C coatings in the fabrication process[20]. Schmidt et al. implanted 12 of these refined chronic microelectrodes in the motor cortices of monkeys to record single unit data for up to ~7 months[21]. In 1988, Drake et al. published a first report on a planar multisite microprobe, now known as the Michigan probe, developed using thin-film technology and micromachining on a silicon substrate to allow for simultaneous recordings from multiple sites and depths when implanted in the rat motor cortex (**Figure 1.1C**)[22]. These were implanted in rats to reliably record brain signals for over a year by the early 2000s[23,24]. Shortly after the first account of the Michigan probe, the Normann group at the University of Utah reported on 100-silicon needle type-electrodes arranged in a 10 x 10 array (**Figure 1.1D**) with a glass/silicon base offering superior mechanical strength and electrical properties[25,26]. This is now known as the Utah array, a popular choice in the clinical setting for signal recording in the human brain, especially in the BrainGate trials[27–29].

The 20$^{th}$ century breakthroughs in device fabrication and manufacturing techniques have shaped neuroscientific research and laid the basis for many present-day neurotechnology-driven ventures and enterprises. A type of Utah array, NeuroPort Array[30] manufactured by Blackrock Neurotech, has been tested to record signals in the human brain since 2004, and has received

commercial FDA approval. Synchron utilizes a stentrode device[31], an electrode array to sense motor signals within blood vessels, that is also FDA approved for human clinical trials as a brain-computer interface (BCI) to detect neural signals and allow control of assistive technology. NeuroNexus was launched in 2004 by leaders involved in developing the Michigan silicon probe, and provides cutting-edge neuroscientific tools designed for research purposes[32]. More recent start-ups that have attracted attention towards neuroscience tools and implant development include Paradromics[33], Neuralink[34], and Precision Neuroscience[35] for BCIs to restore human capabilities for those living with neurological conditions, and Flow Neuroscience[36] for mental health illness treatment using transcranial Direct Current Stimulation (tDCS).

Today, implanted electrodes are widely being used to study brain function in clinical and research settings. The application of neural implants in the central nervous system has created new treatment strategies for numerous medical conditions including Parkinson's disease (PD), paralysis, Alzheimer's disease, Tourette's syndrome, obsessive compulsive disorder, depression, deafness, tinnitus, chronic pain or stroke[37–49]. Symptomatic treatment of such disorders can employ closed-loop systems, which condition electrical stimulation on detected signals[50]. The adaptive power of closed-loop systems has driven new advances for rehabilitation of movement disorders such as PD, essential tremor and dystonia: for example, deep brain stimulation can be controlled by activity recorded in the motor cortex[51,52]. Likewise, recorded neural activity from brain implants can be decoded and used to control assistive technologies for restorative and rehabilitative therapies for paralyzed patients[53,54].

## 1.3 METHODS OF RECORDING SIGNALS FROM THE BRAIN

Several techniques have been developed to record signals from the brain *in vivo* and *in vitro*, most of which can be grouped into the following broad categories – (1) Electrical activity

recording, for example, electrophysiology, electroencephalography (EEG), electrocorticography (ECoG), and magnetoencephalography, (MEG); (2) Electrochemical detection methods, such as amperometry and FSCV; (3) Nuclear medicine tomographic imaging, such as positron emission tomography (PET) and single-photon emission computed tomography (SPECT); (4) Optical sensing techniques and optical fiber based sensors (fiber photometry), surface-enhanced Raman spectroscopy, fluorescence, chemiluminescence, and colorimetry; and (5) Microdialysis with coupling methods such as high-pressure liquid chromatography (HPLC). Considering applicability to the research discussed in future chapters, this work will expand on two main approaches of detecting brain signals - (I) electrical signaling (electrophysiology), and (II) chemical signaling (electrochemical detection methods of amperometry, cyclic voltammetry, and FSCV). Detailed information on other categories can be found in the reviews by Niyonambaza et al (2019)[55] and Wu et al. (2018)[56].

### 1.3.1 ELECTRICAL SIGNALING (ELECTROPHYSIOLOGY)

Electrophysiology refers to the study of how electrical signals are generated and propagated to influence the activity of neurons, muscles, and other tissues. These electrical signals are essential for everyday brain and bodily functions, governing our abilities as humans. At the simplest level, neurons are considered excitable cells, having the ability to generate and propagate electrical signals. This excitability is facilitated mainly due to ions, channels, a polarizable membrane and action potentials. This section will briefly cover how each of these components contributes to electrical signaling.

*Ions & ion channels*: Sodium ($Na^+$), potassium ($K^+$), calcium ($Ca^{2+}$) and chloride ($Cl^-$) ions play crucial roles in moving across the cellular membrane through ion channels to elicit electrical signaling in the nervous system. Ion channels can further be considered excitable molecules

themselves that are responsive to a stimulus (for example, chemical or neurotransmitter presence, membrane potential change, mechanical or temperature change, etc.)[4]. This response is known as "gating", an important feature that allows the opening and closing of a pore based on the stimulus to enable selective permeability to the flow of certain ions. In electrophysiology, these gated ion fluxes can be studied as electric currents across the cellular membrane. The ion fluxes have an instantaneous effect on the overall potential of the membrane, thereby exciting other ion channels in the membrane and inducing a propagating effect. The classic work conducted by Hodgkin and Huxley in 1952 studied such ionic currents in the squid giant axon which led to the recognition of the Na and K channels[9]. Ever since, advances in electrophysiology and molecular genetics have enabled the identification of numerous different types of ion channels, genes encoding for these channels, and families or classes of channels with similarities[4]. Some commonly recognized types of ion channels present in neurons to aid electrical signaling include voltage-gated (Na, K, Ca, Cl), ligand-gated, mechano-sensitive, and cyclic nucleotide-gated channels.

*Polarizable membrane*: The membrane of an excitable cell is composed of a phospholipid bilayer that is conductive due to the ion channels embedded within the bilayer. Since these channels span the lipid bilayer, ion fluxes create electric currents which in turn influence the membrane potential overall. From a simplified biophysical perspective, charge carried in excitable cells via ions is similar to that in an electronic circuit[57], and follows the fundamental Ohm's Law that provides a relation between current (I), voltage (V) and resistance (R). Ohm's law defines that current passing through a conductor between two points is directly proportional to the V across the two points and inversely proportional to the R, and can be expressed as:

$$V = I \times R$$

Here, resistance is a reciprocal of conductance which is the measure of an ion channel's ability to move ions across itself. Ohm's law is central to membrane biophysics, or understanding how ion channels influence electrical properties of the cell membrane, since each channel acts as a small conductor enabling ions to move across the otherwise insulating lipid membrane. The electrical conductance of a membrane as a whole is dictated by the sum of all these elementary, small conductances. Additionally, the membrane of an excitable cell acts as a capacitor. The thin insulating bilayer separates external and internal conducting solutions i.e. divides intracellular components from the extracellular space. This makes the excitable cell membrane an efficient electrical capacitor, and determines how many ions must move across the membrane to make electrical signals.

*Action potential*: Prior to the discussion of an action potential, it is important to understand the excitable cell at rest, or equilibrium[58]. In general, all systems maintain and move towards equilibrium. The equilibrium potential of an excitable cell for a particular ion can be explained by the Nernst equation, proposed by Hermann Walther Nernst in the 1800s, to understand how each ion contributes to the overall membrane potential[4]. The Nernst equation was founded on the discovery that ions carrying charge can move across conducting solutions and generate potential or voltage differences. In electrophysiology, the Nernst equation can be applied as:

$$E_{ion} = \frac{RT}{zF} \ln \frac{[ion]_o}{[ion]_i}$$

Here, $E_{ion}$ is the equilibrium potential of the ion, $R$ is the universal gas constant, $T$ is the temperature in Kelvin, $z$ is the valence of the ion, $[ion]$ is the concentration of the ion, $o$ stands for outside of the cell, and $i$ stands for the inside of the cell. For a deeper discussion on the relation of the Nernst equation to equilibrium potentials in this context, refer to Chapter 1 of Hille 2001[4]. Yet, as discussed previously, the membrane potential is determined by more than one ion's movement

across the membrane. The Goldman-Hodgkin-Katz (GHK) Equation is an extension of the Nernst equation that accounts for the presence and movement of multiple ions across the membrane. The GHK equation adds to the Nernst equation by considering the permeabilities and concentrations of other ions involved[59,60]. For example, for each K, Na, and Cl ion concentrations, the GHK equation adds a term as such:

$$V_m = \frac{RT}{zF} \ln \frac{p_k[K^+]_o + p_{Na}[Na^+]_o + p_{Cl}[Cl^-]_o}{p_k[K^+]_i + p_{Na}[Na^+]_i + p_k[Cl^-]_i}$$

Here, the equation contains similar variables to the Nernst equation, except *Vm* is the membrane potential and $p_{ion}[ion]$ is the relative membrane permeability for the ion. Such mathematical equations and models quantitatively describe the fundamental ionic interactions and cellular processes that give rise to intracellular electrical signals (for more comprehensive quantitative explanations on intracellular events and understanding the Nernst equation, refer to Ion Channels of Excitable Membranes[4] and referenced articles[58,60–64]).

The resting membrane potential of a neuron is typically maintained between -85 mV and -60 mV relative to the outside of the cell. The more negative potential is mainly because more $K^+$ selective channels are open (compared to $Na^+$, $Cl^-$ or $Ca^+$ selective ions) at rest. When a stimulus triggering an action potential presents, the membrane potential becomes less negative as more ion channels open. The depolarization of a membrane must reach a threshold of ~55 mV for the action potential to occur; else, the neuron will not carry out an action potential (commonly known as all-or-none firing). Once the -55-mV threshold is reached, voltage-gated $Na^+$ channels open and allow an influx of $Na^+$ ions to rapidly depolarize the membrane to ~ +40 mV; this is known as the depolarization phase of an action potential (**Figure 1.2A**). As the system tries to restore equilibrium, voltage-gated $Na^+$ channels close and voltage-gated $K^+$ channels open for $K^+$ ions to leave the cell and repolarize the membrane; this is known as the repolarization phase (**Figure**

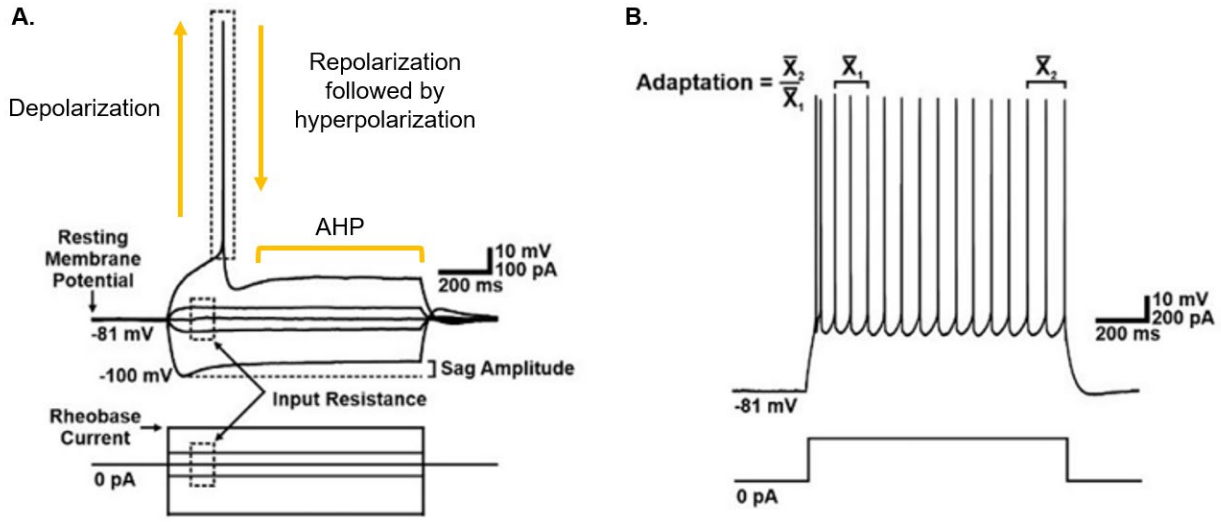


**Figure 1.2.** Intracellular action potential (AP) characteristics as recorded by whole cell electrophysiology. **A.** Singular action potential of a naïve deep layer pyramidal neuron in the rat motor cortex. Labels indicate widely recognized features that are used for calculating AP characteristics. **B.** Representative trace of burst firing of action potentials that can used to assess qualitative effects. Reproduced from Gregory et al. Copyright 2023.

**1.2A**). Few $Ca^+$ channels are involved during depolarization, but most are activated during repolarization where $Ca^+$ entry can also drive calcium-activated K channels (e.g. BK channels and SK channels)[65]. The continued efflux of $K^+$ ions temporarily hyperpolarizes the membrane to a more negative potential than the resting state, referred to as the hyperpolarization phase which is closely followed by an afterhyperpolarization (AHP) phase. During AHP, ion channels (such as the sodium-potassium pump) work to re-establish equilibrium and recover the resting membrane potential. The AHP can have fast, medium or slow components, and include a refractory period which prevents the firing of a subsequent action potential. However, in some neurons, an afterdepolarization can occur right after a fast AHP, where the membrane experiences a small depolarization which in turn can elicit subsequent action potentials, or all-or-none burst, if the threshold is reached[65] (**Figure 1.2B**).

Action potential firing is the process of transmitting electrical signals in the central nervous system. This electrical transmission is often studied as spiking activity in electrophysiology, and can be divided into two types – (1) intercellular electrical signaling (within a single neuron), and (2) extracellular electrical signaling (in the extracellular space, outside of neurons).

#### 1.3.1.1 INTRACELLULAR ELECTRICAL SIGNALING

Intracellular electrical recordings allow for highly precise measurements from a single cell using a microelectrode. Common types of intracellular electrical recording techniques include patch-clamp (having a whole-cell configuration enabling voltage-clamp & current-clamp modes), dynamic clamp, and sharp electrode recording. These techniques usually employ a glass micropipette containing a concentrated salt solution and a silver wire that is connected to an amplifier[4]. Experimentally, in the whole cell configuration of the patch-clamp technique, a ~1 μm mouth diameter pipette (resistance between 2 and 6 MΩ) is placed just outside the cell membrane with the amplifier zeroed. Positive pressure is applied to the pipette while advancing to come in contact with the cell membrane, and then released, to attach the pipette mouth to a "patch" of the cell membrane. This forms an initial low resistance (MΩ) seal that can be tightened to a higher resistance (GΩ) by negative pressure or light sucking. By steadily pulling the pipette out to the cell surface, and applying more negative pressure, the cell membrane can be ruptured to make the pipette solution continuous with the cell cytoplasm. In the current-clamp mode, a specific current amplitude can be injected through the experimental set up to record cellular excitability. Similarly, in the voltage-clamp mode, the membrane potential can be held at a user specified potential for the purpose of the study. By holding the membrane potential at a specific voltage, it is possible isolate and measure ionic currents such as excitatory post-synaptic currents (EPSCs) and inhibitory

post-synaptic currents (IPSCs). These post-synaptic currents are facilitated by applying a stimulus to a presynaptic neuron or by neurotransmitter binding at the recorded postsynaptic neuron.

Action potentials recorded via intracellular electrical signaling may consist of different shapes, rates, and firing patterns based on the distribution of ion channels and type of neuron[65]. The individual parts of an action potential and the anatomy of a spike can further be studied to provide insight into neuronal function and behavior. Gregory et al. (2023) assessed individual deep layer pyramidal neurons surrounding microelectrode arrays implanted in rat motor cortices using whole-cell electrophysiology which enabled an investigation of action potential (AP) characteristics (sag amplitude, AP maximum amplitude, AP threshold, etc.)[66] (**Figure 1.2**). Using current-clamp configuration, it was found that neurons surrounding devices showed reduced sag amplitude i.e. a lessened depolarizing response to a hyperpolarizing current stimulus, and increased spike frequency adaptation, i.e. widening of the interval between spikes during a sustained depolarizing current injection. Further, voltage-clamp recordings revealed a reduction in the firing frequency of spontaneous EPSCs in neurons surrounding devices that had been implanted for 6 weeks. In this way, intracellular electrical signaling enables measurements of action potentials, membrane potentials and synaptic potentials in single neurons to discover novel information about electrical signals and neurological states.

Pharmacological manipulations during intracellular signal recording is another powerful tool to uncover electrical function or dysfunction of excitable cells. It is known that certain marine toxins can disrupt the function of voltage-gated Na channels by inhibiting current flow or changing the activation and inactivation of gating processes. Consequently, these ligands can be employed by electrophysiologists in research and clinical settings targeted towards understanding neurophysiology and/or drug development[67].

#### 1.3.1.2 EXTRACELLULAR ELECTRICAL SIGNALING

Extracellular electrical recordings are taken from the extracellular space, usually outside of a neuron, and contain information from multiple neurons. As various cellular processes occur (e.g. ion fluxes, action potentials, etc.) and neuronal activities generate transmembrane currents, the extracellular space experiences a net potential change ($V_e$), relative to a reference potential, due to a combination of all the current changes in the electrical field[68]. All ionic processes in the brain, including slow changes in glia and explosive action potentials, generate currents that superimpose at any point in space to generate *Ve* at that location. When recorded by microelectrodes implanted in the brain, the low-frequency component of $V_e$ is referred to as the local field potential (LFP); however, recent advances have verified that this term is a misnomer as the LFP can propagate beyond the immediate local region[68,69]. LFPs recorded using a microelectrode array, such as the silicon Michigan probe, are visualized as slow oscillations obtained by low pass filtering (below ~300 Hz) of the raw neural signals. The LFP signal can be especially informative of population-scale synaptic activity, making this method a powerful form of studying electrogenesis.

Theoretically, the LFP waveform (amplitude, frequency and magnitude) largely relies on a number of factors within the broad categories of: (1) various extracellular current sources; (2) the architectural organization of the cellular-synaptic network, and; (3) the synchrony of current sources. Multiple current sources contribute to the LFP including synaptic activity, fast action potentials, calcium spikes, intrinsic currents and resonances, spike AHPs and “down states” (i.e. hyperpolarized states), gap junctions and neuron-glia interactions, and ephaptic effects[68]. The placement of the microelectrode relative to the current source (shorter distance yields a higher amplitude) also dictates the LFP waveform. Greater distances from the current source result in

spatially averaged, less informative LFP signals that include interferent or background currents. The magnitude, direction, spatial density as well as temporal coordination (synchrony) of individual current sources add to the electric field. Further, neuronal geometry and architecture are foundational to the network that contributes to extracellular electrical signals. Here, the morphology of neurons, i.e. shape and size, as well the organization, i.e. spatial alignment, influences the magnitude of the extracellular current. For example, pyramidal cells with long, apical dendrites generate strong dipoles that strongly contribute to the ionic flow of the extracellular space, whereas thalamocortical cells that are spherically symmetrical, with equally sized dendrites, generate small dipoles. Temporally synchronous changes in the membrane potential of groups of neurons also add to the magnitude of the extracellular LFP: this rhythmic firing of neurons gives rise to network oscillations that are associated with different LFP magnitudes and brain states (e.g. asleep, awake, aware, etc.).

Raw extracellular electrical signals recorded using a microelectrode array, such as the Michigan probe, can further be high-pass filtered (~above 300 Hz) to extract spikes[70]. Additional processing of the extracted spikes can differentiate between multi-unit activity (MUA) and single-unit activity (SUA)[70,71]. MUA represents all the detected spikes (or combined action potentials) generated by threshold crossing, but without spike sorting, from a collection of neurons in the vicinity of the implanted electrode. SUA can reflect the timing of action potentials fired by individual neurons and is obtained by threshold crossing with subsequent data processing techniques (spike sorting). MUA is less precise and reflects an aggregated view of a neuronal spiking activity over a period of seconds, while SUA shows the behavior of a single neuron over a period of milliseconds but requires complex analysis. A typical extracellular action potential of an individual unit (from the soma region) displays a waveform that is reversed in polarity in

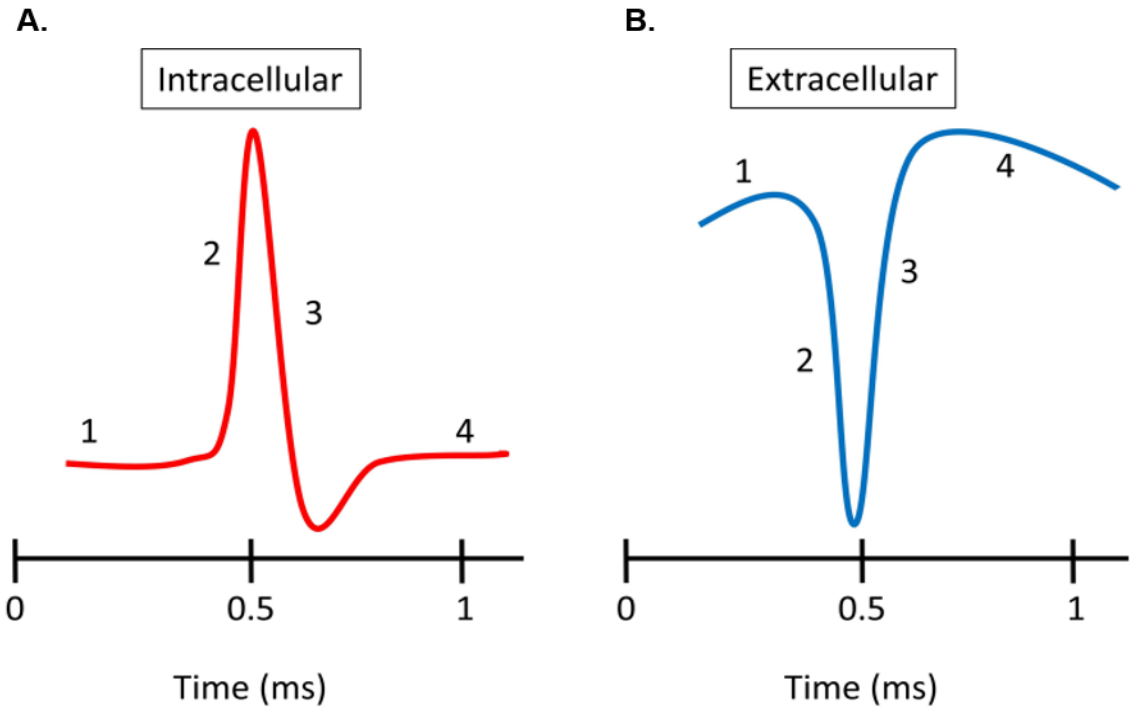


**Figure 1.3.** Waveforms of **A**. intracellular vs **B**. extracellular single unit spike signals. Both waveforms reflect the typical phases of an action potential labeled as: (1) at rest, (2) depolarization, (3) repolarization and (4) after-hyperpolarization. Reused from open-access by Jung et al.[71] Copyright 2023.

comparison to the waveform of a typical intracellular action potential[71] (**Figure 1.3**). Additionally, extracellular electrical signal recording techniques have a compelling advantage of sampling in awake, behaving subjects over long periods of time.

### 1.3.2 CHEMICAL SIGNALING (ELECTROCHEMICAL DETECTION)

Chemical signaling takes place via chemical messengers in the central nervous system (CNS), allowing nerve cells to communicate with other destination cells such as gland or muscle cells. Camillo Golgi, who created the Golgi stain in 1873, and Santiago Ramon y Cajal, who presented the neuron doctrine in 1888, were the first to introduce the complexity of neuronal maps and circuits that laid the basis for our modern understanding of chemical signaling[72]. These ideas were advanced by the prominent neurophysiologist Sherrington who established the term

"synapse" – the junction between two neurons where chemical or electrical signals are transmitted[72]. Ever since, deeper investigations into the nature of chemical signaling have provided insight into the presence of biogenic amines acting as neurotransmitters (chemical messengers), such as dopamine (DA) and serotonin (5-HT), and their widespread projections in the CNS. Further, it was found that chemical signaling was not only limited to neurotransmitter communication in the synapse, but also extended to the extracellular space, now termed volume transmission. Today, two widely recognized modes of chemical transmission are synaptic and volume transmission. Electrochemical detection methods are powerful techniques that employ the use of microelectrodes to study these modes of chemical transmission in the brain.

#### 1.3.2.1 AMPEROMETRY

Similar to other electrochemical detection methods, amperometry employs the use of an electrode to detect the oxidation and reduction of specific neurotransmitters. This method is better known as constant-potential amperometry as the electrode is held at the same potential to facilitate redox reactions, and generate currents based on mass transport[73]. The response currents are obtained as a function of time, and current integration typically gives the concentration of the electrolyzed analyte[74]. Amperometry is especially useful to analyze the kinetics of neurotransmitter release due to high temporal resolution dependent on the rate of data collection[73]. Initial chemical evidence for catecholamine exocytosis in chromaffin cells was found using amperometry and voltammetry by Mark Wightman and colleagues (1990)[75]. The high sensitivity of the technique allows exocytosis events to be captured as oxidative current spikes that provide quantitative and qualitative information about the nature of neurotransmitter release[73].

The constant-applied potential restricts amperometry to be used only with samples of specified and known components[73]. At a given voltage, all the electroactive species in an analyte

will be oxidized or reduced, thereby offering insufficient chemical information about the compounds in a sample[73]. For this reason, experiments using amperometry often use other detection techniques, such as voltammetry or separation methods, to predetermine and confirm analytes of interest. Zhao et al. (2010) used continuous amperometry with the boron-doped diamond (BDD) electrode to measure 5-HT release in guinea pig mucosa tissue to better understand common gastrointestinal disorders[76]. To confirm that the measured analyte was in fact 5-HT, differential pulse voltammetry (DPV) for *in vitro* measurements of 5-HT and citalopram, a selective serotonin reuptake inhibitor, was employed at the BDD electrode[76]. Numerous other works have adapted amperometry with the carbon fiber microelectrode (CFME) to study exocytotic events involving catecholamines[77], 5-HT[78] and peptides[79] in a variety of cells[80]. These studies demonstrate another powerful feature of amperometry and ECD techniques – measurement of different analytes with suitable working electrodes based on experimental requirements.

#### 1.3.2.2 VOLTAMMETRY AND CYCLIC VOLTAMMETRY (CV)

Voltammetric methods apply time-dependent voltage to a working electrode and measure the resulting current, generated by an electroactive analyte, as a function of the applied potential[81,82]. The measurements are represented as voltammograms which are current (*I*) vs voltage (V) plots, and can be distinct for different analytes[82]. The type of voltammetric method is driven by its voltage profile since the applied potential can be manipulated to take various shapes[83]. For example, square wave voltammetry and DPV are based on stepping or pulsing to different potentials, and linear sweep voltammetry involves a single straight sweep of potential from initial to final value[84]. Whereas, cyclic voltammetry (CV) is driven by ramping the voltage up and down in a linear fashion[82]. Along with superb temporal resolution, some voltammetric techniques can also provide good selectivity and are preferred over amperometry for bioanalysis[82].

In CV, an electrode is submerged in an unstirred solution (electrolyte) and supplied with voltage in a cyclic manner using a potentiostat. The working electrode potential is controlled against a reference electrode, often in the form of a silver/silver chloride (Ag/AgCl) wire[85]. The voltage is ramped to a switching potential and back in a linear fashion, creating a triangular waveform, to analyze redox currents at those potentials[83]. More specifically, the voltage is swept from an initial potential ($E_1$) to a switching potential ($E_2$) completing the "forward scan", and then reversed to sweep back from $E_2$ to $E_1$ as a "backward or reverse scan" – this concludes one cycle in the experiment[85,86]. Fundamentally, it is important to note that the triangular waveform applied in CV can be visualized as a potential vs time (s) plot, whereas the current measured at the working electrode during this time is represented as a voltammogram (*I* vs V). In a voltammogram, when the potential is scanned positively (low $E_1$ value to high $E_2$ value), oxidation of the analyte occurs, and the resulting current is anodic[84]. Conversely, when the potential is scanned negatively (high $E_1$ value to low $E_2$ value), the analyte is reduced, and the observed current is cathodic[84]. The speed or rate at which the potential varies linearly over time defines the scan rate (V/s) of the experiment[86]. The typical rate for CV is ~ 100 mV/s, and too slow to capture neurotransmitter release in biological matrices[83]. However, CV is still a powerful and versatile technique to study the redox reactions of molecular species[86]. Although conventional CV cannot be employed for *in vivo* neurotransmitter measurements at the relevant timescale, *in vitro* experiments have proved useful in studying the oxidation-reduction processes of compounds. CV experiments can provide key insights into the behavior of molecules at a given electrode including the redox properties, reaction mechanisms, adsorption and surface interactions, diffusion coefficients, and mass transport processes. Major neurotransmitters, including DA, 5-HT, NE, and their metabolites, are

electrochemically active and have been studied extensively *in vitro* with CV at various electrodes[73,83].

#### 1.3.2.3 FAST-SCAN CYCLIC VOLTAMMETRY (FSCV)

Motivated by studying the electrochemistry of biogenic amines in 1973, Ralph N. Adams and his group carried out the novel experiment of implanting a carbon-paste electrode in the caudate nucleus of an anesthetized rat and detecting a responding signal using voltammetry[73,87]. This work pioneered *in vivo* electrochemical detection of neurotransmitters in the brain using voltammetric techniques[73]. Following advancements in the field led to the development of FSCV as a powerful tool to study instantaneous neurochemical changes and responses in the brain. FSCV has become a popular electrochemical method to detect real-time neurotransmitter release and changes in the CNS, especially in the research setting, offering superior temporal resolution and large area sampling[73]. FSCV is fundamentally similar to CV (described above); however, one major difference sets the techniques apart – the scan rate in FSCV is usually 400 V/s, much faster (1000x) than conventional CV[83]. Due to the high scan rate, FSCV is able to monitor subsecond changes in the biological environment and capture neurotransmitter release in living samples[73]. This section will look at exemplary neurotransmitters, DA and 5-HT, at the carbon fiber microelectrode (CFME) explain the FSCV voltammogram and basics further.

*FSCV is a background subtracted technique* – Due to the high scan rate of FSCV, a single scan or cycle can be completed in just a few milliseconds; however, a major complication of this is a large capacitive, background charging current[83]. When voltage is applied to the electrode, a background current is generated by the rearrangement of ions around the electrode, or charging of the electric double layer[73]. This charging current magnitude is proportional to scan rate[73,83]. Simultaneously, a faradaic current is produced by the oxidation or reduction of an electroactive analyte at the

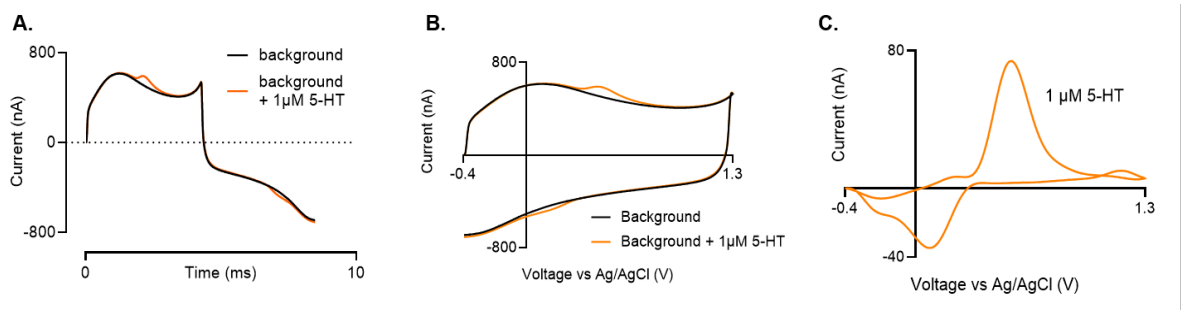


**Figure 1.4.** FSCV is a background subtracted technique. FSCV background currents with and without 1 μM 5-HT plotted with respect to **A.** time, and **B.** voltage. **C.** FSCV background-subtracted faradaic current of 1 μM 5-HT at the CFME.

electrode[83,88]. Slow scan rates produce a small background charging current that does not interfere with the faradaic current; however, FSCV background currents are much larger (10 – 100 times bigger than the faradaic current at a CFME) due to the high scan rate[83]. The background signal can overlap with the faradaic current, complicating identification of one from the other[83] (**Figure 1.4 A & B**). However, FSCV background currents are relatively stable and similar in each scan, and the background current can be subtracted out from each scan to obtain the differential signal representing the faradaic current (**Figure 1.4C**)[83]. Due to this, measurements with FSCV are differential in nature and capture rapid changes (not basal amounts) of neurotransmitters[83,89].

*Electrodes for FSCV measurements* – The background charging current is also proportional to the surface area of the electrode[83]. Thus, FSCV can only be used with small surface area electrodes, usually microelectrodes[83]. With large, macroscale electrodes (e.g., glassy-carbon electrode) the background current requires very long durations to stabilize, whereas the CFME is temporally and spatially ideal[83]. CFMEs are the standard electrodes for neurochemical sensing with FSCV[90].

*FSCV voltammogram: peak separation, symmetry, height* – Compared to traditional CV, the background subtracted FSCV voltammogram looks particularly different. These differences lie in: (1) peak separation; (2) peak symmetry, and; (3) peak heights. Firstly, in the FSCV voltammogram, the oxidation and reduction peaks are spread apart by approximately 750 mV[83]

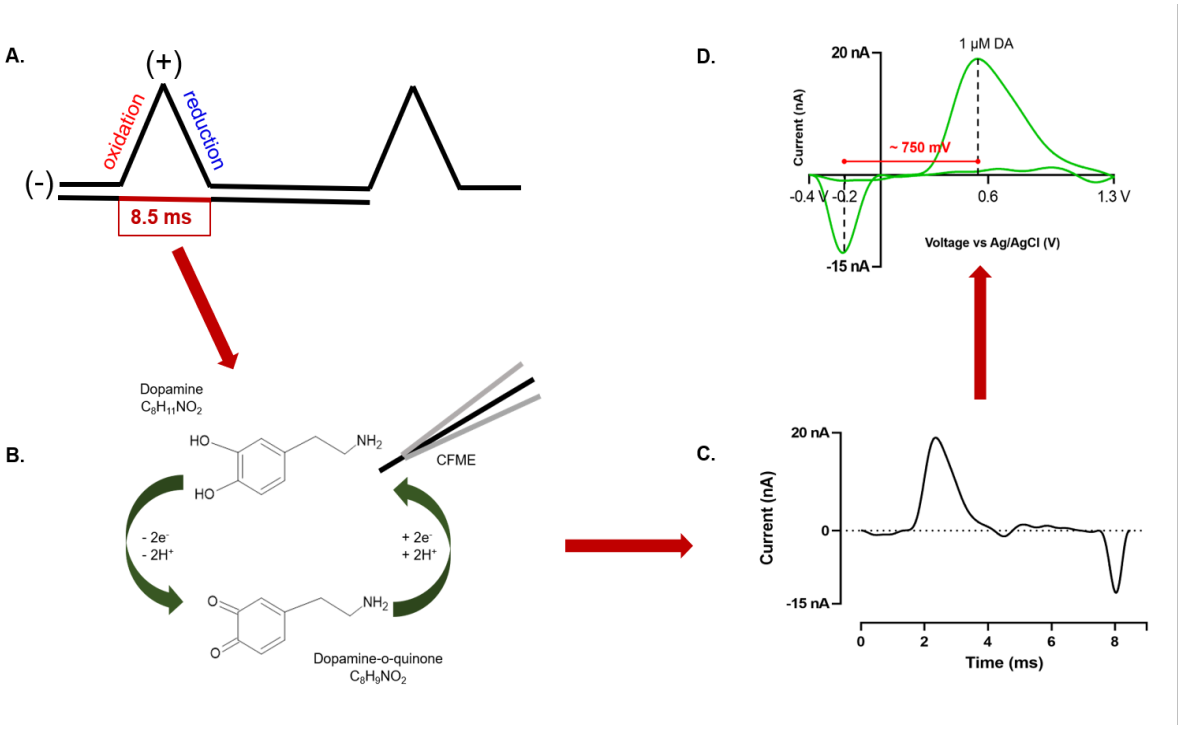


**Figure 1.5.** Generation of the cyclic voltammogram (CV) represented by FSCV. **A.** Triangular waveform applied at the electrode. **B.** Redox reaction of analyte: DA oxidizes to DOQ, and reduces back to DA. **C.** Unfolded CV along time axis to illustrate DA oxidation and reduction within 8.5 ms. **D.** Folded, typical current (I) vs voltage (V) CV generated by FSCV. Characteristics of the CV can be studied (e.g. peak separation, peak heights etc.) to investigate analyte responses. DA redox reaction illustration made with ChemSketch[167].

(**Figure 1.5D**). Peak oxidation of DA occurs at ~ 0.6 V, and peak reduction is at ~ -0.2 V. This peak separation is much wider in FSCV (compared to slower scan rate techniques) mainly because of the high scan rate, sluggish electron transfer of DA at the electrode surface, and high current density[83,91]. Secondly, the FSCV DA peaks are quite symmetrical as the current returns to zero before the backward scan begins[83]. FSCV kinetics are essentially adsorption-controlled at CFMEs, restricting DA to the surface area of the electrode in a manner that all the analyte is oxidized before being replenished by mass transport, and the current returns to zero as the potential is reversed, resulting in symmetrical peak shapes[83]. Thirdly, the symmetrical peaks are not the same height – the oxidation peak is much larger than the reduction peak[83]. At the CFME surface, DA is first oxidized to dopamine-*o*-quinone (DOQ) during the forward scan, and then, DOQ is reduced back

to DA with the backward scan[83] . While the same DA molecules can be oxidized and reduced over and over again, the peak heights differ as the amount of DOQ being reduced is not the same as the amount of DA being oxidized[81,83]. This is due to differences of DA and DOQ adsorption on the electrode surface: some DOQ possibly desorbs and falls off the surface before being reduced back to DA, thereby resulting in a smaller reduction peak[83,92].

*FSCV waveform* – A major factor influencing the FSCV waveform is adsorption of the analyte on the electrode surface[83]. The well-established DA triangular waveform (**Figure 1.5A**) generally begins at -0.4 V goes to 1.3 V and back to -0.4 V, with a scan rate of 400 V/s repeated at 10 Hz frequency (applied potential is versus Ag/AgCl reference electrode)[83,89]. Wightman's group pioneered FSCV waveform development, and demonstrated some of above-mentioned parameters as ideal for DA detection at CFMEs[92,93]. The LOD for DA at the CFME is as low as 15 nM with the typical DA waveform using FSCV[83].

The triangular waveform holds the electrode at a negative potential of -0.4 V initially to selectively target and adsorb DA on the electrode surface[89]. With increasing holding potential, the measured FSCV current for DA decreases[83]. Since DA is inherently positively charged, the electrode must be at a negative potential initially to facilitate surface adsorption. At very negative potentials (~0.6 V), oxygen can be reduced and may interfere with analyte measurement[94,95]; thus, -0.4 V is the optimized holding potential for DA adsorption[83]. The voltage is ramped up to a switching potential of +1.3 V and back to -0.4 V at 400 V/s to oxidize DA to DOQ and reduce back to DA within 8.5 ms (**Figure 1.5 B, C and D**). Increasing the current over + 1.0 V increases the DA current as the carbon fiber surface is activated to add more edge plane sites and break carbon bonds[83,93,96]. At very high potentials (> +1.3 V) the CFME surface can undergo prominent etching[96], while +1.3 V is sufficient to completely oxidize DA and preserve the electrode surface

over time. Repetition of the triangular waveform at 10 Hz is carried out to facilitate a temporal resolution of 100 ms in which neurotransmission can be detected[89]. It was found that the DA current decreased with increasing frequency[92]; hence, 10 Hz was demonstrated as the ideal rate to repeat FSCV measurements on the biological time scale. Since oxidation of DA is adsorption controlled, higher scan rates also increase DA current[83,92]. However, very high scan rates can make electrodes unstable, and therefore, 400 V/s ensures stable currents and minimizes peak distortion[83].

The FSCV waveform can be modified to detect distinct compounds depending on the electrochemical properties of the analyte[73,97] and the working electrode[73,98]. For example, adenosine oxidation requires modified anodic limits of the potential scan to facilitate electron transfer[73]. Waveform optimization can improve detection of analytes and diminish electrode fouling[89,99]. Despite modifications, interferent analytes (e.g. ascorbic acid) in the same potential window can still complicate selectivity of detecting neurotransmitters with FSCV[83,100]. Data analysis techniques (e.g., principal component regression (PCR) and machine learning) and modified electrodes have been employed to tackle issues with analyte identification[73,89].

*FSCV color plot and current vs time plot* – **Figure 1.6** illustrates an FSCV color plot and the corresponding current (I) over time (T) representation of a 1μM DA flow injection followed by Tris aCSF buffer rinsing in an in vitro flow cell set up. One second can contain 10 CVs, and a single run of few seconds will collect hundreds of CVs continuously[89]. Since it would be impractically time consuming to individually analyze every CV, developed FSCV software[101] stack all the collected CV data from one experimental run in the form of a color plot[83,89] (**Figure 1.5B**). On a 2-dimensional scale, the color plot is represented as a voltage (V) vs time (s) plot[89].

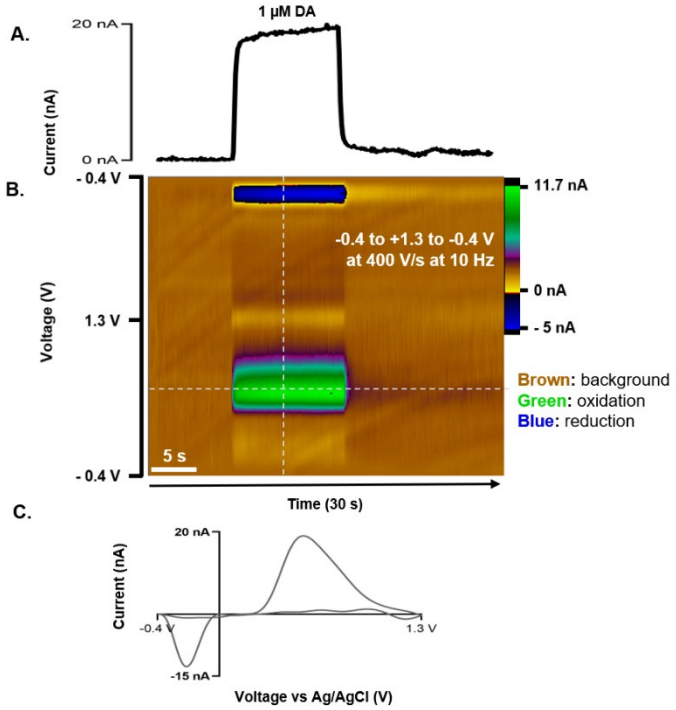


**Figure 1.6.** FSCV color plot and I vs T trace. **A**. Current (I) vs time (T) trace of 30 sec produced by a horizontal section (dotted line) of the color plot. **B.** FSCV software generated color plot (voltage vs T) of stacked CVs. Green block represents oxidation, blue shows reduction. **C**. Resulting background-subtracted CV of DA redox reaction extracted by vertical section (dotted line ~) of the color plot at the given point. A triangular waveform of -0.4 V to +1.3 V to -0.4 V at 400 V/s at 10 Hz was applied. Dopamine (DA, 1 µM) was injected at ~ 8 s, Tris aCSF was used as a buffer solution at a flow rate of 750 µL/min. Scale bar on bottom left of color plot is 5 s.

The pseudo colors showcase different currents occurring during the length of the run – blue for reduction, green for oxidation and brown as background or baseline current. A horizontal section extracted from the color plot at a given potential presents the I vs T trace of the run, while the vertical section extracts the CV[83].

## 1.4 COMMON TYPES OF IMPLANTABLE ELECTRODES IN THE BRAIN

The emergence of the first implantable electrodes for signal detection in the 1950s ushered in a new era for implantable neurotechnology. Traditionally, silicon and metal-based, and lately,

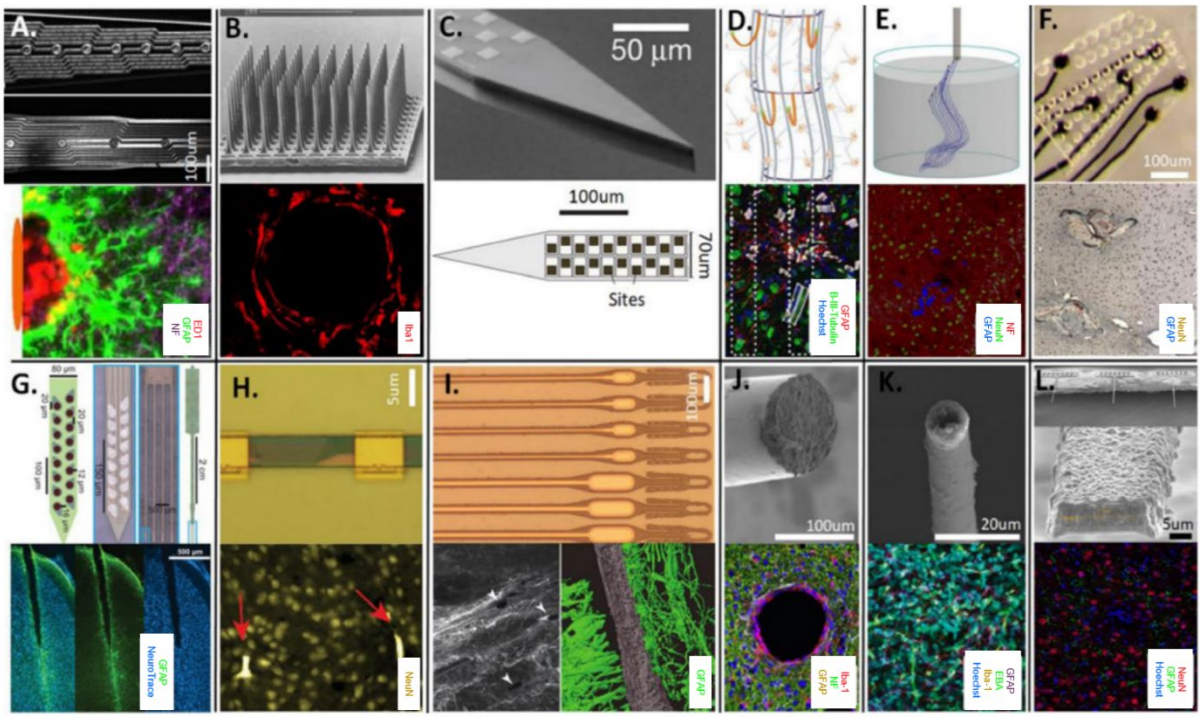


**Figure 1.7.** Different types of implantable devices and histological metrics commonly used in the field. Top and bottom panels are organized to contain device image with the corresponding histological image placed directly below. **A-C**. traditional, high density silicon and metal-based arrays. **D-E**. mesh arrays. **F-I.** polymer-based electrodes. **J-L.** carbon-based electrodes. Various neuronal (NF: neurofilament, NeuN: neuronal nuclei, NeuroTrace: neurons, B-Tubulin-III: neuronal microtubules) and glial markers (GFAP: glial fibrillary protein, Iba-1: microglia, ED-1: microglia) are pre-selected to assess densities around the injury/implant, but selection of these histological markers is not standardized across research groups and studies. Other histological markers such as Hoechst (universal DNA stain) and endothelial barrier antigen (EBA: blood brain barrier) can provide added information about the device-tissue interface. Reproduced from open-access article by Thompson et al.[50] Copyright 2020.

polymer-based, electrodes are common choices for electrical signal recording. Whereas, carbon-based electrodes have been popular selections for chemical sensing. Assessments of implantable devices of different designs, architectures, dimensions and materials have been carried out in the field (**Figure 1.7**). This section will briefly discuss conventional and next-generation implantable electrodes in the context of primary neural signal detection (i.e. electrical or chemical).

### 1.4.1 ELECTRODES WIDELY USED FOR ELECTRICAL SIGNALS

*Microwires and microwire bundles* – Some of the first electrical recordings in the brain were carried out using the glass micropipette containing a salt solution and a platinum or silver wire, paving the way for metal-based electrodes soon afterwards. Microwires employing a variety of conductive metals and alloys, such as iridium, stainless steel, platinum-iridium, and tungsten, were developed to detect unit activity, usually in cortices of smaller animals (cats, rats, squirrels, etc.). These proved useful for extracellular recording of electrical signals as the conductive metals were insulated with an exposed tip for detection in the contact tissue. As more knowledge on unit activity in the brain became available, microwire bundles were developed to sample from a larger area and include MUA signals[102]. These employed similar metals and alloys as regular microwires, but contained different designs and configurations, for example, stereotrodes (two closely-spaced microwires, often twisted together) and tetrodes (four microwires bundled together)[102].

*Microelectrode arrays (MEAs)* – Silicon-based shank arrays ('Michigan'-style arrays) were the first to employ micromachining techniques for fabrication of a multisite platform. These planar devices with a tapered shape usually contain a silicon substrate with multiple metal recording sites. Generally, recording sites nested along the shank of the probe are defined by metal deposition (platinum or iridium) onto conductive traces (polysilicon insulated with silicon dioxide and silicon nitride)[50]. Such micromachining fabrication techniques are advantageous as the devices are customizable to user specific needs, offering the possibility of different configurations (e.g. multi-shank, unique site design, multi-modal, etc.). These electrodes offer a small footprint and high yield of recorded cells for signal detection with superior biocompatibility[102]. Similarly, the Utah array, used in larger animals and humans, also utilizes a doped silicon substrate, etched into a 10 x 10 array, or 100 microneedles, with $SiO_2$ insulation between channels. The comb-like needles

have an insulation of Parylene-C along most of the length, with the tip coated with metals such as platinum or iridium[50,102]. The Utah array configuration has a flat base for needles with a flexible wire bundle enabling to needles to be positioned into the brain at a right angle. This allows the array to "float" with the natural movements of the brain relative to the skull, an important feature required for implants in larger primate and humans[30]. The Utah array is the most widely used MEA in human brains for signal detection, and sometimes, also for electrical signal delivery. A notable recent high-density, silicon-based array with 364 recording channels is the Neuropixels probe[103,104]. While this device presents an unprecedented number of recording sites of titanium nitride (TiN) along the length of the array resembling the physical design of the Michigan probe, it also experiences hardware and software constraints that limit simultaneous recording from all sites.

*Polymer-based and next-generation electrode arrays* – Flexible substrates offering reduced footprint and smaller dimensions have gained recent attention as modern implantable neurotechnology advances towards better integrating the device and host tissue. Ellis Meng's group reported on a flexible Parylene-based planar array with precisely organized platinum traces and recording sites to detect signals in the rat hippocampus[105,106]. Investigations on this device showed that bending stiffness, i.e. the measured material resistance towards deformation upon implantation, along the tapered shank was minimal. The Parylene sheath electrode, also developed by the Meng group, allows tissue to occupy the device structure for cellular signaling through the device[107]. Coatings of bioactive compounds can further increase biocompatibility and long term (~ 50 weeks) recordings using this device. Other developments with Parylene-C have supported similar results of notable integration in the tissue and overall biocompatibility[50,108,109]. Purcell and Seymour reported on a planar, hollowed out, Parylene-coated device containing a scaffold seeded

with neural stem cells. These showed promising transient effects of greater neuronal densities and reduced acute immune response around the implanted device in rat cortices, but not beyond the 6-week timepoint at which glial encapsulation and cell density appeared similar to control conditions. Polyimide-based devices also offer a reduced footprint and potentially improved integration including the use of bioactive surface modification. The flexible polyimide probe has shown viable signal recording over 5 months, and reduced astrocyte device encapsulation at 160 days after implantation. The nanoelectronic thread (NET), or Neuralthread device, developed by Chong Xie's group, is an ultra-flexible probe micromachined to be scalable to smaller dimensions and include biocompatible materials[110]. These flexible devices are inserted using a carbon fiber shuttle device that attaches to the micro-hole at the apex of the NET similar to how a sewing needle interacts with a thread, and then disengages once the device is implanted at the desired depth. Post-implant chronic histology showed improved recovery of neuronal density, and better overall integration with minimal cellular morphology disruption around the device.

### 1.4.2 ELECTRODES WIDELY USED FOR CHEMICAL SIGNALS

*Carbon electrodes* – Carbon electrodes are routinely employed for electrochemical detection methods as these materials commonly offer notable properties of high mechanical strength, good electrical and thermal conductivity, chemical inertness, and rich surface chemistry[111]. Carbon can form microstructurally distinct allotropes, including glassy carbon, single and polycrystalline diamond, diamond-like carbon ($sp^2$ and $sp^3$ carbon bonding mixtures) and graphitic carbons (e.g. single sheet graphene, nanotubes, etc.)[111]. A standard carbon electrode used for sensing in biological samples is the CFME. This is a benchmark electrode to use with FSCV, offering the excellent properties of carbon electrodes as well as increased surface area and flexibility as a microelectrode. The CFME contains $sp^2$-bonded carbon structure along with an extended π-

electron system[90]. The surface oxide functional groups adsorb cations, making these devices excellent tools for detecting positively charged neurotransmitters[83]. CFMEs offer small-diameters that cause minimal tissue damage, and low-cost hand fabrication methods that are easily accessible[100]. The kinetics at these electrodes are adsorption controlled[83,92], which is especially advantageous for techniques like FSCV. Coatings and surface modifications to the CFME are commonly employed techniques to enhance chemical sensing at the electrode. Recently, different types of carbon-fiber based microelectrodes have been developed in an attempt to reduce cellular response to the electrode, minimize fouling, and device-design challenges for chronic recordings [112–114]. These include the micro-invasive probe (μIP), flexible glassy carbon multielectrode array, carbon fiber thread array, and carbon nanotube electrodes (CNT)[114].

Carbon materials are also a popular choice as nanocoatings due to high conductivity, biocompatibility, and versatility for not only electrochemical sensors, but also electrophysiological sensors [115–120], despite trade-offs in signal instability, etching and fouling (explained further in Section 1.7) of the carbon material itself. Coatings, such as electrodeposited PtIr and poly (3,4-ethylenedioxythiophene) polystyrene sulfonate (PEDOT-PSS), can enhance the charge carrying capacity at the electrode surface[121]. CNTs have similarly been deposited as coatings due to exceptional electrical performance and biocompatibility[115] while graphene and nanodiamond have proved useful as biocompatible materials[122–128].

*Diamond-based and next-generation electrodes* – Although an allotrope of carbon, diamond and diamond-like carbon materials have been recognized widely for the prospect of biosensing, and development of next-generation devices[129–132]. The boron-doped diamond (BDD) electrode, often produced by chemical vapor deposition (CVD), is one such candidate with extensively studied electrochemical properties and promising biocompatibility appropriate for neurochemical

sensing[98,133]. Diamond itself is a form of carbon that has a rigid non-polar, bonding structure of $sp^3$ hybridization[90]. Upon the level of boron-doping, diamond can become sufficiently conductive for use as an electrode[90,134]. The surface characterization of stable $sp^3$ bonded carbon, without an extended π-electron system, enable BDD electrodes to be excellent electrochemical sensors that have[90]: 1) wide working potentials; 2) lower background currents; 3) good mechanical and chemical stability, and; 4) good electrochemical activity without pre-treatment[98,134]. The surface characterization is inherently more resistant to corrosion, and the wide potential window allows greater stability with applied voltages of over 1.0 V needed for the detection of biomolecules[90]. Chemical and mechanical stability of the electrode resists high adsorption at the surface and reduces fouling[90]. Lower background currents provide better signal to background and signal to noise ratio which could be advantageous for long-term implantation and signal stability[90,133]. BDD nano/microelectrodes have already been applied for *in vitro* biosensing of NE, 5-HT, adenosine, histamine and nitric oxide[90]. Polycrystalline BDD on tungsten rods have demonstrated reduced fouling and increased robustness compared to CFMEs with long-term FSCV measurements[89,135]. Clinically, these electrodes have been implemented to address the issue of CFME degradation during chronic sensing, and were successfully applied in humans to detect adenosine during DBS treatment[135]. Due to the surface characterization of diamond, a tradeoff of decreased sensitivity *in vivo* may have to be accepted with BDD microelectrodes; however, stability of the device (as working or reference electrodes) offers potential for chronic sensing of biomolecules[98].

## 1.5 SIGNAL INSTABILITY: A MAJOR CHALLENGE OF IMPLANTABLE ELECTRODES

Although there is notable success in recording neural activity over time, signal variability in chronic recordings is a well-established challenge with implanted devices[136–140]. Signal

inconsistencies have been observed in electrical and chemical recordings in the brain, more prominently in the long term. Device failure, signal loss and instability can complicate decoding activity and compromise the performance of closed-loop systems. Decoding algorithms and closed-loop neurostimulation often rely on neuronal spike detection[66]. Action potentials generated by neurons are detected as spikes in voltage in the ~500 to 5000 Hz frequency band of signals detected at electrodes implanted in neural tissue. However, numerous studies across animal models have observed a reduction in spike amplitudes as well as complete signal loss over time[66,141–145]. A seminal study by Biran et al. observed a ~40% decrease in neuronal population density around silicon Michigan-style probes implanted for 4 weeks in rat cortex[146]. Chestek et al. reported an average 2.4% decrease per month in action potential peak amplitude over 9.4, 10.4 and 31.7 months in 3 non-human primates implanted with silicon cortical arrays[147]. In one animal, amplitude declined by 37% within the first 2 months of implantation. This rapid decay in signal quality and stability has also been observed in days and weeks post insertion in rodent models[136,148,149]. More recently, Chestek and colleagues investigated Utah arrays implanted in non-human primates for up to 2 years, and found similar ~60% losses in signals[150]. These observations provide evidence of a change in the biological environment surrounding implanted electrodes with suboptimal recovery post-implantation to produce viable electrical signals in the long-term.

Similar patterns of signal loss have been identified in limited reports with neurochemical sensors using FSCV, commonly at the CFME[83,89,97,100,137,151]. As a background subtracted technique, FSCV relies on a stable background current to provide high temporal resolution (i.e. 10 Hz) that can capture neurotransmission. Consequently, signal instability can majorly compromise accuracy of measured peak currents. The sensitivity of CFMEs to dopamine decreases by ~50% after implantation in the rat brain as revealed by pre and post calibrations of electrodes in a study

using FSCV conducted by the Wightman group[83,152]. Other FSCV works have investigated in vitro brain tissue exposure and reported similar observations of ~60-70% sensitivity decrease at CFMEs[100]. Chronic in vivo works have reported on drifts in the background currents and gradual peak signal decay within days after device implantation in rat brains[137]. Overall, these findings corroborate that the biological environment, or reactive tissue response, is a key underlying contributor to signal instability and loss in implanted electrodes.

## 1.6 THE BIOLOGICAL RESPONSE TO IMPLANTED ELECTRODES

The inherent biological response to implanted electrodes is multifaceted, involving physiological, chemical and mechanical factors (**Figure 1.8**). A cascade of reactive tissue responses is initiated immediately upon device insertion, which causes blood-brain barrier breach and vasculature disruption. Rapid and nonspecific chemical adsorption of proteins (such as albumin and fibrinogen) to the electrode surface occurs within minutes after implantation[153]. Adsorption of proteins builds a layer at the electrode surface, enabling cells gathering at the site to interact with the foreign body[153]. Inflammatory microglia are activated and extend processes towards the implant within minutes after device insertion[154]. Early responders, such as neutrophils and macrophages, respond to the implant with degrading enzymes and reactive oxygen species in subsequent days[153]. In the following weeks, microglia and reactive astroglia significantly increase to encase and surround the device, forming a glial scar[155]. Neuronal loss at the implant can occur[146,156], and functional changes in near-device neurons can be observed[66]. The chronic foreign body response is guided by cellular encapsulation that isolates the electrode from the host tissue and impedes overall device performance. Additionally, insertional trauma and signal stability can also be affected by mechanical features. A plethora of evidence indicates that electrode design and architecture, including device cross-sectional dimensions, Young's modulus and bending-

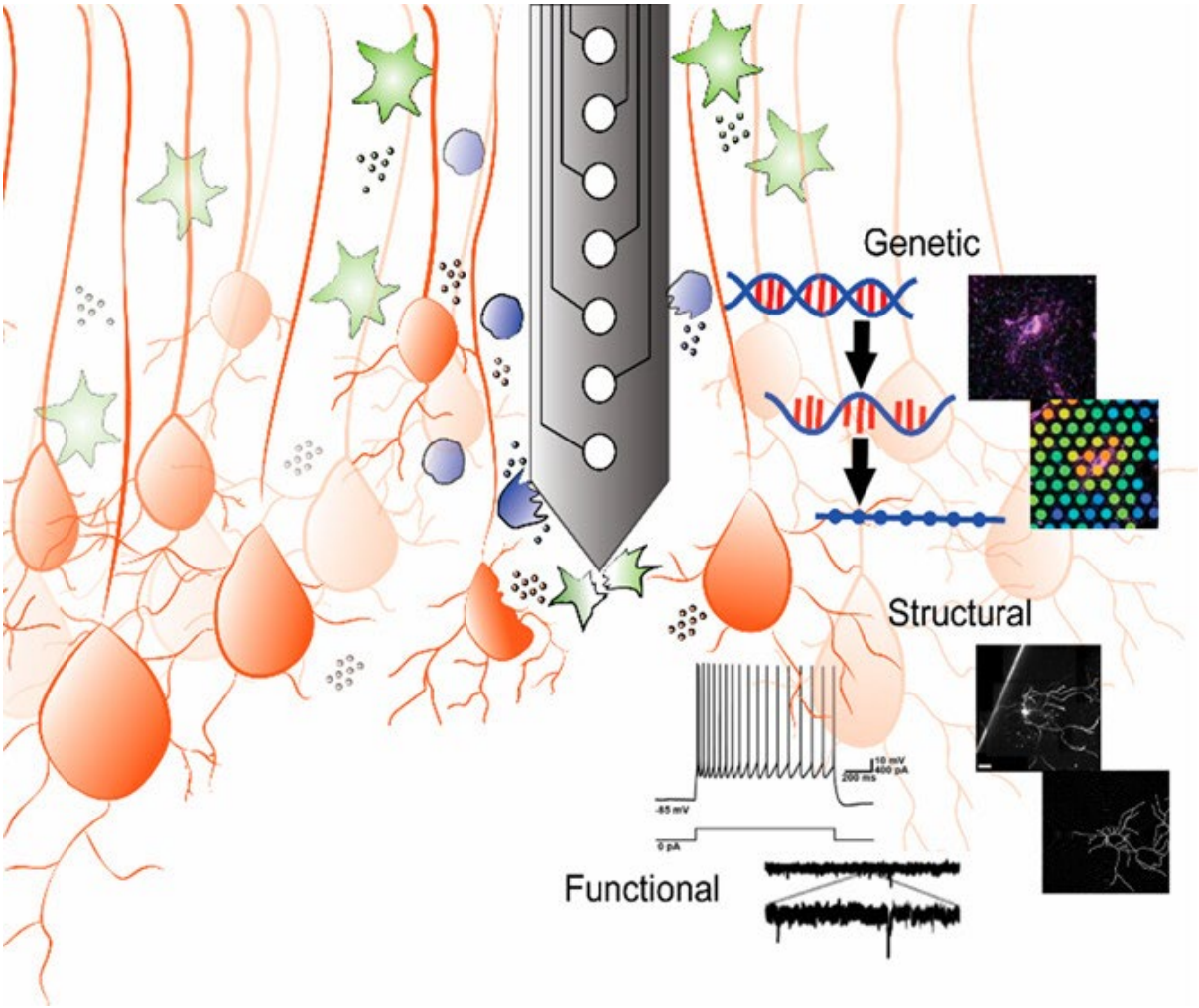


**Figure 1.8.** The biological response to implanted electrodes is multifaceted, warranting an investigation using a variety of techniques and technology. The overall tissue response is guided by physiological, chemical and mechanical factors that give rise to structural, functional and genetic changes in the biological environment of implanted electrodes. Reused from Gupta et al.[168] Copyright 2024.

stiffness, are vital features that guide device-tissue integration in the brain[50]. Tethering forces, or mechanical strain, created by connector configuration can also contribute to the tissue response[157]. In general, smaller (<10 um) and softer probes have been suggested to favor improved tissue integration. Various device types, including traditional silicon- and metal-based arrays, mesh arrays, polymer and carbon-based electrodes, have been implemented in the field to assess biocompatibility and signal quality[50].

From a chemical sensing standpoint, electrode material and device type majorly influence signal detection in the biological environment. Changes to the electrode surface can alter the background current signal when employing FSCV detection techniques for neurotransmitter sensing. During in vivo FSCV at the CFME, the electrode is introduced in a conductive aqueous environment (interstitial fluid) with an applied potential of greater than 1.0 V (vs Ag/AgCl). The surface of the electrode undergoes chemical and physical changes[158] as oxygen-containing (carbonyl and hydroxyl) functional groups are added to the carbon-fiber surface that consequently increase the CV faradaic current[158,159]. The addition of these groups increases the background current and shifts its peak until equilibrium, or relative stabilization[158]. Neurochemical recordings are typically taken after the electrode is stabilized as the carbon-fiber surface is sufficiently activated[158]. Immediate post-implantation "cycling", i.e. applying the waveform at a given frequency, can stabilize the background current and ensure minimal drift contamination. Acutely implanted CFMEs often require ~ 30 mins at 60 Hz followed by at least 10 mins at 10 Hz for cycling, whereas chronic CFMEs can take up to ~ 2 hours to stabilize initially[158]. Regardless of thorough cycling periods, the recorded signal still experiences some drift[158], and time taken to reach equilibrium can vary across CFMEs[158] as each electrode is fabricated individually. Moreover, the carbon fiber surface is prone to etching with each voltage scan especially over +1.0 V (vs Ag/AgCl), and this adds to the overall stabilization drift[158]. Etching effects both the faradaic and non-faradaic current, and depends on the duration of applied high potential at the electrode[158]. Generally, the drift generated by surface etching is at a lower rate than that by surface chemistry[158]. The rate of etching drift is not different between acute and chronic electrodes; however, the total etching across a working chronic electrode will be greater as the recording intervals are longer[158].

Whereas etching and background stabilization drifts currently exist as unavoidable

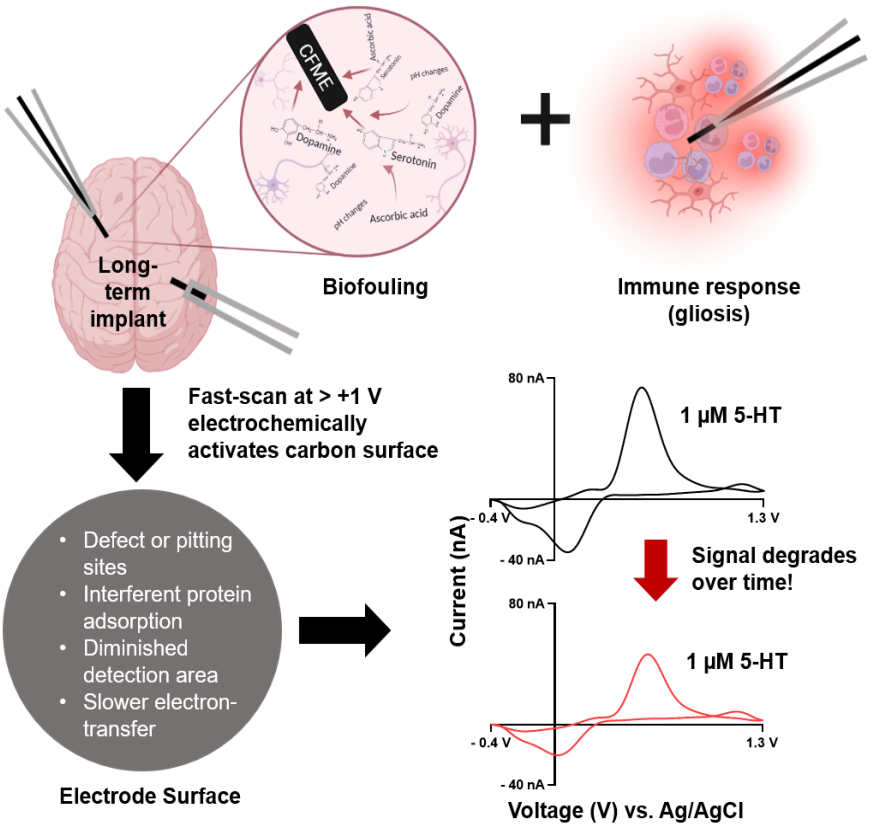


**Figure 1.9.** Biological challenges to chronic neurochemical sensing with implantable microelectrodes. Long-term sensors experience biofouling, occurring from the adsorption of unwanted proteins and interferent molecules at the electrode surface, as well as cellular encapsulation (gliosis) taking place over days and weeks following implantation. Image created with *BioRender* (www.BioRender.com).

phenomena with biochemical sensors employing a voltage driven technique like FSCV, the biological tissue response can compound the effects of detected signal variations (**Figure 1.9**). Chronic FSCV studies have reported on the occurrence of biofouling, i.e. the nonspecific adsorption of interferent molecules at the electrode surface upon implantation. This arises from the obvious presence of electroactive analytes other than the target chemical (specific neurotransmitter DA or 5-HT) in a biological presence. Highly adsorptive electrode surfaces, such as that of CFME with $sp^2$ hybridized bonding structure, are prone to biofouling. Although electrochemical activation at the CFME with high potentials produces surface defect sites that promote adsorption and sensitivity to analytes[83,158] , significant corrosion of more than one

chemical at the electrode is also facilitated[90]. Adsorbed unwanted proteins, due to biofouling of the surface, act as a barrier by diminishing the available electrode surface area for adsorption and electron transfer of compounds of interest[83]. Biofouling can change CVs of known analytes – DA peaks are shifted apart (as slower electron transfer takes place), and ratio of peak current oxidation to peak current reduction changes (as adsorption is restricted)[83]. The overall peak amplitude and sensitivity of the electrode from pre-calibration to post-calibration is further significantly reduced (~ 50% loss)[83,152]. While the chronic tissue response of cellular encapsulation (gliosis and neuronal damage) to implanted electrodes occurs over a prolonged period of days to weeks, biofouling is a more acute and immediate process that can affect electrode performance over the duration of the study. Together, the biological tissue response can contaminate the electrode surface area, limit transfer kinetics, reduce electrode sensitivity and selectivity, shift faradaic peaks and lead to signal instability[89,137].

Evidence of the biological response to implanted electrodes employing neurotransmitter detection using FSCV are limited, while electrophysiological reports are abundant. Nevertheless, the metrics for assessing tissue response are not well-defined. Histological assessments of neuronal density and glial fibrillary acidic protein (GFAP) have traditionally been used to study the biological response and tissue health after device implantation[160]. However, histology alone is not a valid predictor of signal quality or recording performance. Michelson et al. demonstrated that the biological response at the electrode interface is complex, and long-established histological metrics, including NeuN, Iba1, GFAP, and IgG, offer limited information on neuronal health and recording performance[160]. Further, conventional staining and qPCR assessments provide relatively limited assessment of device-tissue biocompatibility due to low-throughput (the assays require pre-selecting a few markers of interest). Newer techniques of spatial transcriptomics can map

transcriptional changes with improved spatial resolution and allow for flexible selection of comparison regions alongside traditional immunofluorescence labeling[161], which has been used to reveal new information about both recording and stimulating electrodes[162,163].

Recent work from our group has focused on the biological effects of electrode implantation in the brain and uncovered unexpected effects of the device presence on the structure, function, and gene expression of neighboring brain cells[66,164]. Using whole cell electrophysiology and 2-photon imaging, Gregory et al. observed that implanted recording electrodes are accompanied by reduced excitatory postsynaptic currents, altered dendritic structure, a reduction of spine density, and changes in the spine morphologies and intrinsic excitability of neurons within the recordable radius of implanted electrodes[66]. In parallel, transcriptomics data by Thompson et al. (2021) and Whitsitt et al. (2021) revealed hundreds of differentially expressed genes around the implant site, indicative of disruptions in synaptic transmission, astrogliosis, oligodendrocyte dysfunction, and microglial activation[162,164]. Spatial transcriptomics on tissue following electrical stimulation showed induction of the genetic signatures of cell death, plasticity, and activity in a manner dependent on the intensity of the applied stimulus[163]. Lately, work from our group has implemented computational approaches [165] with the goal to identify the genes most strongly predictive of changes in recording performance.[166] As the field moves toward smaller and softer devices, and the incorporation of nanoscale topologies and nanomaterials, the identification of biomarkers of performance will enable: (a) the ability to benchmark the biocompatibility of emerging materials and design parameters in the context of functional outcomes, and (b) the identification of biological mechanisms underlying recording quality and stimulation effects, which will enable the design of targeted modifications to improve performance and therapeutic effects.

## 1.7 CONCLUDING REMARKS

To gain a better understanding of the biological tissue response and the intricacies of the device-tissue interface, a diverse approach employing a variety of techniques, device types and technology is warranted. This work investigates two sources of signal loss of electrodes in the brain (1) protein adsorption ("biofouling"), and (2) cellular encapsulation. By employing a material perspective as well as tissue level investigation with computational analysis, the findings herein add: (1) novel insights on the performance of a next-generation diamond-based device, particularly to investigate biofouling at a recently developed freestanding boron-doped diamond microelectrode (BDDME), and (2) new insights of gene expression at the device-tissue interface implanted with chronic silicon Michigan-style probes. These details add to the growing body of literature suggesting that the biological response to electrodes remains a major limitation for chronic recording quality.

## REFERENCES


(1) Deer, T. R. History of Neurostimulation. In *Atlas of Implantable Therapies for Pain Management*; Springer New York: New York, NY, 2011; pp 3–7. https://doi.org/10.1007/978-0-387-88567-4_1.

(2) Rettinger, J.; Schwarz, S.; Schwarz, W. *Electrophysiology*; Springer International Publishing: Cham, 2022. https://doi.org/10.1007/978-3-030-86482-8.

(3) Chandrasekaran, S.; Fifer, M.; Bickel, S.; Osborn, L.; Herrero, J.; Christie, B.; Xu, J.; Murphy, R. K. J.; Singh, S.; Glasser, M. F.; Collinger, J. L.; Gaunt, R.; Mehta, A. D.; Schwartz, A.; Bouton, C. E. Historical Perspectives, Challenges, and Future Directions of Implantable Brain-Computer Interfaces for Sensorimotor Applications. *Bioelectron Med* **2021**, *7* (1), 14. https://doi.org/10.1186/s42234-021-00076-6.

(4) Bertil Hille. *Ion Channels of Excitable Membranes*, Third Edition.; Sinauer Associates, 2001.

(5) Kaplan, R. M. The Mind Reader: The Forgotten Life of Hans Berger, Discoverer of the EEG. *Australasian Psychiatry* **2011**, *19* (2), 168–169. https://doi.org/10.3109/10398562.2011.561495.

(6) İnce, R.; Adanır, S. S.; Sevmez, F. The Inventor of Electroencephalography (EEG): Hans Berger (1873–1941). *Child's Nervous System* **2021**, *37* (9), 2723–2724. https://doi.org/10.1007/s00381-020-04564-z.

(7) HODGKIN, A. L.; HUXLEY, A. F. Action Potentials Recorded from Inside a Nerve Fibre. *Nature* **1939**, *144* (3651), 710–711. https://doi.org/10.1038/144710a0.

(8) Schwiening, C. J. A Brief Historical Perspective: Hodgkin and Huxley. *J Physiol* **2012**, *590* (11), 2571–2575. https://doi.org/10.1113/jphysiol.2012.230458.

(9) Hodgkin, A. L.; Huxley, A. F. A Quantitative Description of Membrane Current and Its Application to Conduction and Excitation in Nerve. *J Physiol* **1952**, *117* (4), 500–544. https://doi.org/10.1113/jphysiol.1952.sp004764.

(10) Armstrong-James, M., Millar, J. & Kruk, Z. Quantification of noradrenaline iontophoresis. *Nature* **288**, 181–183 (1980). https://doi.org/10.1038/288181a0.

(11) Baur, J. E.; Kristensen, E. W.; May, L. J.; Wiedemann, D. J.; Wightman, R. M. Fast-Scan Voltammetry of Biogenic Amines. *Anal Chem* **1988**, *60* (13), 1268–1272. https://doi.org/10.1021/AC00164A006.

(12) NEHER, E.; SAKMANN, B. Single-Channel Currents Recorded from Membrane of Denervated Frog Muscle Fibres. *Nature* **1976**, *260* (5554), 799–802. https://doi.org/10.1038/260799a0.

(13) Bretag, A. H. The Glass Micropipette Electrode: A History of Its Inventors and Users to 1950. *Journal of General Physiology* **2017**, *149* (4), 417–430. https://doi.org/10.1085/jgp.201611634.

(14) Dowben, R. M.; Rose, J. E. A Metal-Filled Microelectrode. *Science (1979)* **1953**, *118* (3053), 22–24. https://doi.org/10.1126/science.118.3053.22.

(15) Hubel, D. H. Tungsten Microelectrode for Recording from Single Units. *Science (1979)* **1957**, *125* (3247), 549–550. https://doi.org/10.1126/science.125.3247.549.

(16) Strumwasser, F. Long-Term Recording from Single Neurons in Brain of Unrestrained Mammals. *Science (1979)* **1958**, *127* (3296), 469–470. https://doi.org/10.1126/science.127.3296.469.

(17) Naka, K.-I.; Kido, R. Hypothalamic Spike Potentials Recorded by Chronically Implanted Tungsten Microelectrodes. *Brain Res* **1967**, *5* (3), 422–424. https://doi.org/10.1016/0006-8993(67)90049-2.

(18) Wise, K. D.; Angell, J. B.; Starr, A. An Integrated-Circuit Approach to Extracellular Microelectrodes. *IEEE Trans Biomed Eng* **1970**, *BME-17* (3), 238–247. https://doi.org/10.1109/TBME.1970.4502738.

(19) Salcman, M.; Bak, M. J. Design, Fabrication, and In Vivo Behavior of Chronic Recording Intracortical Microelectrodes. *IEEE Trans Biomed Eng* **1973**, *BME-20* (4), 253–260. https://doi.org/10.1109/TBME.1973.324189.

(20) Salcman, M.; Bak, M. J. A New Chronic Recording Intracortical Microelectrode. *Med Biol Eng* **1976**, *14* (1), 42–50. https://doi.org/10.1007/BF02477088.

(21) Schmidt, E. M.; Bak, M. J.; McIntosh, J. S. Long-Term Chronic Recording from Cortical Neurons. *Exp Neurol* **1976**, *52* (3), 496–506. https://doi.org/10.1016/0014-4886(76)90220-X.

(22) Drake, K. L.; Wise, K. D.; Farraye, J.; Anderson, D. J.; BeMent, S. L. Performance of Planar Multisite Microprobes in Recording Extracellular Single-Unit Intracortical Activity. *IEEE Trans Biomed Eng* **1988**, *35* (9), 719–732. https://doi.org/10.1109/10.7273.

(23) Kipke, D. R.; Vetter, R. J.; Williams, J. C.; Hetke, J. F. Silicon-Substrate Intracortical Microelectrode Arrays for Long-Term Recording of Neuronal Spike Activity in Cerebral Cortex. *IEEE Transactions on Neural Systems and Rehabilitation Engineering* **2003**, *11* (2), 151–155. https://doi.org/10.1109/TNSRE.2003.814443.

(24) Vetter, R. J.; Williams, J. C.; Hetke, J. F.; Nunamaker, E. A.; Kipke, D. R. Chronic Neural Recording Using Silicon-Substrate Microelectrode Arrays Implanted in Cerebral Cortex. *IEEE Trans Biomed Eng* **2004**, *51* (6), 896–904. https://doi.org/10.1109/TBME.2004.826680.

(25) Jones, K. E.; Campbell, P. K.; Normann, R. A. A Glass/Silicon Composite Intracortical Electrode Array. *Ann Biomed Eng* **1992**, *20* (4), 423–437. https://doi.org/10.1007/BF02368134.

(26) Campbell, P. K.; Jones, K. E.; Huber, R. J.; Horch, K. W.; Normann, R. A. A Silicon-Based, Three-Dimensional Neural Interface: Manufacturing Processes for an Intracortical Electrode Array. *IEEE Trans Biomed Eng* **1991**, *38* (8), 758–768. https://doi.org/10.1109/10.83588.

(27) Willsey, M. S.; Shah, N. P.; Avansino, D. T.; Hahn, N. V.; Jamiolkowski, R. M.; Kamdar, F. B.; Hochberg, L. R.; Willett, F. R.; Henderson, J. M. A High-Performance Brain–Computer Interface for Finger Decoding and Quadcopter Game Control in an Individual with Paralysis. *Nat Med* **2025**, *31* (1), 96–104. https://doi.org/10.1038/s41591-024-03341-8.

(28) BrainGate Trials. Publications. https://www.braingate.org/publications/ (2025).

(29) Pun, T. K.; Khoshnevis, M.; Hosman, T.; Wilson, G. H.; Kapitonava, A.; Kamdar, F.; Henderson, J. M.; Simeral, J. D.; Vargas-Irwin, C. E.; Harrison, M. T.; Hochberg, L. R. Measuring Instability in Chronic Human Intracortical Neural Recordings towards Stable, Long-Term Brain-Computer Interfaces. *Commun Biol* **2024**, *7* (1), 1363. https://doi.org/10.1038/s42003-024-06784-4.

(30) Blackrock Neurotech. *NeuroPort*. https://blackrockneurotech.com/products/neuroport/ (2025).

(31) Synchron 2023. The Technology | Synchron's BCI.

(32) NeuroNexus. *Advanced Multi-channel Electrodes, Instrumentation, and Software for Neuroscience Research*. https://www.neuronexus.com/ (2025).

(33) Paradromics. *Connexus® Brain-Computer Interface*. Connexus® Brain-Computer Interface (2025).

(34) Neuralink. *N1 Implant*. https://neuralink.com/#n1 (2025).

(35) Precision Neuroscience. *The Layer 7 Cortical Interface*. https://precisionneuro.io/product (2025).

(36) Flow Neuroscience. *Noninvasive Headset*. https://www.flowneuroscience.com/ (2025).

(37) Laxton, A. W.; Tang-Wai, D. F.; McAndrews, M. P.; Zumsteg, D.; Wennberg, R.; Keren, R.; Wherrett, J.; Naglie, G.; Hamani, C.; Smith, G. S.; Lozano, A. M. A Phase I Trial of Deep Brain Stimulation of Memory Circuits in Alzheimer's Disease. *Ann Neurol* **2010**, *68* (4), 521–534. https://doi.org/10.1002/ana.22089.

(38) Whiting, D. M.; Tomycz, N. D.; Bailes, J.; de Jonge, L.; Lecoultre, V.; Wilent, B.; Alcindor, D.; Prostko, E. R.; Cheng, B. C.; Angle, C.; Cantella, D.; Whiting, B. B.; Mizes, J. S.; Finnis, K. W.; Ravussin, E.; Oh, M. Y. Lateral Hypothalamic Area Deep Brain Stimulation for Refractory Obesity: A Pilot Study with Preliminary Data on Safety, Body Weight, and Energy Metabolism. *J Neurosurg* **2013**, *119* (1), 56–63. https://doi.org/10.3171/2013.2.JNS12903.

(39) Ranjan, M.; Ranjan, N.; Deogaonkar, M.; Rezai, A. Deep Brain Stimulation for Refractory Depression, Obsessive-Compulsive Disorder and Addiction. *Neurol India* **2020**, *68* (8), 282. https://doi.org/10.4103/0028-3886.302459.

(40) Sun, F. T.; Morrell, M. J.; Wharen, R. E. Responsive Cortical Stimulation for the Treatment of Epilepsy. *Neurotherapeutics* **2008**, *5* (1), 68–74. https://doi.org/10.1016/j.nurt.2007.10.069.

(41) Shekhawat, G. S.; Sundram, F.; Bikson, M.; Truong, D.; De Ridder, D.; Stinear, C. M.; Welch, D.; Searchfield, G. D. Intensity, Duration, and Location of High-Definition Transcranial Direct Current Stimulation for Tinnitus Relief. *Neurorehabil Neural Repair* **2016**, *30* (4), 349–359. https://doi.org/10.1177/1545968315595286.

(42) Moore, D. R.; Shannon, R. V. Beyond Cochlear Implants: Awakening the Deafened Brain. *Nat Neurosci* **2009**, *12* (6), 686–691. https://doi.org/10.1038/nn.2326.

(43) Sheth, S. A.; Mayberg, H. S. Deep Brain Stimulation for Obsessive-Compulsive Disorder and Depression. *Annu Rev Neurosci* **2023**, *46* (1), 341–358. https://doi.org/10.1146/annurev-neuro-110122-110434.

(44) Rotsides, J.; Mammis, A. The Use of Deep Brain Stimulation in Tourette's Syndrome. *Neurosurg Focus* **2013**, *35* (5), E4. https://doi.org/10.3171/2013.8.FOCUS13292.

(45) Moore, D. R.; Shannon, R. V. Beyond Cochlear Implants: Awakening the Deafened Brain. *Nat Neurosci* **2009**, *12* (6), 686–691. https://doi.org/10.1038/nn.2326.

(46) Quinn, E. J.; Blumenfeld, Z.; Velisar, A.; Koop, M. M.; Shreve, L. A.; Trager, M. H.; Hill, B. C.; Kilbane, C.; Henderson, J. M.; Brontë-Stewart, H. Beta Oscillations in Freely Moving Parkinson's Subjects Are Attenuated during Deep Brain Stimulation. *Mov Disord* **2015**, *30* (13), 1750–1758. https://doi.org/10.1002/mds.26376.

(47) Satzer, D.; Wu, S.; Henry, J.; Doll, E.; Issa, N. P. Ambulatory Local Field Potential Recordings from the Thalamus in Epilepsy: A Feasibility Study. *Stereotact Funct Neurosurg* **2023**, *101* (3), 195–206. https://doi.org/10.1159/000529961.

(48) Collinger, J. L.; Wodlinger, B.; Downey, J. E.; Wang, W.; Tyler-Kabara, E. C.; Weber, D. J.; McMorland, A. J. C.; Velliste, M.; Boninger, M. L.; Schwartz, A. B. High-Performance Neuroprosthetic Control by an Individual with Tetraplegia. *Lancet* **2013**, *381* (9866), 557–564. https://doi.org/10.1016/S0140-6736(12)61816-9.

(49) Nijhuis, H. J. A.; Hofsté, W.-J.; Krabbenbos, I. P.; Dietz, B. E.; Mugan, D.; Huygen, F. First Report on Real-World Outcomes with Evoked Compound Action Potential (ECAP)-Controlled Closed-Loop Spinal Cord Stimulation for Treatment of Chronic Pain. *Pain Ther* **2023**, *12* (5), 1221–1233. https://doi.org/10.1007/s40122-023-00540-y.

(50) Thompson, C. H.; Riggins, T. E.; Patel, P. R.; Chestek, C. A.; Li, W.; Purcell, E. Toward Guiding Principles for the Design of Biologically-Integrated Electrodes for the Central Nervous System. *J Neural Eng* **2020**, *17* (2), 021001. https://doi.org/10.1088/1741-2552/ab7030.

(51) Broccard, F. D.; Mullen, T.; Chi, Y. M.; Peterson, D.; Iversen, J. R.; Arnold, M.; Kreutz-Delgado, K.; Jung, T.-P.; Makeig, S.; Poizner, H.; Sejnowski, T.; Cauwenberghs, G. Closed-Loop Brain–Machine–Body Interfaces for Noninvasive Rehabilitation of Movement Disorders. *Ann Biomed Eng* **2014**, *42* (8), 1573–1593. https://doi.org/10.1007/s10439-014-1032-6.

(52) Rosin, B.; Slovik, M.; Mitelman, R.; Rivlin-Etzion, M.; Haber, S. N.; Israel, Z.; Vaadia, E.; Bergman, H. Closed-Loop Deep Brain Stimulation Is Superior in Ameliorating Parkinsonism. *Neuron* **2011**, *72* (2), 370–384. https://doi.org/10.1016/j.neuron.2011.08.023.

(53) Orsborn, A. L.; Carmena, J. M. Creating New Functional Circuits for Action via Brain-Machine Interfaces. *Front Comput Neurosci* **2013**, *7*. https://doi.org/10.3389/fncom.2013.00157.

(54) Lorach, H.; Galvez, A.; Spagnolo, V.; Martel, F.; Karakas, S.; Intering, N.; Vat, M.; Faivre, O.; Harte, C.; Komi, S.; Ravier, J.; Collin, T.; Coquoz, L.; Sakr, I.; Baaklini, E.; Hernandez-Charpak, S. D.; Dumont, G.; Buschman, R.; Buse, N.; Denison, T.; van Nes, I.; Asboth, L.; Watrin, A.; Struber, L.; Sauter-Starace, F.; Langar, L.; Auboiroux, V.; Carda, S.; Chabardes, S.; Aksenova, T.; Demesmaeker, R.; Charvet, G.; Bloch, J.; Courtine, G. Walking Naturally after Spinal Cord Injury Using a Brain–Spine Interface. *Nature* **2023**, *618* (7963), 126–133. https://doi.org/10.1038/s41586-023-06094-5.

(55) Niyonambaza, S. D.; Kumar, P.; Xing, P.; Mathault, J.; Koninck, P. de; Boisselier, E.; Boukadoum, M.; Miled, A. A Review of Neurotransmitters Sensing Methods for Neuro-

Engineering Research. *Applied Sciences 2019, Vol. 9, Page 4719* **2019**, *9* (21), 4719. https://doi.org/10.3390/APP9214719.

(56) Wu, F.; Yu, P.; Mao, L. Analytical and Quantitative in Vivo Monitoring of Brain Neurochemistry by Electrochemical and Imaging Approaches. *ACS Omega* **2018**, *3* (10), 13267–13274. https://doi.org/10.1021/ACSOMEGA.8B02055.

(57) *Electrophysiology Fundamentals, Membrane Potential and Electrophysiological Techniques | Technology Networks*. https://www.technologynetworks.com/neuroscience/application-notes/optimizing-metabolite-identification-with-electron-activated-dissociation-398091 (2025).

(58) Cardozo, D. An Intuitive Approach to Understanding the Resting Membrane Potential. *Adv Physiol Educ* **2016**, *40* (4), 543–547. https://doi.org/10.1152/advan.00049.2016.

(59) *Goldman-Hodgkin-Katz Equation Calculator - PhysiologyWeb*. https://www.physiologyweb.com/calculators/ghk_equation_calculator.html (2025).

(60) Powell, C. L.; Brown, A. M. A Classic Experiment Revisited: Membrane Permeability Changes during the Action Potential. *Adv Physiol Educ* **2021**, *45* (1), 178–181. https://doi.org/10.1152/advan.00188.2020.

(61) Brown, A. M. Flowcharts to Aid Student Comprehension of Nernst Equation Calculations. *Adv Physiol Educ* **2018**, *42* (2), 260–262. https://doi.org/10.1152/advan.00006.2018.

(62) *Resting Membrane Potential - Nernst - Generation - TeachMePhysiology*. https://teachmephysiology.com/nervous-system/synapses/resting-membrane-potential/#Resting_Membrane_Potential_Generation (2025).

(63) Crowther, G. J. Which Way Do the Ions Go? A Graph-Drawing Exercise for Understanding Electrochemical Gradients. *Adv Physiol Educ* **2017**, *41* (4), 556–559. https://doi.org/10.1152/advan.00111.2017.

(64) Archer, M. D. Genesis of the Nernst Equation; 1989; pp 115–126. https://doi.org/10.1021/bk-1989-0390.ch008.

(65) Bean, B. P. The Action Potential in Mammalian Central Neurons. *Nature Reviews Neuroscience 2007 8:6* **2007**, *8* (6), 451–465. https://doi.org/10.1038/nrn2148.

(66) Gregory, B. A.; Thompson, C. H.; Salatino, J. W.; Railing, M. J.; Zimmerman, A. F.; Gupta, B.; Williams, K.; Beatty, J. A.; Cox, C. L.; Purcell, E. K. Structural and Functional Changes of Deep Layer Pyramidal Neurons Surrounding Microelectrode Arrays Implanted in Rat Motor Cortex. *Acta Biomater* **2023**, *168*, 429–439. https://doi.org/10.1016/j.actbio.2023.07.027.

(67) Al-Sabi, A.; McArthur, J.; Ostroumov, V.; French, R. J. Marine Toxins That Target Voltage-Gated Sodium Channels. *Mar Drugs* **2006**, *4* (3), 157–192. https://doi.org/10.3390/md403157.

(68) Buzsáki, G.; Anastassiou, C. A.; Koch, C. The Origin of Extracellular Fields and Currents — EEG, ECoG, LFP and Spikes. *Nat Rev Neurosci* **2012**, *13* (6), 407–420. https://doi.org/10.1038/nrn3241.

(69) Herreras, O. Local Field Potentials: Myths and Misunderstandings. *Front Neural Circuits* **2016**, *10*. https://doi.org/10.3389/fncir.2016.00101.

(70) Ahmadi, N.; Constandinou, T. G.; Bouganis, C.-S. Inferring Entire Spiking Activity from Local Field Potentials. *Sci Rep* **2021**, *11* (1), 19045. https://doi.org/10.1038/s41598-021-98021-9.

(71) Jung, Y. J.; Sun, S. H.; Almasi, A.; Yunzab, M.; Meffin, H.; Ibbotson, M. R. Characterization of Extracellular Spike Waveforms Recorded in Wallaby Primary Visual Cortex. *Front Neurosci* **2023**, *17*. https://doi.org/10.3389/fnins.2023.1244952.

(72) Borroto-Escuela, D. O.; Gonzalez-Cristo, E.; Ochoa-Torres, V.; Serra-Rojas, E. M.; Ambrogini, P.; Arroyo-García, L. E.; Fuxe, K. Understanding Electrical and Chemical Transmission in the Brain. *Front Cell Neurosci* **2024**, *18*. https://doi.org/10.3389/fncel.2024.1398862.

(73) Bucher, E. S.; Wightman, R. M. Electrochemical Analysis of Neurotransmitters. *Annu Rev Anal Chem (Palo Alto Calif)* **2015**, *8*, 239–261. https://doi.org/10.1146/ANNUREV-ANCHEM-071114-040426.

(74) Adeloju, S. B. Amperometry. *Encyclopedia of Analytical Science: Second Edition* **2004**, 70–79. https://doi.org/10.1016/B0-12-369397-7/00012-1.

(75) Wightman, R. M.; Jankowski, J. A.; Kennedy, R. T.; Kawagoe, K. T.; Schroeder, T. J.; Leszczyszyn, D. J.; Near, J. A.; Diliberto, E. J.; Viveros, O. H. Temporally Resolved Catecholamine Spikes Correspond to Single Vesicle Release from Individual Chromaffin Cells. *Proc Natl Acad Sci U S A* **1991**, *88* (23), 10754–10758. https://doi.org/10.1073/pnas.88.23.10754.

(76) Zhao, H.; Bian, X.; Galligan, J. J.; Swain, G. M. Electrochemical Measurements of Serotonin (5-HT) Release from the Guinea Pig Mucosa Using Continuous Amperometry with a Boron-Doped Diamond Microelectrode. *Diam Relat Mater* **2010**, *19* (2–3), 182–185. https://doi.org/10.1016/J.DIAMOND.2009.10.004.

(77) Pothos, E. N.; Davila, V.; Sulzer, D. Presynaptic Recording of Quanta from Midbrain Dopamine Neurons and Modulation of the Quantal Size. *J Neurosci* **1998**, *18* (11), 4106–4118. https://doi.org/10.1523/JNEUROSCI.18-11-04106.1998.

(78) de Toledo, G. A.; Fernández-Chacón, R.; Fernández, J. M. Release of Secretory Products during Transient Vesicle Fusion. *Nature* **1993**, *363* (6429), 554–558. https://doi.org/10.1038/363554A0.

(79) Huang, L.; Shen, H.; Atkinson, M. A.; Kennedy, R. T. Detection of Exocytosis at Individual Pancreatic Beta Cells by Amperometry at a Chemically Modified Microelectrode. *Proc Natl Acad Sci U S A* **1995**, *92* (21), 9608–9612. https://doi.org/10.1073/PNAS.92.21.9608.

(80) Mosharov, E. v.; Sulzer, D. Analysis of Exocytotic Events Recorded by Amperometry. *Nat Methods* **2005**, *2* (9), 651–658. https://doi.org/10.1038/NMETH782.

(81) Bard, A. J.; Faulkner, L. R. *Electrochemical Methods: Fundamentals and Applications*, Second.; John Wiley & Sons, Inc.: New York, 2001.

(82) Venton, B. J.; DiScenza, D. J. Voltammetry. *Electrochemistry for Bioanalysis* **2020**, 27–50. https://doi.org/10.1016/B978-0-12-821203-5.00004-X.

(83) Venton, B. J.; Cao, Q. Fundamentals of Fast-Scan Cyclic Voltammetry for Dopamine Detection †. *CRITICAL REVIEW Cite this: Analyst* **2020**, *145*, 1158. https://doi.org/10.1039/c9an01586h.

(84) *7.5: Voltammetric Methods - Chemistry LibreTexts*. chem.libretexts.org/Bookshelves/Analytical_Chemistry/Supplemental_Modules_(Analytical_Chemistry)/Analytical_Sciences_Digital_Library/Active_Learning/In_Class_Activities/Electrochemical_Methods_of_Analysis/02_Text/7%253A_Electrochemical_Analytical_Methods/7.5%253A_Voltammetric_Methods (2022).

(85) Kissinger, P. T.; Heineman, W. R. Cyclic Voltammetry. *J Chem Educ* **1983**, *60* (9), 702–706. https://doi.org/10.1021/ED060P702.

(86) Elgrishi, N.; Rountree, K. J.; McCarthy, B. D.; Rountree, E. S.; Eisenhart, T. T.; Dempsey, J. L. A Practical Beginner's Guide to Cyclic Voltammetry. *J Chem Educ* **2018**, *95* (2), 197–206. https://doi.org/10.1021/ACS.JCHEMED.7B00361/SUPPL_FILE/ED7B00361_SI_002.DOCX.

(87) Kissinger, P. T.; Hart, J. B.; Adams, R. N. Voltammetry in Brain Tissue--a New Neurophysiological Measurement. *Brain Res* **1973**, *55* (1), 209–213. https://doi.org/10.1016/0006-8993(73)90503-9.

(88) Tan, S. Y.; Chia, V. Y. Y.; Hölttä-Otto, K.; Anariba, F. Teaching the Nernst Equation and Faradaic Current through the Use of a *Designette:* An Opportunity to Strengthen Key Electrochemical Concepts and Clarify Misconceptions. *J Chem Educ* **2020**, *97* (8), 2238–2243. https://doi.org/10.1021/acs.jchemed.9b00932.

(89) Puthongkham, P.; Venton, B. J. Recent Advances in Fast-Scan Cyclic Voltammetry. *Analyst* **2020**, *145* (4), 1087–1102. https://doi.org/10.1039/C9AN01925A.

(90) Dong, H.; Wang, S.; Galligan, J. J.; Swain, G. M. *Boron-Doped Diamond Nano/Microelectrodes for Biosensing and in Vitro Measurements*; 2011; Vol. 3.

(91) Deakin, M. R.; Wightman, R. M.; Amatore, C. A. Electrochemical Kinetics at Microelectrodes. *J Electroanal Chem Interfacial Electrochem* **1986**, *215* (1–2), 49–61. https://doi.org/10.1016/0022-0728(86)87004-8.

(92) Bath, B. D.; Michael, D. J.; Trafton, B. J.; Joseph, J. D.; Runnels, P. L.; Wightman, R. M. Subsecond Adsorption and Desorption of Dopamine at Carbon-Fiber Microelectrodes. *Anal Chem* **2000**, *72* (24), 5994–6002. https://doi.org/10.1021/ac000849y.

(93) Heien, M. L. A. v.; Phillips, P. E. M.; Stuber, G. D.; Seipel, A. T.; Wightman, R. M. Overoxidation of Carbon-Fiber Microelectrodes Enhances Dopamine Adsorption and Increases Sensitivity. *Analyst* **2003**, *128* (12), 1413. https://doi.org/10.1039/b307024g.

(94) Kennedy, R. T.; Jones, S. R.; Wightman, R. M. Simultaneous Measurement of Oxygen and Dopamine: Coupling of Oxygen Consumption and Neurotransmission. *Neuroscience* **1992**, *47* (3), 603–612. https://doi.org/10.1016/0306-4522(92)90169-3.

(95) Wang, Y.; Venton, B. J. Correlation of Transient Adenosine Release and Oxygen Changes in the Caudate-Putamen. *J Neurochem* **2017**, *140* (1), 13–23. https://doi.org/10.1111/jnc.13705.

(96) Takmakov, P.; Zachek, M. K.; Keithley, R. B.; Walsh, P. L.; Donley, C.; McCarty, G. S.; Wightman, R. M. Carbon Microelectrodes with a Renewable Surface. *Anal Chem* **2010**, *82* (5), 2020–2028. https://doi.org/10.1021/ac902753x.

(97) Jackson, B. P.; Dietz, S. M.; Wightman, R. Mark. Fast-Scan Cyclic Voltammetry of 5-Hydroxytryptamine. *Anal Chem* **1995**, *67* (6), 1115–1120. https://doi.org/10.1021/ac00102a015.

(98) Purcell, E. K.; Becker, M. F.; Guo, Y.; Hara, S. A.; Ludwig, K. A.; McKinney, C. J.; Monroe, E. M.; Rechenberg, R.; Rusinek, C. A.; Saxena, A.; Siegenthaler, J. R.; Sortwell, C. E.; Thompson, C. H.; Trevathan, J. K.; Witt, S.; Li, W. Next-Generation Diamond Electrodes for Neurochemical Sensing: Challenges and Opportunities. *Micromachines (Basel)* **2021**, *12* (2), 1–29. https://doi.org/10.3390/MI12020128.

(99) Dunham, K. E.; Venton, B. J. Improving Serotonin Fast-Scan Cyclic Voltammetry Detection: New Waveforms to Reduce Electrode Fouling. *Analyst* **2020**, *145* (22), 7437–7446. https://doi.org/10.1039/D0AN01406K.

(100) Singh, Y. S.; Sawarynski, L. E.; Dabiri, P. D.; Choi, W. R.; Andrews, A. M. Head-to-Head Comparisons of Carbon Fiber Microelectrode Coatings for Sensitive and Selective Neurotransmitter Detection by Voltammetry. *Anal Chem* **2011**, *83* (17), 6658. https://doi.org/10.1021/AC2011729.

(101) Bucher, E. S.; Brooks, K.; Verber, M. D.; Keithley, R. B.; Owesson-White, C.; Carroll, S.; Takmakov, P.; McKinney, C. J.; Wightman, R. M. Flexible Software Platform for Fast-Scan Cyclic Voltammetry Data Acquisition and Analysis. *Anal Chem* **2013**, *85* (21), 10344–10353.

(102) Im, C.; Seo, J.-M. A Review of Electrodes for the Electrical Brain Signal Recording. *Biomed Eng Lett* **2016**, *6* (3), 104–112. https://doi.org/10.1007/s13534-016-0235-1.

(103) Mora Lopez, C.; Putzeys, J.; Raducanu, B. C.; Ballini, M.; Wang, S.; Andrei, A.; Rochus, V.; Vandebriel, R.; Severi, S.; Van Hoof, C.; Musa, S.; Van Helleputte, N.; Yazicioglu, R. F.; Mitra, S. A Neural Probe With Up to 966 Electrodes and Up to 384 Configurable Channels in 0.13 µm SOI CMOS. *IEEE Trans Biomed Circuits Syst* **2017**, *11* (3), 510–522. https://doi.org/10.1109/TBCAS.2016.2646901.

(104) Jun, J. J.; Steinmetz, N. A.; Siegle, J. H.; Denman, D. J.; Bauza, M.; Barbarits, B.; Lee, A. K.; Anastassiou, C. A.; Andrei, A.; Aydın, Ç.; Barbic, M.; Blanche, T. J.; Bonin, V.; Couto, J.; Dutta, B.; Gratiy, S. L.; Gutnisky, D. A.; Häusser, M.; Karsh, B.; Ledochowitsch, P.; Lopez, C. M.; Mitelut, C.; Musa, S.; Okun, M.; Pachitariu, M.; Putzeys, J.; Rich, P. D.; Rossant, C.; Sun, W.; Svoboda, K.; Carandini, M.; Harris, K. D.; Koch, C.; O'Keefe, J.; Harris, T. D. Fully Integrated Silicon Probes for High-Density Recording of Neural Activity. *Nature* **2017**, *551* (7679), 232–236. https://doi.org/10.1038/nature24636.

(105) Huijing Xu; Weltman, A.; Min-Chi Hsiao; Scholten, K.; Meng, E.; Berger, T. W.; Dong Song. Design of a Flexible Parylene-Based Multi-Electrode Array for Multi-Region Recording from the Rat Hippocampus. In *2015 37th Annual International Conference of the IEEE Engineering in Medicine and Biology Society (EMBC)*; IEEE, 2015; pp 7139–7142. https://doi.org/10.1109/EMBC.2015.7320038.

(106) Xu, H.; Weltman, A.; Scholten, K.; Meng, E.; Berger, T. W.; Song, D. Chronic Multi-Region Recording from the Rat Hippocampus in Vivo with a Flexible Parylene-Based Multi-Electrode Array. In *2017 39th Annual International Conference of the IEEE Engineering in Medicine and Biology Society (EMBC)*; IEEE, 2017; pp 1716–1719. https://doi.org/10.1109/EMBC.2017.8037173.

(107) Hara, S. A.; Kim, B. J.; Kuo, J. T. W.; Lee, C. D.; Meng, E.; Pikov, V. Long-Term Stability of Intracortical Recordings Using Perforated and Arrayed Parylene Sheath Electrodes. *J Neural Eng* **2016**, *13* (6), 066020. https://doi.org/10.1088/1741-2560/13/6/066020.

(108) Seymour, J. P.; Kipke, D. R. Neural Probe Design for Reduced Tissue Encapsulation in CNS. *Biomaterials* **2007**, *28* (25), 3594–3607. https://doi.org/10.1016/j.biomaterials.2007.03.024.

(109) Purcell, E. K.; Seymour, J. P.; Yandamuri, S.; Kipke, D. R. In Vivo Evaluation of a Neural Stem Cell-Seeded Prosthesis. *J Neural Eng* **2009**, *6* (2), 026005. https://doi.org/10.1088/1741-2560/6/2/026005.

(110) Wei, X.; Luan, L.; Zhao, Z.; Li, X.; Zhu, H.; Potnis, O.; Xie, C. Nanofabricated Ultraflexible Electrode Arrays for High-Density Intracortical Recording. *Advanced Science* **2018**, *5* (6). https://doi.org/10.1002/advs.201700625.

(111) Jarošová, R.; De Sousa Bezerra, P. M.; Munson, C.; Swain, G. M. Assessment of Heterogeneous Electron-transfer Rate Constants for Soluble Redox Analytes at Tetrahedral Amorphous Carbon, Boron-doped Diamond, and Glassy Carbon Electrodes. *physica status solidi (a)* **2016**, *213* (8), 2087–2098. https://doi.org/10.1002/pssa.201600339.

(112) Yang, C.; Denno, M. E.; Pyakurel, P.; Venton, B. J. Recent Trends in Carbon Nanomaterial-Based Electrochemical Sensors for Biomolecules: A Review. *Anal Chim Acta* **2015**, *887*, 17–37. https://doi.org/10.1016/j.aca.2015.05.049.

(113) Xiao, T.; Jiang, Y.; Ji, W.; Mao, L. Controllable and Reproducible Sheath of Carbon Fibers with Single-Walled Carbon Nanotubes through Electrophoretic Deposition for In Vivo Electrochemical Measurements. *Anal Chem* **2018**, *90* (7), 4840–4846. https://doi.org/10.1021/acs.analchem.8b00303.

(114) Perillo, M. L.; Gupta, B.; Saxena, A.; Veltri, A. P.; Li, W.; Siegenthaler, J. R.; Purcell, E. K. Biological and Mechanical Limitations for Chronic Fast-Scan Cyclic Voltammetry Sensor Design. *Adv Mater Technol* **2025**. https://doi.org/10.1002/admt.202401808.

(115) Fabbro, A.; Prato, M.; Ballerini, L. Carbon Nanotubes in Neuroregeneration and Repair. *Adv Drug Deliv Rev* **2013**, *65* (15), 2034–2044. https://doi.org/10.1016/j.addr.2013.07.002.

(116) Keefer, E. W.; Botterman, B. R.; Romero, M. I.; Rossi, A. F.; Gross, G. W. Carbon Nanotube Coating Improves Neuronal Recordings. *Nat Nanotechnol* **2008**, *3* (7), 434–439. https://doi.org/10.1038/nnano.2008.174.

(117) Chae, S. H.; Lee, Y. H. Carbon Nanotubes and Graphene towards Soft Electronics. *Nano Converg* **2014**, *1* (1), 15. https://doi.org/10.1186/s40580-014-0015-5.

(118) Herbert, R.; Jeong, J.-W.; Yeo, W.-H. Soft Material-Enabled Electronics for Medicine, Healthcare, and Human-Machine Interfaces. *Materials* **2020**, *13* (3), 517. https://doi.org/10.3390/ma13030517.

(119) Koehne, J. E.; Marsh, M.; Boakye, A.; Douglas, B.; Kim, I. Y.; Chang, S.-Y.; Jang, D.-P.; Bennet, K. E.; Kimble, C.; Andrews, R.; Meyyappan, M.; Lee, K. H. Carbon Nanofiber Electrode Array for Electrochemical Detection of Dopamine Using Fast Scan Cyclic Voltammetry. *Analyst* **2011**, *136* (9), 1802. https://doi.org/10.1039/c1an15025a.

(120) Power, A. C.; Gorey, B.; Chandra, S.; Chapman, J. Carbon Nanomaterials and Their Application to Electrochemical Sensors: A Review. *Nanotechnol Rev* **2018**, *7* (1), 19–41. https://doi.org/10.1515/ntrev-2017-0160.

(121) della Valle, E.; Koo, B.; Patel, P. R.; Whitsitt, Q.; Purcell, E. K.; Chestek, C. A.; Weiland, J. D. Electrodeposited Platinum Iridium Enables Microstimulation With Carbon Fiber Electrodes. *Frontiers in Nanotechnology* **2021**, *3*. https://doi.org/10.3389/fnano.2021.782883.

(122) Schrand, A. M.; Huang, H.; Carlson, C.; Schlager, J. J.; Ōsawa, E.; Hussain, S. M.; Dai, L. Are Diamond Nanoparticles Cytotoxic? *J Phys Chem B* **2007**, *111* (1), 2–7. https://doi.org/10.1021/jp066387v.

(123) Kim, T.; Cho, M.; Yu, K. Flexible and Stretchable Bio-Integrated Electronics Based on Carbon Nanotube and Graphene. *Materials* **2018**, *11* (7), 1163. https://doi.org/10.3390/ma11071163.

(124) Sahni, D.; Jea, A.; Mata, J. A.; Marcano, D. C.; Sivaganesan, A.; Berlin, J. M.; Tatsui, C. E.; Sun, Z.; Luerssen, T. G.; Meng, S.; Kent, T. A.; Tour, J. M. Biocompatibility of Pristine Graphene for Neuronal Interface. *J Neurosurg Pediatr* **2013**, *11* (5), 575–583. https://doi.org/10.3171/2013.1.PEDS12374.

(125) Edgington, R. J.; Thalhammer, A.; Welch, J. O.; Bongrain, A.; Bergonzo, P.; Scorsone, E.; Jackman, R. B.; Schoepfer, R. Patterned Neuronal Networks Using Nanodiamonds and the Effect of Varying Nanodiamond Properties on Neuronal Adhesion and Outgrowth. *J Neural Eng* **2013**, *10* (5), 056022. https://doi.org/10.1088/1741-2560/10/5/056022.

(126) Puthongkham, P.; Venton, B. J. Nanodiamond Coating Improves the Sensitivity and Antifouling Properties of Carbon Fiber Microelectrodes. *ACS Sens* **2019**, *4* (9), 2403–2411. https://doi.org/10.1021/acssensors.9b00994.

(127) Furtado, D.; Björnmalm, M.; Ayton, S.; Bush, A. I.; Kempe, K.; Caruso, F. Overcoming the Blood–Brain Barrier: The Role of Nanomaterials in Treating Neurological Diseases. *Advanced Materials* **2018**, *30* (46). https://doi.org/10.1002/adma.201801362.

(128) Zhao, N.; Francis, N. L.; Calvelli, H. R.; Moghe, P. V. Microglia-Targeting Nanotherapeutics for Neurodegenerative Diseases. *APL Bioeng* **2020**, *4* (3). https://doi.org/10.1063/5.0013178.

(129) Fischer, A. E.; Show, Y.; Swain, G. M. Electrochemical Performance of Diamond Thin-Film Electrodes from Different Commercial Sources. *Anal Chem* **2004**, *76* (9), 2553–2560. https://doi.org/10.1021/ac035214o.

(130) Jarošová, R.; De Sousa Bezerra, P. M.; Munson, C.; Swain, G. M. Assessment of Heterogeneous Electron-transfer Rate Constants for Soluble Redox Analytes at Tetrahedral Amorphous Carbon, Boron-doped Diamond, and Glassy Carbon Electrodes. *physica status solidi (a)* **2016**, *213* (8), 2087–2098. https://doi.org/10.1002/pssa.201600339.

(131) Jarošová, R.; Sanchez, S.; Haubold, L.; Swain, G. M. Isatin Analysis Using Flow Injection Analysis with Amperometric Detection – Comparison of Tetrahedral Amorphous Carbon and Diamond Electrode Performance. *Electroanalysis* **2017**, *29* (9), 2147–2154. https://doi.org/10.1002/elan.201700272.

(132) Purcell, E.; Becker, M.; Guo, Y.; Hara, S.; Ludwig, K.; McKinney, C.; Monroe, E.; Rechenberg, R.; Rusinek, C.; Saxena, A.; Siegenthaler, J.; Sortwell, C.; Thompson, C.; Trevathan, J.; Witt, S.; Li, W. Next-Generation Diamond Electrodes for Neurochemical Sensing: Challenges and Opportunities. *Micromachines (Basel)* **2021**, *12* (2), 128. https://doi.org/10.3390/mi12020128.

(133) Fan, B.; Rusinek, C. A.; Thompson, C. H.; Setien, M.; Guo, Y.; Rechenberg, R.; Gong, Y.; Weber, A. J.; Becker, M. F.; Purcell, E.; Li, W. Flexible, Diamond-Based Microelectrodes Fabricated Using the Diamond Growth Side for Neural Sensing. *Microsyst Nanoeng* **2020**, *6* (1), 42. https://doi.org/10.1038/s41378-020-0155-1.

(134) Yence, M.; Cetinkaya, A.; Ozcelikay, G.; Kaya, S. I.; Ozkan, S. A. Boron-Doped Diamond Electrodes: Recent Developments and Advances in View of Electrochemical Drug Sensors. *Crit Rev Anal Chem* **2022**, *52* (5), 1122–1138. https://doi.org/10.1080/10408347.2020.1863769.

(135) Bennet, K. E.; Tomshine, J. R.; Min, H.-K.; Manciu, F. S.; Marsh, M. P.; Paek, S. B.; Settell, M. L.; Nicolai, E. N.; Blaha, C. D.; Kouzani, A. Z.; Chang, S.-Y.; Lee, K. H. A Diamond-Based Electrode for Detection of Neurochemicals in the Human Brain. *Front Hum Neurosci* **2016**, *10*. https://doi.org/10.3389/fnhum.2016.00102.

(136) Chestek, C. A.; Cunningham, J. P.; Gilja, V.; Nuyujukian, P.; Ryu, S. I.; Shenoy, K. V. Neural Prosthetic Systems: Current Problems and Future Directions. *Annu Int Conf IEEE Eng Med Biol Soc* **2009**, *2009*, 3369–3375. https://doi.org/10.1109/IEMBS.2009.5332822.

(137) Seaton, B. T.; Hill, D. F.; Cowen, S. L.; Heien, M. L. Mitigating the Effects of Electrode Biofouling-Induced Impedance for Improved Long-Term Electrochemical Measurements In Vivo. *Anal Chem* **2020**, *92* (9), 6334–6340. https://doi.org/10.1021/acs.analchem.9b05194.

(138) Perge, J. A.; Homer, M. L.; Malik, W. Q.; Cash, S.; Eskandar, E.; Friehs, G.; Donoghue, J. P.; Hochberg, L. R. Intra-Day Signal Instabilities Affect Decoding Performance in an Intracortical Neural Interface System. *J Neural Eng* **2013**, *10* (3), 036004. https://doi.org/10.1088/1741-2560/10/3/036004.

(139) Prasad, A.; Sanchez, J. C. Quantifying Long-Term Microelectrode Array Functionality Using Chronic in Vivo Impedance Testing. *J Neural Eng* **2012**, *9* (2), 026028. https://doi.org/10.1088/1741-2560/9/2/026028.

(140) McCreery, D. B.; Agnew, W. F.; Bullara, L. A. The Effects of Prolonged Intracortical Microstimulation on the Excitability of Pyramidal Tract Neurons in the Cat. *Ann Biomed Eng* **2002**, *30* (1), 107–119. https://doi.org/10.1114/1.1430748.

(141) Ryu, S. I.; Shenoy, K. V. Human Cortical Prostheses: Lost in Translation? *Neurosurg Focus* **2009**, *27* (1). https://doi.org/10.3171/2009.4.FOCUS0987.

(142) Kozai, T. D. Y.; Catt, K.; Li, X.; Gugel, Z. V.; Olafsson, V. T.; Vazquez, A. L.; Cui, X. T. Mechanical Failure Modes of Chronically Implanted Planar Silicon-Based Neural Probes for Laminar Recording. *Biomaterials* **2015**, *37*, 25–39. https://doi.org/10.1016/J.BIOMATERIALS.2014.10.040.

(143) Joseph, K.; Kirsch, M.; Johnston, M.; Münkel, C.; Stieglitz, T.; Haas, C. A.; Hofmann, U. G. Transcriptional Characterization of the Glial Response Due to Chronic Neural Implantation of Flexible Microprobes. *Biomaterials* **2021**, *279*. https://doi.org/10.1016/J.BIOMATERIALS.2021.121230.

(144) Partouche, E.; Adenis, V.; Gnansia, D.; Stahl, P.; Edeline, J.-M. Increased Threshold and Reduced Firing Rate of Auditory Cortex Neurons after Cochlear Implant Insertion. *Brain Sci* **2022**, *12* (2), 205. https://doi.org/10.3390/brainsci12020205.

(145) Grill, W. M. *Signal Considerations for Chronically Implanted Electrodes for Brain Interfacing*; 2008.

(146) Biran, R.; Martin, D. C.; Tresco, P. A. Neuronal Cell Loss Accompanies the Brain Tissue Response to Chronically Implanted Silicon Microelectrode Arrays. *Exp Neurol* **2005**, *195* (1), 115–126. https://doi.org/10.1016/J.EXPNEUROL.2005.04.020.

(147) Chestek, C. A.; Gilja, V.; Nuyujukian, P.; Foster, J. D.; Fan, J. M.; Kaufman, M. T.; Churchland, M. M.; Rivera-Alvidrez, Z.; Cunningham, J. P.; Ryu, S. I.; Shenoy, K. V. Long-Term Stability of Neural Prosthetic Control Signals from Silicon Cortical Arrays in Rhesus Macaque Motor Cortex. *J Neural Eng* **2011**, *8* (4), 045005. https://doi.org/10.1088/1741-2560/8/4/045005.

(148) Purcell, E. K.; Thompson, D. E.; Ludwig, K. A.; Kipke, D. R. Flavopiridol Reduces the Impedance of Neural Prostheses in Vivo without Affecting Recording Quality. *J Neurosci Methods* **2009**, *183* (2), 149–157. https://doi.org/10.1016/J.JNEUMETH.2009.06.026.

(149) Perge, J. A.; Homer, M. L.; Malik, W. Q.; Cash, S.; Eskandar, E.; Friehs, G.; Donoghue, J. P.; Hochberg, L. R. Intra-Day Signal Instabilities Affect Decoding Performance in an Intracortical Neural Interface System. *J Neural Eng* **2013**, *10* (3). https://doi.org/10.1088/1741-2560/10/3/036004.

(150) Patel, P. R.; Welle, E. J.; Letner, J. G.; Shen, H.; Bullard, A. J.; Caldwell, C. M.; Vega-Medina, A.; Richie, J. M.; Thayer, H. E.; Patil, P. G.; Cai, D.; Chestek, C. A. Utah Array Characterization and Histological Analysis of a Multi-Year Implant in Non-Human Primate Motor and Sensory Cortices. *J Neural Eng* **2023**, *20* (1), 014001. https://doi.org/10.1088/1741-2552/acab86.

(151) Hashemi, P.; Dankoski, E. C.; Petrovic, J.; Keithley, R. B.; Wightman, R. M. Voltammetric Detection of 5-Hydroxytryptamine Release in the Rat Brain. *Anal Chem* **2009**, *81* (22), 9462–9471. https://doi.org/10.1021/AC9018846.

(152) Logman, M. J.; Budygin, E. A.; Gainetdinov, R. R.; Wightman, R. M. Quantitation of in Vivo Measurements with Carbon Fiber Microelectrodes. *J Neurosci Methods* **2000**, *95* (2), 95–102. https://doi.org/10.1016/S0165-0270(99)00155-7.

(153) Carnicer-Lombarte, A.; Chen, S.-T.; Malliaras, G. G.; Barone, D. G. Foreign Body Reaction to Implanted Biomaterials and Its Impact in Nerve Neuroprosthetics. *Front Bioeng Biotechnol* **2021**, *9*. https://doi.org/10.3389/fbioe.2021.622524.

(154) Kozai, T. D. Y.; Vazquez, A. L.; Weaver, C. L.; Kim, S.-G.; Cui, X. T. In Vivo Two-Photon Microscopy Reveals Immediate Microglial Reaction to Implantation of Microelectrode through Extension of Processes. *J Neural Eng* **2012**, *9* (6), 066001. https://doi.org/10.1088/1741-2560/9/6/066001.

(155) Salatino, J. W.; Ludwig, K. A.; Kozai, T. D. Y.; Purcell, E. K. Glial Responses to Implanted Electrodes in the Brain. *Nat Biomed Eng* **2017**, *1* (11), 862–877. https://doi.org/10.1038/S41551-017-0154-1.

(156) Patel, P. R.; Welle, E. J.; Letner, J. G.; Shen, H.; Bullard, A. J.; Caldwell, C. M.; Vega-Medina, A.; Richie, J. M.; Thayer, H. E.; Patil, P. G.; Cai, D.; Chestek, C. A. Utah Array Characterization and Histological Analysis of a Multi-Year Implant in Non-Human Primate Motor and Sensory Cortices. *J Neural Eng* **2023**, *20* (1), 014001. https://doi.org/10.1088/1741-2552/acab86.

(157) Subbaroyan, J.; Martin, D. C.; Kipke, D. R. A Finite-Element Model of the Mechanical Effects of Implantable Microelectrodes in the Cerebral Cortex. *J Neural Eng* **2005**, *2* (4), 103–113. https://doi.org/10.1088/1741-2560/2/4/006.

(158) Rodeberg, N. T.; Sandberg, S. G.; Johnson, J. A.; Phillips, P. E. M.; Wightman, R. M. Hitchhiker's Guide to Voltammetry: Acute and Chronic Electrodes for in Vivo Fast-Scan Cyclic Voltammetry. *ACS Chem Neurosci* **2017**, *8* (2), 221–234. https://doi.org/10.1021/acschemneuro.6b00393.

(159) Roberts, J. G.; Moody, B. P.; McCarty, G. S.; Sombers, L. A. Specific Oxygen-Containing Functional Groups on the Carbon Surface Underlie an Enhanced Sensitivity to Dopamine at Electrochemically Pretreated Carbon Fiber Microelectrodes. *Langmuir* **2010**, *26* (11), 9116–9122. https://doi.org/10.1021/la9048924.

(160) Michelson, N. J.; Vazquez, A. L.; Eles, J. R.; Salatino, J. W.; Purcell, E. K.; Williams, J. J.; Cui, X. T.; Kozai, T. D. Y. Multi-Scale, Multi-Modal Analysis Uncovers Complex Relationship at the Brain Tissue-Implant Neural Interface: New Emphasis on the Biological Interface. *J Neural Eng* **2018**, *15* (3). https://doi.org/10.1088/1741-2552/AA9DAE.

(161) Marx, V. Method of the Year: Spatially Resolved Transcriptomics. *Nat Methods* **2021**, *18* (1), 9–14. https://doi.org/10.1038/s41592-020-01033-y.

(162) Whitsitt, Q. A.; Patel, B.; Hunt, B.; Purcell, E. K. A Spatial Transcriptomics Study of the Brain-Electrode Interface in Rat Motor Cortex. *bioRxiv* **2021**, 2021.12.03.471147. https://doi.org/10.1101/2021.12.03.471147.

(163) Whitsitt, Q. A.; Koo, B.; Celik, M. E.; Evans, B. M.; Weiland, J. D.; Purcell, E. K. Spatial Transcriptomics as a Novel Approach to Redefine Electrical Stimulation Safety. *Front Neurosci* **2022**, *16*. https://doi.org/10.3389/fnins.2022.937923.

(164) Thompson, C. H.; Saxena, A.; Heelan, N.; Salatino, J.; Purcell, E. K. Spatiotemporal Patterns of Gene Expression around Implanted Silicon Electrode Arrays. *J Neural Eng* **2021**, *18* (4), 045005. https://doi.org/10.1088/1741-2552/abf2e6.

(165) Moore, M. G.; Thompson, C. H.; Reimers, M. A.; Purcell, E. K. Differential Co-Expression Analysis of RNA-Seq Data Reveals Novel Potential Biomarkers of Device-Tissue Interaction. In *2022 44th Annual International Conference of the IEEE Engineering in Medicine & Biology Society (EMBC)*; IEEE, 2022; pp 3072–3076. https://doi.org/10.1109/EMBC48229.2022.9871437.

(166) Whitsitt, Q.; Saxena, A.; Patel, B.; Evans, B. M.; Hunt, B.; Purcell, E. K. Spatial Transcriptomics at the Brain-Electrode Interface in Rat Motor Cortex and the Relationship to Recording Quality. *J Neural Eng* **2024**, *21* (4), 046033. https://doi.org/10.1088/1741-2552/ad5936.

(167) ACD Labs. ChemSketch. Www.Acdlabs.Com. Ontario, Canada.

(168) Gupta, B.; Saxena, A.; Perillo, M. L.; Wade-Kleyn, L. C.; Thompson, C. H.; Purcell, E. K. Structural, Functional, and Genetic Changes Surrounding Electrodes Implanted in the Brain. *Acc Chem Res* **2024**, *57* (9), 1346–1359. https://doi.org/10.1021/acs.accounts.4c00057.

# CHAPTER 2 | ALL-DIAMOND BORON-DOPED DIAMOND MICROELECTRODES FOR NEUROCHEMICAL SENSING WITH FAST-SCAN CYCLIC VOLTAMMETRY

## 2.1 INTRODUCTION

Implantable electrodes that can be integrated with biological tissue to monitor and deliver electrical or chemical signals have gained increasing interest in the study of neurological disorders[1–4]. Such microelectrodes and microelectrode arrays have allowed for neural stimulation as well as acute and chronic recordings to better understand, diagnose and treat diseases such as epilepsy, Parkinson's disease, and depression[5–7]. Recent advances in electrode development have largely focused on electrophysiological, optical, stimulating or hybrid approaches to study electrical activity in the brain[8–10]. In contrast, current progress with sensors to examine real-time and long-term chemical signaling in living systems is relatively limited and challenging[2]. Electrochemical sensors targeted to detect neurotransmitters in physiological environments, such as the brain, face major issues including selective identification of analytes, long-term electrode stability, sparse distribution of neural circuitries and signal loss due to protein adsorption related surface fouling, i.e. biofouling[11–14].

Exploration of new electrode materials is one avenue towards addressing these challenges and contributing to the next generation of implantable electrochemical tools[15–17]. The carbon-fiber microelectrode (CFME) is the present-day standard implantable electrode for neurochemical sensing with fast-scan cyclic voltammetry (FSCV), a popular technique offering adequate spatial and temporal resolution to study sub-second neurotransmitter release in biological environments. In general, FSCV facilitates redox reactions of analytes by applying a fast-repeating voltage-driven waveform at the microelectrode to measure the resulting change in current. The CFME offers

advantageous $sp^2$ carbon structure to favor adsorption-controlled processes at the electrode surface maintains the sensitivity to detect neurotransmitters with FSCV. Despite 30 years of use and development, the CFME still faces major drawbacks that limit it as an ideal implantable neurochemical sensor for clinical application. First, the high adsorptive CFME surface in biological conditions is prone to biofouling and degradation resulting in signal sensitivity loss over time. Second, the CFME is conventionally hand fabricated using low-cost assembly methods which produce electrodes that are susceptible to human error, inconsistent in size and limited in shape and structure. As researchers move towards arrays and away from singular fiber fabrication, there has been great development with individual CFMEs being placed on an array and insulated with parylene-c[18,19]. However, these arrays are still hand fabricated. Other FSCV electrode array developments have focused on pyrolyzed photoresist films on a silicon wafer[20] creating a 4-channel recording probe, glassy carbon microelectrode arrays on a flexible polymer substrate[21,22] creating multichannel (8+) recording sites. Higher flexibility arrays have been developed using carbon fiber electrode threads[23] as well as a NeuroString, with a graphene based biosensing neural interface[24]. More recently, the development of a fuzzy graphene microelectrode array has also been reported[25].

To contribute to the advancements of microelectrodes offering array-style platforms, our team has previously reported on a promising all-diamond boron-doped diamond microelectrode (BDDME) for electrochemical measurements[12,15,26,27]. The boron-doped diamond (BDD) electrode, offering $sp^3$ carbon structure, has gained attention as a favorable biosensor due to its low background current, chemical inertness, mechanical stability, large working potential window and biocompatibility[15,28,29]. Others have shown that hybridizing BDD to CFME's reduces chemical fouling, and increases CFME lifetime[30,31]. Polycrystalline BDD films on sharpened tungsten rods

have shown reduced fouling and increased mechanical strength compared to CFME with FSCV measurements. However, BDD electrodes grown on metals such as tungsten or platinum still require hand fabrication and packaging in an insulating medium, and are not easily amenable towards batch electrode array fabrication. Finally, BDD has been microfabricated previously into planar multiarray and utilized for amperometric detection of neurotransmitters[32] and action potential firing[33,34] and the heterogeneous distribution of microdomains with chromaffin cells[35] leveraging the wafer microfabrication capabilities of the material.

Our team's all-diamond BDDME is freestanding and contains no additional metals to potentially address the outlined challenges faced by the standard CFME and typical metal-based BDD electrodes. These BDDMEs were constructed using batch wafer technology which is amenable to reproducibility, as opposed to hand fabrication techniques, where all the sensors are processed identically at a time. Batch fabrication offers ease of scalability, and the precision of semiconductor microfabrication. A key example is on a 4 in diameter Si wafer, where we can structure ~472 single channel diamond microelectrodes simultaneously. With precision alignment, the electrode yields from the different process steps can be greater than 70%. As this process matures, we expect to increase yield up to 90% of produced electrodes. Our all-diamond electrodes rely on microfabrication from the semiconductor industry, mature cleanrooms and tool process allow for ease of scale running multiple wafers through process steps in parallel, allowing for batch mass production.

The $sp^3$ to $sp^2$ ratio of the all-diamond BDD is tunable during the diamond growth process. The inherent $sp^3$ carbon structure of diamond provides a less adsorptive electrode surface, which is advantageous for tackling biofouling, albeit at the expense of sensitivity. Batch wafer fabrication of electrodes produces consistent and closely replicated electrodes that could potentially be used

in a microelectrode array. From a commercialization standpoint, modern wafer technology allows for easy scale-up and batch fabrication of electrodes which surpasses conventional hand fabrication techniques producing one sensor at a time. Our recent study on the *in vitro* biofouling performance[12] of these BDDMEs suggested that: 1) possible roles of both diffusion- as well as adsorption-controlled processes facilitating neurotransmitter sensing at the BDDME with FSCV, and 2) reduced biofouling-induced current attenuation at BDDME with a waveform selective for a serotonin redox reaction. A deeper investigation of the electrochemical behavior of BDDME was warranted to further explore the findings in this previous work.

In this report, we provide detailed findings on: (1) the fabrication scheme and changes implemented to improve the electrochemical performance of the BDDME, (2) slow scan cyclic voltammetric responses at the BDDME of reference analytes, such as Ruthenium Hexamine and Ferrocene Carboxylic Acid, and target analytes, such as dopamine (DA) and serotonin (5-HT), (3) fast scan cyclic voltammetric responses to common neurotransmitters (DA, 5-HT, 3,4-Dihydroxyphenylacetic acid (DOPAC), Ascorbic Acid (AA) and, hydrogen peroxide ($H_2O_2$) using a custom flow cell injection system and, (4) *In vitro* FSCV responses to mixture solutions containing varying concentrations of DA and 5-HT for oxidative peak identification. The limit of detection of DA was 260 nM and 160 nM for 5-HT, calculated using the linear dynamic ranges of each. Overall, the BDDME demonstrated favorability to detect 5-HT over DA, with the 5-HT oxidative peak current response being around two times greater than that of DA for the same concentrations. This report provides new findings to extend upon our work to develop the next-generation BDDME as a chronic, *in vivo* neurochemical sensor. The findings of this study add to the growing body of literature for next-generation electrochemical sensors and implantable neural devices.

## 2.2 METHODS AND MATERIALS

### 2.2.1 CHEMICALS

Dopamine (DA), serotonin (5-HT), ascorbic acid (AA), 3,4-Dihydroxyphenylacetic acid (DOPAC), hydrogen peroxide and Agarose (TBE blend 1.0%) were all purchased from Sigma-Aldrich, Inc (St. Louis, MO, USA). A 1 μM stock solution of each was prepared in 1 mM perchloric acid ($HClO_4$), and final working solutions were prepared diluting the stock solution in pH 7.4 Tris artificial cerebral-spinal fluid (aCSF) buffer immediately before measurement. Calibration ranges were from 200 nM – 200 μM. Tris aCSF was prepared by making a solution of 25 mM Tris, 126 mM NaCl, 2.5 mM KCl, 1.2 mM $NaH_2PO_4$, 2.4 mM $CaCl_2$, 1.2 mM $MgCl_2$ and adjusting the solution to pH 7.4[36]. Solution working time for the stocks was kept to no greater than 30 min to prevent measurable differences through degradation. Agarose gel was prepared at a concentration of 0.6% in deionized water.

### 2.2.2 INSTRUMENTATION AND DATA ACQUISITION

FSCV experiments were conducted using a two-electrode setup vs a Ag/AgCl quasi reference electrode. Electrodes were connected to a mini-UEI potentiostat with a variable gain headstage. (UNC Electronics Facility, University of North Carolina, Chapel Hill, NC). Data was collected using an NI-6363 data acquisition card, using HDCV Analysis software (Department of Chemistry, University of North Carolina, Chapel Hill, NC)[37]. Unless otherwise specified, a standard triangular FSCV waveform was used, by applying a -0.4 V holding potential, and ramping to a switching potential of 1.3 V at 400 V/s, repeating at 10 Hz to the electrode. Electrodes were tested and calibrated using a flow cell injection system with a TTL controlled switching source and a flowrate of 0.75 mL/min supplied by a NE-1000 syringe pump (New Era Pump Systems,

Inc. Farmingdale, NY). For FSCV calibrations, recordings were taken for 30 s, and boluses of sample was injected at 5 s, and removed at 15 s, providing a 10 s window of measured analyte exposure on the electrode. Peak oxidations and reduction responses for the various analytes were taken at time 13 s of the measurement when the response was stable. Reference electrodes used in FSCV experiments were fabricated using quasi-Ag/AgCl wires. Quasi-Ag/AgCl electrode were fabricated by soaking a silver wire (0.25 mm, Alfa Aesar) in undiluted concentrated bleach overnight (Clorox Professional Products Company, Oakland, CA). Slow-scan voltammetric (< 1 V/s) and electrical impedance spectroscopy measurements were made using a CHI 660C (CH Instruments, Austin TX) potentiostat with a Pt counter electrode and a Ag/AgCl reference electrode.

### 2.2.3 STATISTICAL METHODS

Data was analyzed and plotted using Origin (Pro), 2019. OriginLab Corporation, Northampton, MA, USA and Graphpad Prism version 10.3.0 for Windows, GraphPad Software, Boston Massachusetts, USA. Means and standard errors are tabulated and reported. Similar to our previous report, limit of detections (LOD) were calculated from the linear best fit equation with the corresponding sensitivity for the linear dynamic range of each analyte[38].

### 2.2.4 BORON-DOPED DIAMOND MICROELECTRODE (BDDME) FABRICATION

The BDDME was designed to have an 8 mm long shank, with both a 30 or a 50 μm wide tip, with a larger connection pad for handling and electrical connection. The conductive diamond was designed to be grown 4 μm thick and insulated with a 10μm layer with a a grow around method. Using a multi-step fabrication process (**Figure 2.1A**) modified from our previous work, we further developed and optimized these electrodes[15,27]. Previously, the diamond wafers were

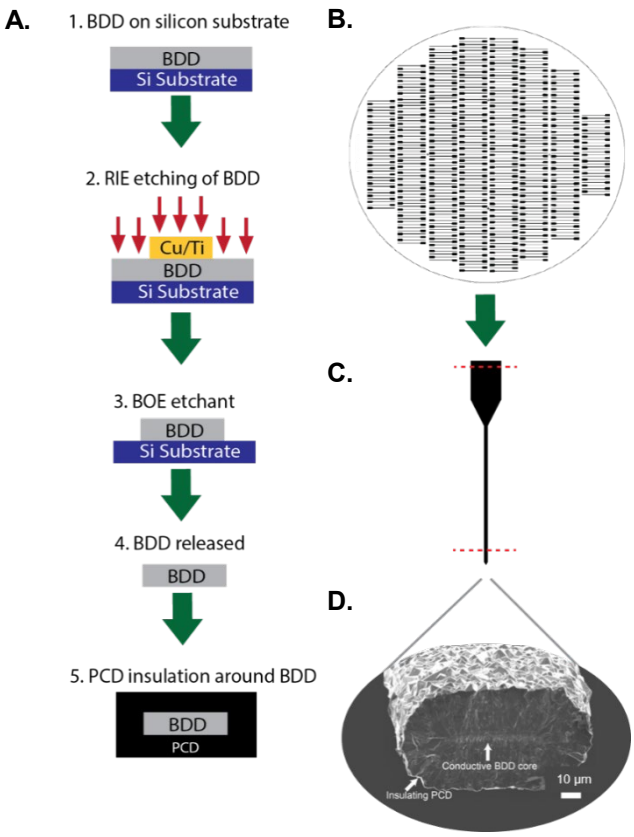


**Figure 2.1.** Fabrication of all diamond electrodes, where a conductive diamond core was insulated with an intrinsic insulating polycrystalline shell. **A.** Fabrication scheme of all diamond electrode where: (1) Boron doped diamond (BDD) is grown on a silicon wafer. (2 & 3) Using lithography and a metal hard mask, the diamond is plasma dry etched and patterned to form the shape of the electrode. (4) The silicon wafer was dissolved releasing the conductive core, and (5) insulated by growing intrinsic polycrystalline diamond (PCD). **B.** Representative example of the scalability and flexibility of designing 100's of electrodes simultaneously. **C.** Electrical connection is formed by cleaving the tip and connection pad. Dotted lines represent cleaving points to expose BDD conductive core. **D.** Scanning electron micrograph of the cleaved diamond tip, revealing the insulating polycrystalline diamond encasing the conductive boron doped diamond core.

fabricated in a 2.45 GHz microwave reactor, grown on 3" silicon substrates[27]. In an effort to move towards scalability, 4" Ø 500 µm thick single side polished silicon wafers were utilized with larger diamond reactors. Initially, wafers were scratch seeded and microcrystalline BDD films were grown on a 4" silicon wafer using a 915 MHz microwave plasma-assisted chemical vapor deposition reactor. Standard BDD synthesis conditions included a microwave power of 9 kW, 900

ºC stage temperature, a chamber pressure of 60 Torr and a gas chemistry of 2 % methane. Diborane was added to the diamond grown at a B/C ratio of 37,500 ppm to ensure conductivity. Following BDD growth, copper and titanium were electron beam evaporated (Kurt Lesker Axiss PVD System) and patterned via photolithography (ABM-USA, INC., Jan Jose, CA, USA), (**Figure 2.1B**) followed by a wet chemical etch. The patterned BDD films with the copper mask were then etched using a microwave assisted reactive ion etcher (RIE) SF6/Ar/O2 with a microwave power of 1000 W and a radio-frequency (RF) bias of 150 W (180 V). The copper mask was then removed using nitric acid. The Si was removed using an HNA etchant, at a ratio of 6:11:5 acetic acid: nitric acid: hydrofluoric acid. Prior to Si etching, batches of electrodes were laser cut out of the main wafer to decrease etchant time, and allow for ease of handleability. The now released electrodes were then placed on a silicon holder vertically, where an insulting PCD film was grown around the freestanding BDD cores, using a hot filament chemical vapor deposition (HF-CVD) around the BDD fibers, insulating the conductive diamond.

Following fabrication, the ends of the electrodes were physically cleaved to expose the BDD core, revealing the pristine diamond (**Figure 2.1C**). Electrical connection through the diamond substrate was made by manually cleaving the opposite end, connection pads. The BDDME's were secured in place and electrically connected to a breakout board using an aqueous-based graphite conductive adhesive (Alfa Aesar, Ward Hill, MA). Following fabrication, a scanning electron micrograph of the BDDMEs revealed a BDD core to have a geometric surface area of either 105 µm2 or 175 µm2 (based on a 30 or 50 µm wide pattern, and 4 µm thick BDD growth thickness), and an insulating polycrystalline diamond (PCD) shell of 11 µm to 20 µm thickness based on the distance tip was cleaved along the shank (**Figure 2.1D**). Thicknesses varied as the growth rate increases with distance from the filaments used during the diamond growth.

## 2.3 RESULTS AND DISCUSSION

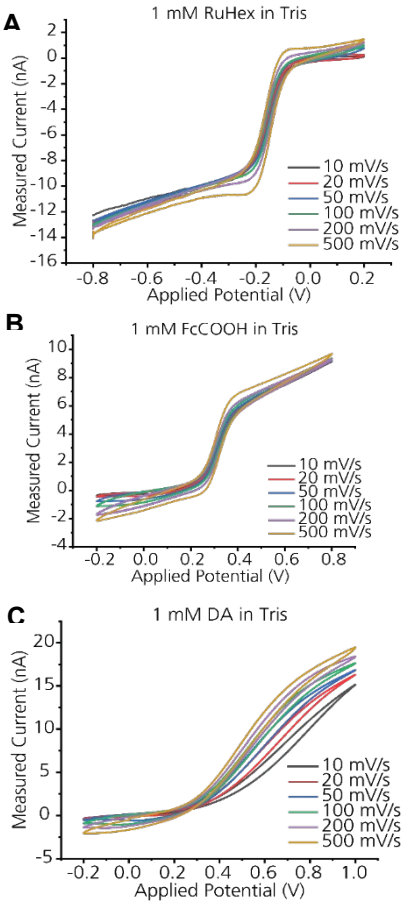


**Figure 2.2.** Slow scan cyclic voltammetry at the BDDME to determine electron transfer kinetics. **A.** Representative measurements of Ruhex on a BDDME, with the calculated rate constant for this electrode. **B.** Representative measurements of FcCOOH on a BDDME, with the calculated rate constant for this electrode. **C.** Representative measurements of DA on a BDDME, with the calculated rate constant for this electrode. All measurements were made in pH 7.4 Tris buffer. Applied potential was versus reference electrode.

Following fabrication, we utilized cyclic voltammetry to characterize the electrochemical response of the BDDME to ruthenium hexamine (RuHex) (**Figure 2.2A**), ferrocene carboxylic acid (FcCOOH) (**Figure 2.2B**), and dopamine (DA) (**Figure 2.2C**), in Tris aCSF pH 7.4 from 10 to 500 mV/s. We additionally measured DA in $H_2SO_4$ (**Figure S2.1A**). Utilizing the Randle-Ševčík equation we calculated the electroactive area for each electrode, and generated a Tafel plot to

**Table 2.1.** Heterogeneous rate constants for FeCOOH, RuHex and DA measured in Tris aCSF (pH 7.4) with different BDDMEs determined from Tafel Plots. (mean ± SEM, n=4 electrodes). All analyte concentrations were 1 mM.

| Species | Average $k_o$ (x$10^{-2}$ cm/s) |
|---|---|
| FcCOOH | 3.09±0.72 |
| RuHex | 5.37±1.66 |
| DA | 4.26±1.09 |

calculate the heterogeneous rate constant for these materials[39,40](**Table 2.1**). Interestingly, the average calculated heterogeneous rate constant for FcCOOH with the BDDME is comparable to values previously reported by Jarošová et al. for BDD based microelectrode measurements[41]. It should be noted that Jarošová et al. electrodes were fabricated through growing BDD on Pt, and as such would have a lower resistance as compared to the BDD films, where diamond is used as the electrical contact. We observed a slight difference for RuHex, where the rate constant was slightly slower on our BDD. Notably, our CV current responses indicate a slightly resistive electrode or surface, with electrical impedance of 2.1 MΩ at 1 kHz when measured in Tris aCSF (**Figure S2.1B**). When comparing 1 mM 5-HT in Tris (**Figure S2.1C**), the scan rate at 100 mV/s revealed that oxidation was extremely slow, and it was not possible to calculate the electroactive area. As such $k_o$ was not calculated. This could indicate an electrode-solution interface resistance, as when, using a 4-point probe after the conductive diamond growth, we measured the BDD and average resistivity to be 4.6 mΩ*cm ±1.4 mΩ*cm. All electrochemical measurements were performed on a cleaved diamond surfaces without any electrochemical pre-activation steps.

Following slow scan measurements, the BDDME was characterized in a custom flow cell injection system. The electrodes were pre-cycled utilizing the DA waveform applied at 10 Hz for 120 mins to study the background and electrode stability (**Figure S2.2**). The FSCV background current is generated by the rearrangement of ions around the electrode or charging of the electric

double layer[42]. A high scan rate (400 V/s) captures the faradaic current produced by the redox reaction of electroactive species at the electrode[43,44], but a large capacitive background current is also generated and needs to be subtracted out to identify[43,45]. Similarly, our all-diamond BDDME demonstrated quick stabilization (within 15 minutes) and minimal drift over 120 min of continuous cycling of the electrode (**Figure S2.2A**). The background peak current on average was ~22 nA for a 30 μm wide electrode and ~28 nA for a 50 μm wide electrode (**Figure S2.2C**). The shape maintained a low capacitive response. At the turn around potential, there was a slight peak increase. This is attributed to possible $sp^2$ etching that occurs at the grain boundaries. We observed that during the initial cycle, the peak slightly decreased, however over the course of the 2-hr experiment, had minimal change. Interestingly on the back scan, there are non-capacitive changes, indicating slight electrochemical modifications to the diamond surface, which warrant further studies.

Previous publications have often focused on thin film, planar BDD electrodes, but limited studies have explored diamond as a microelectrode[29,46]. Park et al. (2005) reported on the background cyclic voltammetric response of thin film BDD on sharpened Pt wire in comparison with the carbon fiber microelectrode (CFME), and showed a low and stable background current independent of solution pH of the diamond microelectrode[47]. These BDD-Pt wire electrodes had a surface area of $1.8 \times 10^4$ $\mu m^2$ and were hydrogen terminated prior to electrochemical measurements to ensure pH insensitivity. However, hydrogen-termination of the electrode removes the surface-oxygen functionalities[48] that are essential for adsorption controlled electrochemical measurements specifically for DA, using FSCV[49,50]. Our freestanding BDDME is unique in its micromachined fabrication process, smaller size (100 to 200 $\mu m^2$), and bare, un-treated surface favorable for FSCV measurements. At the same time, lack of hydrogen-termination

of the our BDDME may leave some redox-active carbon-oxygen functionalities on the electrode surface, making the electrode sensitive to pH changes (**Figure S2.3**). It is also important to note that while our BDDME maintains a bulk $sp^3$ carbon microstructure, some $sp^2$ carbon may exist at the grain boundaries due to boron doping content. As shown in **Figure S2.2A**, the BDDME background was relatively stable over two hours with a slight shift that presents as a drift, possibly indicative of surface etching of the minor $sp^2$ carbon present on the electrode surface. The BDDME showed excellent response stability and repeatability over this time with an average current response of $0.293 \pm 0.007$ nA for 5 μM DA injections (**Figure S2.2B**). The stability of the electrode over the course of two hours, and the stability of measuring ferrocene carboxylic acid (**Figure S2.2D**), demonstrates that the BDDME, without the metal support, maintains physical qualities that allow good chemical and electrical properties for an electrochemical sensor.

Fast stabilization of the all-diamond BDDME can be especially advantageous for *in vivo* measurements where stabilizing an electrode immediately upon implantation can take long periods of time (up to 1 hour) before a single recording. When cycled in a conductive aqueous solution with an applied potential over 1.0 V, a carbon electrode surface can undergo chemical and physical changes that manifest as background drifts[45,51]. It has been reported that the BDD electrode lacks the majority of $sp^2$ [29], and thus, the background reaches equilibrium relatively quickly with minimal shifts. Our BDDME similarly contains low levels of $sp^2$ carbon content, mainly concentrated at the grain boundaries, allowing the electrode to reach fast equilibrium for adsorption-controlled electrochemical measurements. The Raman spectra (**Figure S2.4**) showcases a strong boron doping peak at 491 $cm^{-1}$, a diamond peak at 1210 $cm^{-1}$, a disorder band at 1325 $cm^{-1}$, and a small graphitic (G) band at 1540 $cm$[52].

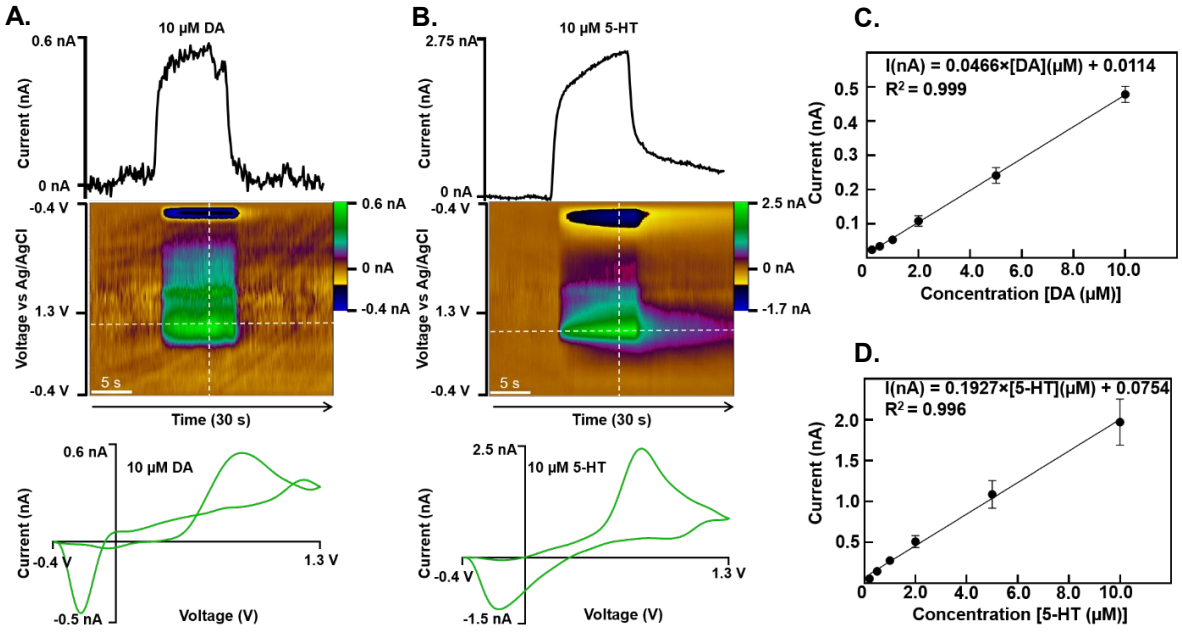


**Figure 2.3.** Comparison of the response for DA and 5-HT for the BDDME. The triangular waveform from -0.4 V to 1.3 V and back at 400 V/s was applied at 10 Hz frequency for all measurements. **A.** Representative FSCV current vs time trace, voltage vs time color plot, and current vs voltage cyclic voltammogram for 10 µM DA at the BDDME. **B**. Representative FSCV current vs time trace, voltage vs time color plot, and current vs voltage cyclic voltammogram for 10 µM 5-HT at the BDDME. **C**. Calibration curve of DA at the BDDME ($n$=3). **D**. Calibration curve of 5-HT at the BDDME ($n$=3). Buffer solution of tris aCSF (pH 7.4) was pumped at a rate of 750 µLmin$^{-1}$. Dotted lines on color plots indicate the extracted current vs. time traces and current vs voltage plots. Scale bars on the bottom left corner of color plots indicate flowing period.

To characterize the response of these diamond sensors and determine the diamonds sensitivity towards common neurotransmitters, we initially characterized the response of DA and 5-HT, AA, DOPAC, and $H_2O_2$ on the BDDME. (**Figure 2.3** and **Figure S2.5**). Interestingly, all tested analytes maintained a linear response with concentration and were well resolved on the BDDME with a sharp on and off current response ensuring high fidelity of temporal resolution and minimized electrode chemical fouling. A wide sensitivity difference between DA and 5-HT for the same concentration of each analyte (representative 10 µM response of DA and 5-HT shown in **Figure 2.3A&B** respectively) was observed. The electrode showed a linear current response to

**Table 2.2.** Comparison for LOD and sensitivity for dopamine and serotonin using the BDDME (n=3) with an electroactive area of ~100 to 200 $\mu m^2$.

| Analyte | LOD (μM) * | Slope (nAμM-1) | Measured Range (μM) | r2 |
|---|---|---|---|---|
| Dopamine (DA) | 0.26 | 0.046 | 0.2 – 10.0 | 0.999 |
| Serotonin (5-HT) | 0.16 | 0.192 | 0.2 – 10.0 | 0.996 |

*Limit of detection (LOD) was calculated for the linear dynamic ranges of 0.2–10 μM for DA and 0.2–2.0 μM for 5-HT. See methods section for LOD calculation.

increasing concentrations of DA (**Figure 2.3C**) over the measured range of 0.2 to 10 μM with a limit of detection (LOD) of 0.26 μM found from the linear dynamic range of 0.2 to 10 μM. Similarly, a linear current response to increasing concentrations of 5-HT (**Figure 2.3D**) was observed over the same range of 0.2 to 10 μM, but with a lower limit of detection (LOD) of 0.16 μM calculated from the linear dynamic range of 0.2 to 2.0 μM (summary of statistics is reported in **Table 2.2**).

Both neurotransmitters generate cyclic voltammograms (CVs) with oxidation and reduction peaks (**Figure 2.3 A&B**), but 5-HT has a larger and clearer response than DA. Notably, the oxidation and reduction peaks are prominently not symmetrical for DA, and a smaller third peak is evident near the turnaround potential of 1.3 V. The small peak at 1.3 V is theorized to be background subtraction error due to slight changes in the background. The representative CV for DA on the BDDME (Current Voltage plot, **Figure 2.3A**) is similar to a more traditional and symmetric "duck-shaped" CV with equivalent oxidation and reduction magnitudes that would be expected with slow scan voltammetry where there is less mass transport of the analyte to the electrode surface due to the growing diffusion layer[43]. The shape indicates that diffusion-controlled

kinetics are at play, and the current is unable to drop to zero before the potential is reversed to induce reduction of the analyte[43]. Additionally, the CV has an oxidation peak ~0.7 nA, with a reduction peak close to -0.5 nA. Ideally, if adsorption-controlled kinetics were solely governing the DA redox reaction, the FSCV voltammogram would generate a reduction peak size that is approximately half the area of the oxidation peak due to strong adsorption of DA and quick desorption of dopamine-*o*-quinone, oxidized form of DA, at the surface[43,50]. Here, the peak heights are nearly the same indicating that possibly adsorption properties of the BDDME, although containing some $sp^2$ carbon content, and surface oxygen containing groups, do not allow complete and strong adsorption of DA with fast desorption of dopamine-*o*-quinone[53–55]. On the other hand, the CV for 5-HT (Current Voltage Plot, **Figure 2.3B**) presents a cleaner response with an oxidation peak of 2.5 nA and reduction peak of -1.5 nA. Still, even in the 5-HT response, the current does not drop to zero before the potential is reversed and a less prominent yet visible second peak is present near the turn around. Based on the calibration curves and compared statistics (**Table 2.2**), the BDDME is favorable to detect lower limits of 5-HT than DA over the measured range of concentrations based on the diamond surface adsorption property characteristics for these catecholamines. Overall, this means that the BDDME is able to carry out adsorption-controlled redox reactions for the most part, but diffusion-controlled kinetics interfere possibly due to the $sp^3$ carbon content at the surface.

We further characterized these electrodes against DOPAC, and AA (**Figure S2.5A&B**) using the standard triangular waveform, which both maintained a linear response with concentration. Interestingly, for DOPAC, the oxidation response was only resolved for the applied current range, and occurred predominantly at +1.1 V. No reduction peak was observed, indicating that a lower applied holding period is necessary to resolve the response. For AA, the oxidation

peak was clearly resolved. All samples for the calibration curve were pH adjusted, to account for decreases in pH due to AA concentration. Comparing DA to DOPAC, a 10 μm DA maintains a similar response to 100 μm. DOPAC with the same current magnitude response. Similarly, for AA, 50 μm of AA correlates with 10 μM DA maintaining sensitivity favorability towards 10 μM DA. Interestingly for $H_2O_2$ there is a much better sensitivity on the BDDME, where 1 nA of response is equivalent to 2 μM (**Figure S2.5C**). It should be noted that the $H_2O_2$ measurements were made with an increased potential of 1.5 V for the turnaround to resolve the oxidation. Key metrics and responses for the analytes are reported in **Table S2.1**.

Comparing the all-diamond cleaved BDDME towards others which we have previously developed and reported on, it should be important to note that these BDDME electrodes with a cleaved tip show lowered sensitivity towards DA. Our previously reported all-diamond electrodes were prepared using an ND:YAG 1064 nm IR laser to cleave and create the recording site[15]. No long-term studies were done in this report to understand the impact of laser dicing and electrode stability. More recently, our findings using a different laser slicing system with an 800 nm femto cutting laser show-cased the temporary increase in DA and 5-HT sensitivity, however these electrodes lacked long term electrochemical stability due to rapid $sp^2$ rapid etching induced by the laser slicing[38]. Additionally, it was found in both studies that laser slicing damaged the PCD layer, increasing the effective surface area of the electrode by an unknown, and minimally controlled amount. All pieces of work point towards the need for diamond surface modification to increase the sensitivity for DA and 5-HT without causing long-term changes, which may lead towards chemical etching of the electrode itself.

While the BDDME may present a surface with weaker adsorption than the standard bulk $sp^2$ carbon fiber electrodes, advantages to a less adsorptive surface include: (1) resilience towards

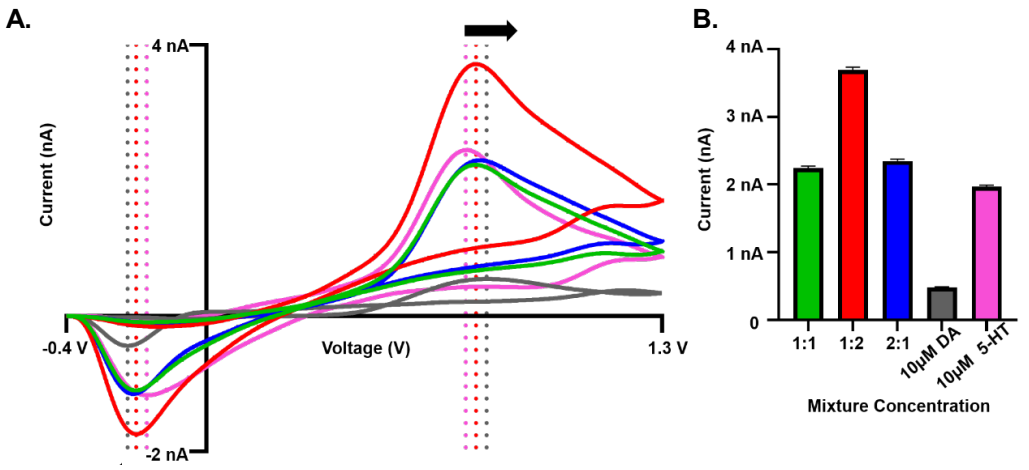


**Figure 2.4.** FSCV responses of mixed solutions containing DA and 5-HT on BDDMEs (*n*=3). **A**. Overlapping FSCV voltammograms of mixtures with varying concentrations of DA and 5-HT. Triangular waveform was employed, starting at -0.4 V to 1.3 V and back scanning at 400 V/s at 10 Hz frequency. Voltammograms of only 10 µm 5-HT and 10 µm DA plotted for reference. **B**. Corresponding current vs concentration plot comparing peak oxidative current for each solution. Mixtures (from left to right on x axis) contain 10 µm DA & 10 µm 5-HT (green), 10 µm DA & 20 µm 5-HT (red), 20 µm DA & 10 µm 5-HT (blue), only 10 µm DA (grey), and only 10 µm 5-HT (magenta).

chemical and physical surface changes in an analyte rich environment such as the brain, and (2) distinguishable neurotransmitter peaks due to adsorption favorability of one analyte over the other. Poor chronic stability and biofouling, i.e. adsorption of interferent proteins upon implantation in a biological environment, are long-standing challenges that disrupt neurochemical detection in the brain. We have previously reported that the BDDME experienced significantly lower biofouling-induced current reductions for 5-HT when using the selective "Jackson" waveform in comparison with the highly adsorptive CFME[12]. This indicates that the BDDME could potentially serve as a more resilient electrode in a chronic *in vivo* setting. Another prevalent FSCV *in vivo* challenge is accurate identification of neurotransmitter peaks – analytes that oxidize and reduce in the same potential window may overlap or appear together, complicating selective detection of the neurotransmitter of interest. Based on our observations from **Figure 2.3**, we exposed the BDDME to boluses of 10 µM 5-HT and 10 µM DA, individually followed by mixtures using the flow

injection system to test peak distinguishability. We made mixtures with 1:1 (10 : 10 μM) DA to 5-HT, 1:2 (10 : 20 μM) DA to 5-HT, and 2:1 DA to 5-HT (20 : 10 μM) to study the FSCV voltammograms and peak shifts (**Figure 2.4**). As expected, a higher concentration of 5-HT in the mixture overwhelmed the response, and reduced the oxidation and reduction peaks' separation. A higher concentration of DA in the mixture pulled the peaks further apart, indicating slower electron transfer when DA is present in the mixture.

The results in **Figure 2.4** show that the BDDME favors detection of 5-HT over DA even while using the standard triangular waveform employed for DA detection. There is a slight shift in oxidation response from 0.7 to 0.73 V when 5-HT is present as compared to the DA oxidation. There is an interesting additional change in the oxidation shape with DA present, where at 1.1 V, there is a broadening of the response. Additionally, there is a slight shift in the reduction potential as well from -0.35 to -0.3 V when 5-HT is present compared to DA. As there are no intrinsic differences in the oxidation measurements additional statistical methods such as PCA would need to be used to differentiate the two-chemical species. As both 5-HT and DA oxidize and reduce within the potential window of -0.4 V to 1.3 V, other manipulations to the waveform may need to be employed *in vivo* to selectively detect one neurotransmitter over the other. As previously reported, employing the Jackson waveform with a faster scan rate may increase the BDDME selectivity and eliminate the slower DA electron transfer, leaving a more prominent 5-HT signal. On the other hand, slowing the scan rate down may present a cleaner DA signal to match the sluggish electron transfer which is planned for future evaluations.

To verify intact physical implantation of the BDDME for *in vivo* application, we inserted the BDDME fiber in a low concentration (0.6%) agarose gel model, to mimic the mechanical properties of brain tissue[56], and validated successful, undamaged implantation and explanation of

the electrode (**S2.6**). To test the diamond response *in vivo* we fabricated a slightly modified version of the BDDME to increase the surface area of the electrode. Briefly, we restructured the diamond to form BDD strips using RIE (**S2.7A&B**) to design 10 or 20μm wide, 4 μm thick and 1-inch long fibers. We then placed these inside glass capillaries, and sealed the tips using epoxy resin (**S2.7B**). The electrodes were cut to be ~100 μm long from the epoxy seal to mimic the size of a CFME. These were tested *in vitro* using FSCV flow injection to calibrate the response to DA ranging from 50 to 1000 nM (**S2.7D**). Next, for *in vivo* application, the electrode was PEDOT:Nafion coated[57] and implanted in the rat nucleus accumbens core, and the medial forebrain bundle was electrically stimulated for DA release. *In vivo* data collection was done following previously published reports[58,59] (see Supplemental Methods). The measured *in vivo* stimulated DA response ($n$=1 rat) was ~150 nM on this glass BDDME. This verified the *in vivo* potential of an all-diamond BDDME electrode with a larger surface area, and a device that may be compatible with *in vivo* FSCV for future studies.

Various modifications to the electrode could further enhance electrochemical measurements at the BDDME, especially for *in vivo* applications. The BDDME reported here has an approximate geometrical electroactive surface area of ~100 to 200 $\mu m^2$, about ten times smaller than the standard carbon fiber microelectrodes (~7 μm diameter, and 100 μm long for an area of 2238 $\mu m^2$). Because the size of the detected current is proportional to the electroactive area on the surface of the electrode, increasing the electroactive area of the freestanding BDDME could contribute to greatly increasing peak current measurements and lowering the limits of detection. Additionally, others using CFME have reported on the effect of edge planes for DA adsorption[50], and taking this into account, the diamond growth direction may impact chemical responses. Our measurements are made across the growth boundary, and previous research from our team has

indicated a DA sensitivity difference between the growth face and nucleation face of the BDD[26]. Alternatively, employing an array-style electrode could maximize detection sites and overall electroactive area. Laser cut BDDMEs, as reported in our recent study[38], could provide a more sensitive, $sp^2$ rich environment that may be beneficial for acute *in vivo* detection for neurotransmitter rich regions, however laser cite BDDME are short-lived as these etch due to the DA waveform switching potential of over 1.0 V. Pretreatment options with cation exchange polymers, such as Nafion, could also be advantageous for increased sensitivity of the electrode. These polymer films and membranes may increase adsorption limitations, as the diamond material would remain stable without etching from underneath the membrane, unlike the carbon fiber counterpart, but this remains to be studied.

## 2.4 CONCLUSION

These findings showcase a scale-able all-diamond probe and provide foundational information to guide future *in vivo* sensor development for electrochemical measurements using the freestanding BDDME. The results reported here are aimed at filling the knowledge gaps and background information to support our past and future work with the next generation of BDDME. The BDDME shows a favorability towards 5-HT detection with the oxidative peak responses having a 2-fold increase compared to DA for the same concentrations of analytes and a lower limit of detection of 0.16 μM for 5-HT than the 0.26 μM for DA. Similarly, the mixture comparisons elucidate that higher concentrations of 5-HT overwhelm the voltammogram, and DA demonstrates slower electron transfer in comparison to 5-HT at the BDDME surface. However, modifications to the waveform, and selective potential windows, may prove useful to differentiate between oxidative peak signals for the *in vivo* setting. Due to the surface characterization of the BDDME, a tradeoff in sensitivity may need to be accepted; however, this can be surmountable with increased

electroactive area sizes, array-style electrode and surface treatments, especially for *in vivo* application as verified in this study. These probes offer a biocompatible platform with stability in the measurement response for future consistent and chronic *in vivo* measurement of biomolecules.

## 2.5 SUPPLEMENTARY MATERIALS

### 2.5.1 ANIMAL, SURGERY AND IMPLANTATION

Surgical procedure and implantation were adapted from previously published methods58,59. A male, adult, Sprague Dawley rat was kept under isoflurane (2.5-3.5% in oxygen) anesthesia for the surgical procedure and in vivo data collection. Craniotomies were performed over nucleus accumbens (NAc) (+1.4 mm anterior posterior, +1.4 mm medio lateral from Bregma) and the medial forebrain bundle (MFB) (-2.5 mm anterior posterior, +1.7 medio lateral from Bregma). Meloxicam (2 mg/kg) was injected subcutaneously prior to electrode implantation as an additional measure to minimize risks of pain or discomfort. The BDDME was stereotaxically lowered in the NAc at a depth of 6.7 mm from the cortical surface, and the stimulating electrode was stereotaxically implanted in the MFB to the depth of 8.3 mm. A third craniotomy was performed on the contralateral hemisphere to access the cerebral cortex for placement of a Ag/AgCl reference electrode, inserted at a depth of 3mm. Dura was resected at each craniotomy prior to electrode implantation. Stereotaxic coordinates were taken from Parent et al59. Upon completion of in vivo data collection from the anesthetized rat, electrodes were explanted, and the rat was euthanized by an overdose delivery of sodium pentobarbital intraperitoneally. All surgical procedures described were approved by the Michigan State University Animal Care and Use Committee.

### 2.5.2 ELECTRODES AND INSTRUMENTATION FOR IN VIVO DATA COLLECTION

The BDDME was modified for in vivo data collection (**Figure S2.7**). A PEDOT:Nafion coating was applied at the BDDME using methods described by Vreeland et al57 prior to in vivo data collection. A bipolar stimulating electrode (P1 Technologies Inc, Roanoke, VA) was lowered in the MFB to deliver a 60-pulse train of 1 ms per phase, 300-600 μA, biphasic, square wave pulses at a frequency of 60 Hz via a Stimulus Generator (STG4002-1.6 mA, Multi Channel Systems, Reutlingen, Germany). The stimulation parameters were taken from Parent et al59. An Ag/AgCl wire was used as the reference electrode for in vivo FSCV measurements. All electrodes were connected to a mini-UEI potentiostat with a variable gain headstage (UNC Electronics Facility, University of North Carolina, Chapel Hill, NC). Data was collected using an NI-6363 data acquisition card using the HDCV Analysis software (Department of Chemistry, University of North Carolina, Chapel Hill, NC). The Stimulus Generator was TTL controlled using HDCV, and the biphasic stimulation pulse train was offset by 20 milliseconds to prevent interference with in vivo FSCV measurements.  Electrodes and Instrumentation for In Vivo Data Collection

The BDDME was modified for in vivo data collection (**Figure S2.7**). A PEDOT:Nafion coating was applied at the BDDME using methods described by Vreeland et al57 prior to in vivo data collection. A bipolar stimulating electrode (P1 Technologies Inc, Roanoke, VA) was lowered in the MFB to deliver a 60-pulse train of 1 ms per phase, 300-600 μA, biphasic, square wave pulses at a frequency of 60 Hz via a Stimulus Generator (STG4002-1.6 mA, Multi Channel Systems, Reutlingen, Germany). The stimulation parameters were taken from Parent et al59. An Ag/AgCl wire was used as the reference electrode for in vivo FSCV measurements. All electrodes were connected to a mini-UEI potentiostat with a variable gain headstage (UNC Electronics Facility, University of North Carolina, Chapel Hill, NC). Data was collected using an NI-6363 data

acquisition card using the HDCV Analysis software (Department of Chemistry, University of North Carolina, Chapel Hill, NC). The Stimulus Generator was TTL controlled using HDCV, and the biphasic stimulation pulse train was offset by 20 milliseconds to prevent interference with in vivo FSCV measurements.

### 2.5.3 SUPPLEMENTARY FIGURES

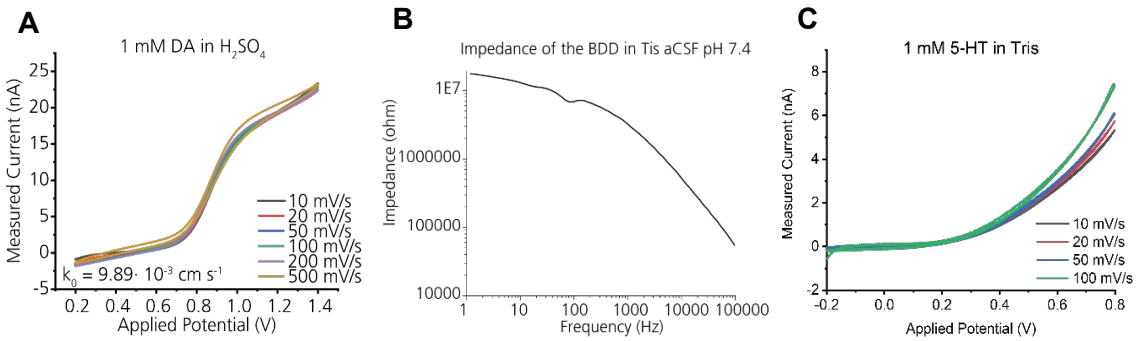


**Figure S2.1 A.** Voltammetric response of BDDME to DA in $H_2SO_4$. **B.** Representative impedance response of the BDDME in Tris aCSF. **C.** Representative 5-HT measurement in Tris aCSF solution.

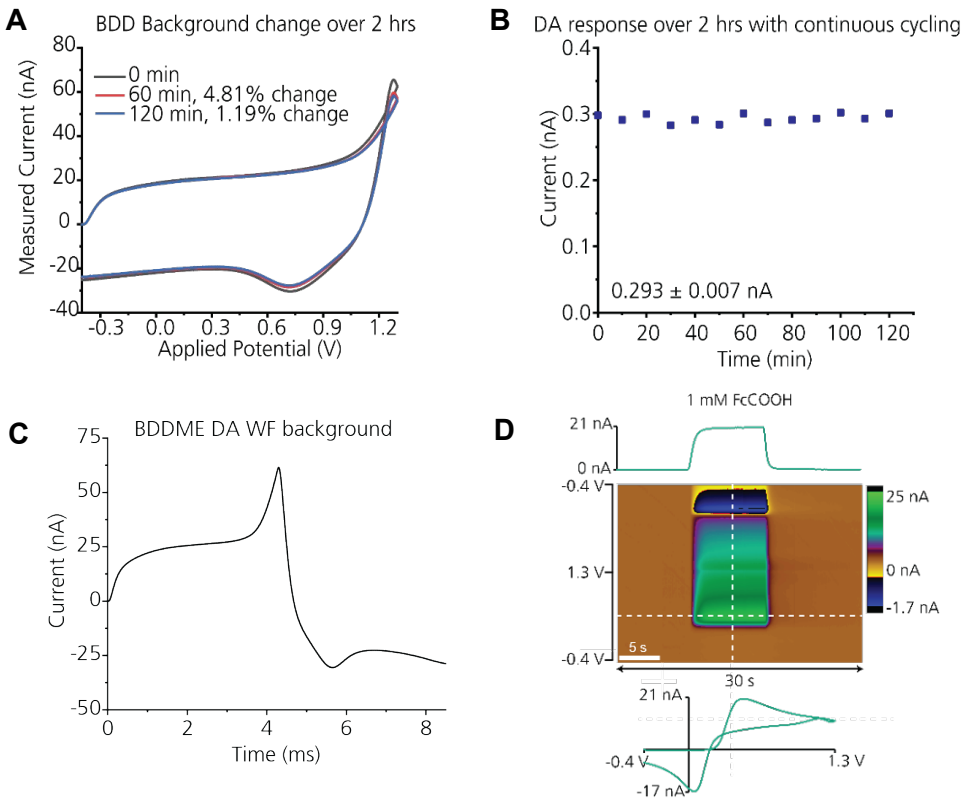


**Figure S2.2.** **A.** BDDME background response when applying the standard DA waveform at 10 Hz application frequency. **B.** Repeated injections of 5 µM DA delivered through the flow cell to the BDDME every 10 minutes showing a stable and reproducible response for the peak oxidative currents. **C**. Background of the BDDME with the triangular waveform commonly applied for dopamine detection starting at -0.4 V to 1.3 V and back at 400 V/s and at 10 Hz frequency. **D.** A representative response to measuring 1 mM FcCOOH in Tris pH 7.4, using a flow injection system on the BDDME. Dotted lines on color plot indicate the extracted current vs. time trace and current vs voltage plot. Scale bar on the bottom left corner of color plot indicates flowing period.

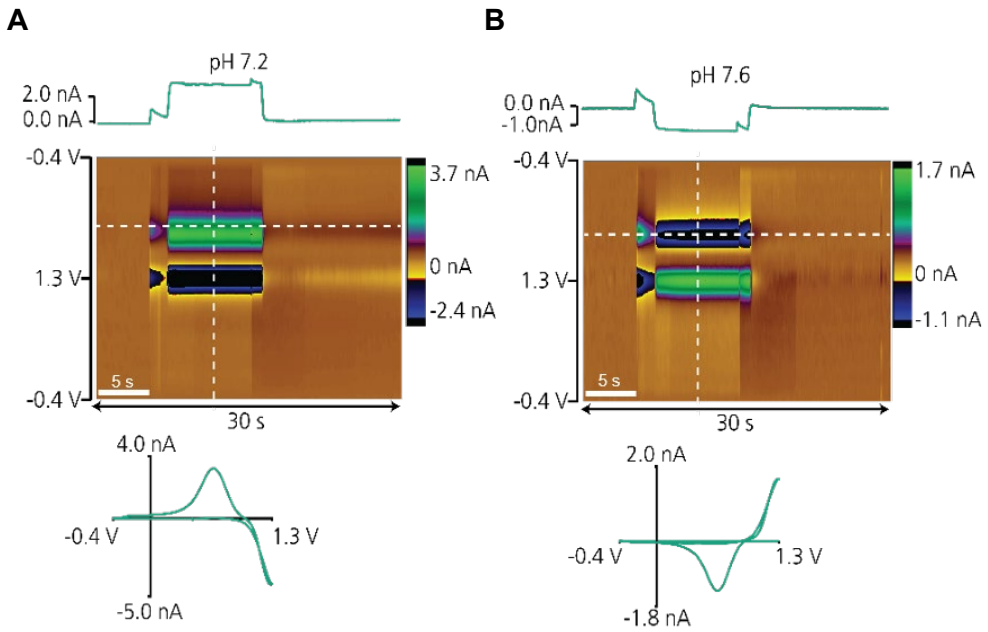


**Figure S2.3**. The BDDME was found to be highly responsive to pH changes, and the acidity of $HClO_4$ influenced the observed the current. Neurochemical stock solutions for in vitro experiments were in 1 mM $HClO_4$ as opposed to 0.1M $HClO_4$ that has been used previously reported in literature. High concentrations of $HClO_4$ overwhelmed the real DA current and presents on the backward scan. Dotted lines on color plots indicate the extracted current vs. time traces and current vs voltage plots. Scale bars on the bottom left corner of color plots indicate flowing period.

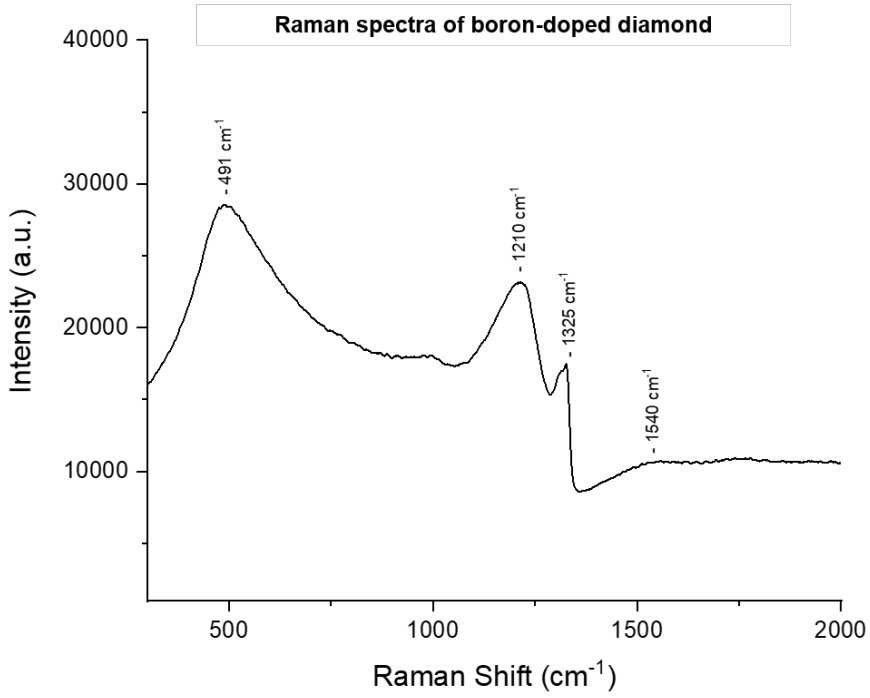


**Figure S2.4.** Representative Raman spectra of the conductive diamond used for the fabrication of the all diamond microelectrodes.

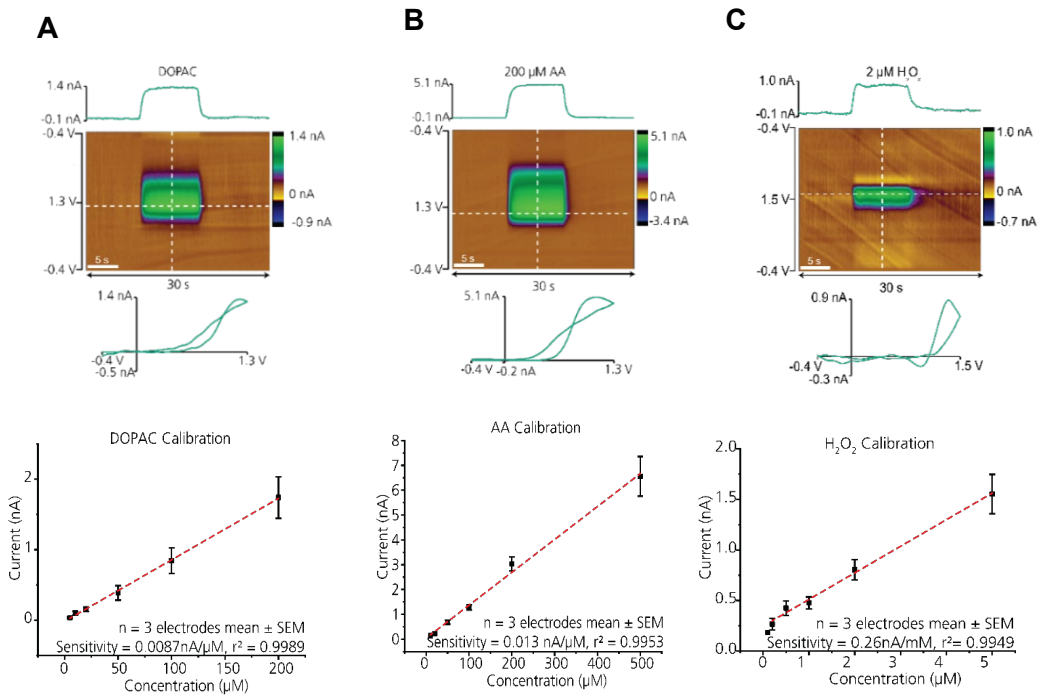


**Figure S2.5.** Commonly investigated NT responses at the BDDME. The triangular FSCV DA waveform from -0.4 V to 1.3 V to -0.4 V at a scan rate of 400 $Vs^{-1}$ with a frequency of 10 Hz was applied at the electrode for DOPAC and AA, and increased to 1.5 V for $H_2O_2$. A buffer solution of tris aCSF (pH 7.4) was pumped at a rate of 750 $\mu Lmin^{-1}$. Minimum of three buffer rinses were done prior to injecting analyte to flush the flow cell and prevent contamination. Dotted lines on color plots indicate the extracted current vs. time traces and current vs voltage plots. Scale bars on the bottom left corner of color plots indicate flowing period.

**Table S2.1** Figures of merit of common compounds at the BDDME (electroactive surface area ~ 100 to 200 $\mu m^2$) (mean ± SEM, n=3 electrodes).

| Compound | ΔEp (V) | Ox/Red ratio | Range of linearity (μM) | Slope ($nA \cdot \mu M^{-1}$) | $r^2$ | Limit of detection (μM) |
|---|---|---|---|---|---|---|
| Ascorbic Acid | 0.67±0.08 | - | 5-200 | 0.00872 | 0.9989 | 3.26 |
| DOPAC (extended WF, -0.7-1.3 V) | 1.53±0.16 | 1.53±1.6 | 10-500 | 0.0133 | 0.9953 | 2.60 |
| pH | - | - | 7.2-7.6 (pH) | -5.52 (nA/pH) | 0.9856 | - |
| $H_2O_2$ (extended WF -0.4-1.5 V) | 1.40±0.01 | - | 0.1-5 | 0.263 | 0.9911 | 0.200 |

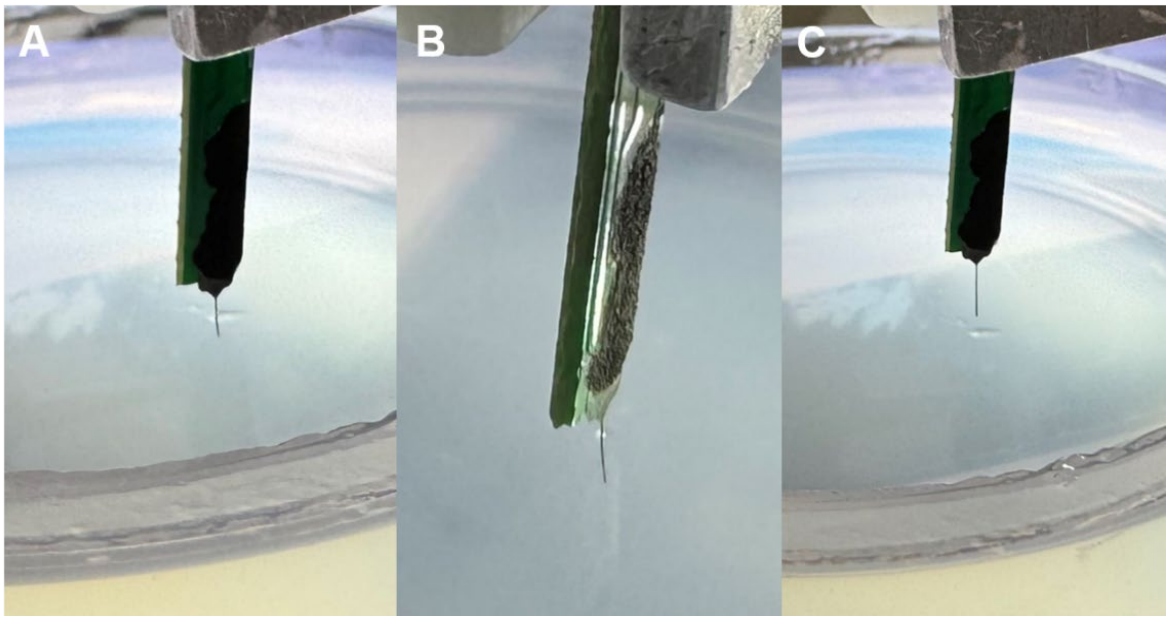


**Figure S2.6**. All-diamond BDDME inserted into a low concentration (0.6%) agarose gel model to mimic the mechanical properties of brain tissue and test implantation. **A.** Half length of BDDME fiber inserted in the agarose gel. **B.** Full length of BDDME fiber inserted in brain mimic, remaining in tact. **C.** BDDME fiber fully explanted from the agarose gel and appears mechnically undamaged.

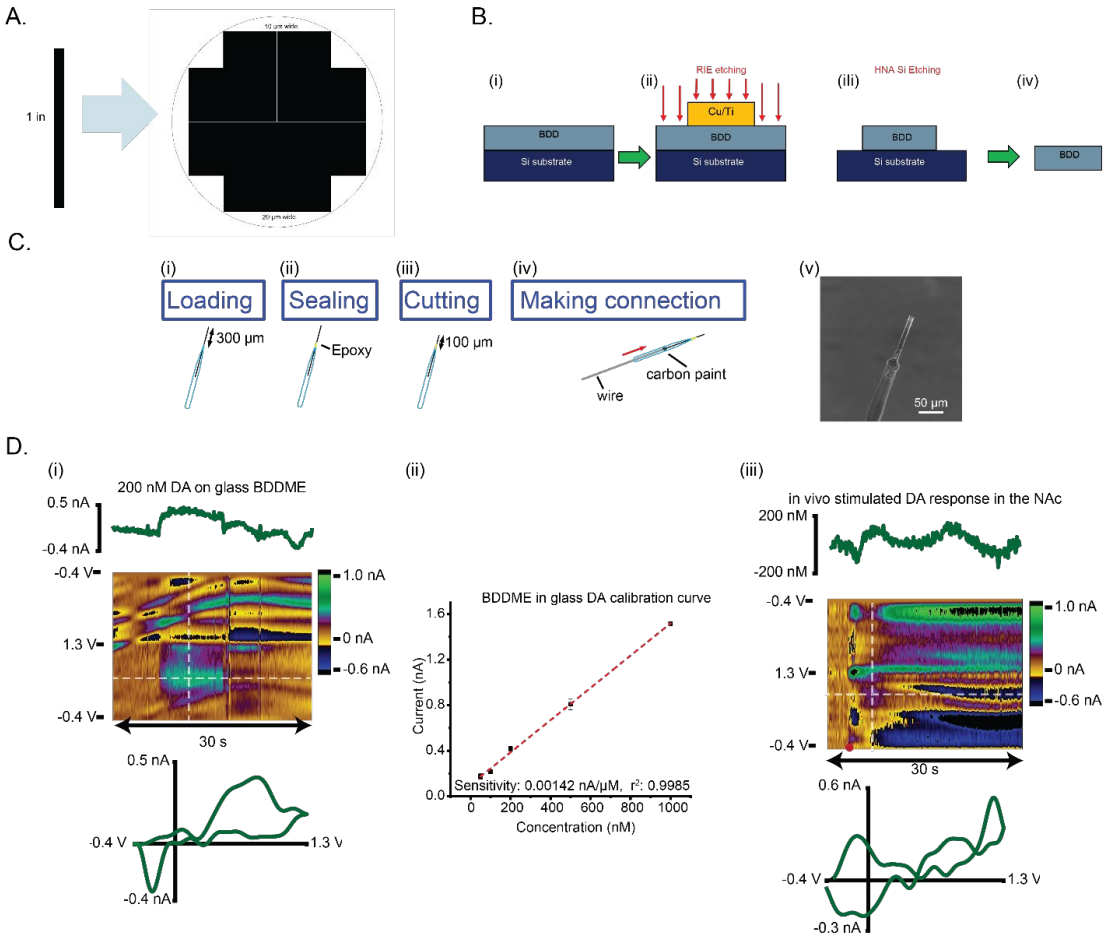


**Figure S2.7.** Fabrication and *in vivo* response of diamond electrode. **A.** BDD strips were designed into 1 inch long, 10 and 20 µm wide and 4 µm thick strips. **B.** The fibers were fabricated by (**B.i**) growing 4 µm thick BDD film on a 4 in diameter Si wafer in a conformal thin film. (**B.ii**) Using reactive ion etching, the pattern was transferred onto the film. (**B.iii**) BDD was released from the Si substrate using HNA etching (nitric, acetic, and hydrofluoric acid) to release (**B.iv**) the fibers. **C.** diamond in glass electrodes were fabricated by (**C.i**) loading a strip into the tip of a pulled capillary and sealing (**C.ii**) the tip with epoxy. The BDD strip was cut (**C.iii**) to ~100 µm from the edge of the epoxy seal, and electrical connection made using a wire and carbon paint from the backside to form the diamond in glass electrode (**C.iv**). **D.** (**D.i**) The diamond glass electrodes was tested in vitro in a flow injection system against 200 nM DA. Current vs time, and the extracted voltammogram showed excellent resolution for electrochemical detection. (**D.ii**) A linear calibration curve from 50 nM to 1000 nM for DA (n=1 electrode) maintained a linear response. (**D.iii**) Stim-evoked *in vivo* DA response recorded with a BDD implanted in the rat NAc post MFB stimulation. Stimulation (red dot on color plot) was set at 575 µA following 3 s from the start of the recording. The evoked DA response measured can be seen at the vertical slice, and the concentration from the horizontal slice (*n*=1 animal).

## REFERENCES


(1) Cho, Y., Park, S., Lee, J. & Yu, K. J. Emerging Materials and Technologies with Applications in Flexible Neural Implants: A Comprehensive Review of Current Issues with Neural Devices. *Advanced Materials* 33, 2005786 (2021).

(2) Liu, Y., Liu, Z., Zhou, Y. & Tian, Y. Implantable Electrochemical Sensors for Brain Research. *JACS Au* 3, 1572–1582 (2023).

(3) Veletić, M. *et al.* Implants with Sensing Capabilities. *Chem Rev* 122, 16329–16363 (2022).

(4) Salatino, J. W., Ludwig, K. A., Kozai, T. D. Y. & Purcell, E. K. Glial responses to implanted electrodes in the brain. *Nat Biomed Eng* 1, 862–877 (2017).

(5) Herrington, T. M., Cheng, J. J. & Eskandar, E. N. Mechanisms of deep brain stimulation. *J Neurophysiol* 115, 19–38 (2016).

(6) Lee, K. H. *et al.* Emerging techniques for elucidating mechanism of action of deep brain stimulation. in *2011 Annual International Conference of the IEEE Engineering in Medicine and Biology Society* 677–680 (IEEE, 2011). doi:10.1109/IEMBS.2011.6090152.

(7) Kogan, M., McGuire, M. & Riley, J. Deep Brain Stimulation for Parkinson Disease. *Neurosurg Clin N Am* 30, 137–146 (2019).

(8) Cho, Y. U., Lim, S. L., Hong, J.-H. & Yu, K. J. Transparent neural implantable devices: a comprehensive review of challenges and progress. *npj Flexible Electronics* 6, 53 (2022).

(9) Hong, G. & Lieber, C. M. Novel electrode technologies for neural recordings. *Nat Rev Neurosci* 20, 330–345 (2019).

(10) Shi, J. & Fang, Y. Flexible and Implantable Microelectrodes for Chronically Stable Neural Interfaces. *Advanced Materials* 31, 1804895 (2019).

(11) Seaton, B. T., Hill, D. F., Cowen, S. L. & Heien, M. L. Mitigating the Effects of Electrode Biofouling-Induced Impedance for Improved Long-Term Electrochemical Measurements In Vivo. *Anal Chem* 92, 6334–6340 (2020).

(12) Gupta, B. *et al.* In Vitro Biofouling Performance of Boron-Doped Diamond Microelectrodes for Serotonin Detection Using Fast-Scan Cyclic Voltammetry. *Biosensors (Basel)* 13, 576 (2023).

(13) Kuhlmann, J., Dzugan, L. C. & Heineman, W. R. Comparison of the Effects of Biofouling on Voltammetric and Potentiometric Measurements. *Electroanalysis* n/a-n/a (2012) doi:10.1002/elan.201200194.

(14) Wisniewski, N., Moussy, F. & Reichert, W. M. Characterization of implantable biosensor membrane biofouling. *Fresenius J Anal Chem* 366, 611–621 (2000).

(15) Purcell, E. *et al.* Next-Generation Diamond Electrodes for Neurochemical Sensing: Challenges and Opportunities. *Micromachines (Basel)* 12, 128 (2021).

(16) Puthongkham, P. & Venton, B. J. Recent advances in fast-scan cyclic voltammetry. *Analyst* 145, 1087–1102 (2020).

(17) Si, B. & Song, E. Recent Advances in the Detection of Neurotransmitters. *Chemosensors* 6, 1 (2018).

(18) Patel, P. R. *et al.* Insertion of linear 8.4 μm diameter 16 channel carbon fiber electrode arrays for single unit recordings. *J Neural Eng* 12, 046009 (2015).

(19) Schwerdt, H. N. *et al.* Subcellular probes for neurochemical recording from multiple brain sites. *Lab Chip* 17, 1104–1115 (2017).

(20) Zachek, M. K., Park, J., Takmakov, P., Wightman, R. M. & McCarty, G. S. Microfabricated FSCV-compatible microelectrode array for real-time monitoring of heterogeneous dopamine release. *Analyst* 135, 1556 (2010).

(21) Nimbalkar, S. *et al.* Ultra-Capacitive Carbon Neural Probe Allows Simultaneous Long-Term Electrical Stimulations and High-Resolution Neurotransmitter Detection. *Sci Rep* 8, 6958 (2018).

(22) Castagnola, E. *et al.* Glassy carbon microelectrode arrays enable voltage-peak separated simultaneous detection of dopamine and serotonin using fast scan cyclic voltammetry. *Analyst* 146, 3955–3970 (2021).

(23) Xia, M. *et al.* Scalable, flexible carbon fiber electrode thread arrays for three-dimensional probing of neurochemical activity in deep brain structures of rodents. *Biosens Bioelectron* 241, 115625 (2023).

(24) Li, J. *et al.* A tissue-like neurotransmitter sensor for the brain and gut. *Nature* 606, 94–101 (2022).

(25) Castagnola, E., Garg, R., Rastogi, S. K., Cohen-Karni, T. & Cui, X. T. 3D fuzzy graphene microelectrode array for dopamine sensing at sub-cellular spatial resolution. *Biosens Bioelectron* 191, 113440 (2021).

(26) Fan, B. *et al.* Flexible, diamond-based microelectrodes fabricated using the diamond growth side for neural sensing. *Microsyst Nanoeng* 6, 42 (2020).

(27) Rusinek, C. A. *et al.* All-Diamond Microfiber Electrodes for Neurochemical Analysis. *J Electrochem Soc* 165, G3087–G3092 (2018).

(28) Rusinek, C. A., Becker, M. F., Rechenberg, R. & Schuelke, T. Fabrication and characterization of boron doped diamond microelectrode arrays of varied geometry. *Electrochem commun* 73, 10–14 (2016).

(29) Dong, H., Wang, S., Galligan, J. J. & Swain, G. M. *Boron-Doped Diamond Nano/Microelectrodes for Biosensing and in Vitro Measurements*. *Frontiers in Bioscience* vol. 3 (2011).

(30) Puthongkham, P. & Venton, B. J. Nanodiamond Coating Improves the Sensitivity and Antifouling Properties of Carbon Fiber Microelectrodes. *ACS Sens* 4, 2403–2411 (2019).

(31) Manciu, F. S. *et al.* Analysis of Carbon-Based Microelectrodes for Neurochemical Sensing. *Materials* 12, 3186 (2019).

(32) Pasquarelli, A., Picollo, F. & Carabelli, V. Boron-Doped Diamond and Graphitic Multiarrays for Neurotransmitter Sensing. 19–65 (2018) doi:10.1007/5346_2018_24.

(33) Carabelli, V. *et al.* Planar Diamond-Based Multiarrays to Monitor Neurotransmitter Release and Action Potential Firing: New Perspectives in Cellular Neuroscience. *ACS Chem Neurosci* 8, 252–264 (2017).

(34) Tomagra, G. *et al.* Diamond-based sensors for in vitro cellular radiobiology: Simultaneous detection of cell exocytic activity and ionizing radiation. *Biosens Bioelectron* 220, 114876 (2023).

(35) Gosso, S. *et al.* Heterogeneous distribution of exocytotic microdomains in adrenal chromaffin cells resolved by high-density diamond ultra-microelectrode arrays. *J Physiol* 592, 3215 (2014).

(36) Siegenthaler, J. R., Gushiken, B. C., Hill, D. F., Cowen, S. L. & Heien, M. L. Moving Fast-Scan Cyclic Voltammetry toward FDA Compliance with Capacitive Decoupling Patient Protection. *ACS Sens* 5, 1890–1899 (2020).

(37) Bucher, E. S. *et al.* Flexible software platform for fast-scan cyclic voltammetry data acquisition and analysis. *Anal Chem* 85, 10344–10353 (2013).

(38) Perillo, M. L. *et al.* Evaluation of In Vitro Serotonin-Induced Electrochemical Fouling Performance of Boron Doped Diamond Microelectrode Using Fast-Scan Cyclic Voltammetry. *Biosensors (Basel)* 14, 352 (2024).

(39) Elgrishi, N. *et al.* A Practical Beginner's Guide to Cyclic Voltammetry. *J Chem Educ* 95, 197–206 (2018).

(40) Bard, A. J. & Faulkner, L. R. *Electrochemical Methods: Fundamentals and Applications*. (John Wiley & Sons, Inc, New York, 2001).

(41) Jarošová, R., De Sousa Bezerra, P. M., Munson, C. & Swain, G. M. Assessment of heterogeneous electron-transfer rate constants for soluble redox analytes at tetrahedral amorphous carbon, boron-doped diamond, and glassy carbon electrodes. *physica status solidi (a)* 213, 2087–2098 (2016).

(42) Bucher, E. S. & Wightman, R. M. Electrochemical Analysis of Neurotransmitters. *Annu Rev Anal Chem (Palo Alto Calif)* 8, 239–261 (2015).

(43) Venton, B. J. & Cao, Q. Fundamentals of fast-scan cyclic voltammetry for dopamine detection †. *CRITICAL REVIEW Cite this: Analyst* 145, 1158 (2020).

(44) Tan, S. Y., Chia, V. Y. Y., Hölttä-Otto, K. & Anariba, F. Teaching the Nernst Equation and Faradaic Current through the Use of a *Designette:* An Opportunity to Strengthen Key Electrochemical Concepts and Clarify Misconceptions. *J Chem Educ* 97, 2238–2243 (2020).

(45) Rodeberg, N. T., Sandberg, S. G., Johnson, J. A., Phillips, P. E. M. & Wightman, R. M. Hitchhiker's Guide to Voltammetry: Acute and Chronic Electrodes for in Vivo Fast-Scan Cyclic Voltammetry. *ACS Chem Neurosci* 8, 221–234 (2017).

(46) Singh, Y. S. *et al.* Boron-Doped Diamond Microelectrodes Reveal Reduced Serotonin Uptake Rates in Lymphocytes from Adult Rhesus Monkeys Carrying the Short Allele of the 5-HTTLPR. *ACS Chem. Neurosci* 1, 49–64 (2010).

(47) Park, J. *et al.* Diamond microelectrodes for use in biological environments. *Journal of Electroanalytical Chemistry* 583, 56–68 (2005).

(48) Kasahara, S. *et al.* Surface Hydrogenation of Boron-Doped Diamond Electrodes by Cathodic Reduction. *Anal Chem* 89, 11341–11347 (2017).

(49) McCreery, R. L. Advanced Carbon Electrode Materials for Molecular Electrochemistry. *Chem Rev* 108, 2646–2687 (2008).

(50) Bath, B. D. *et al.* Subsecond Adsorption and Desorption of Dopamine at Carbon-Fiber Microelectrodes. *Anal Chem* 72, 5994–6002 (2000).

(51) Roberts, J. G., Moody, B. P., McCarty, G. S. & Sombers, L. A. Specific Oxygen-Containing Functional Groups on the Carbon Surface Underlie an Enhanced Sensitivity to Dopamine at Electrochemically Pretreated Carbon Fiber Microelectrodes. *Langmuir* 26, 9116–9122 (2010).

(52) Dec, B. *et al.* Gas Composition Influence on the Properties of Boron-Doped Diamond Films Deposited on the Fused Silica. *Materials Science-Poland* 36, 288–296 (2018).

(53) John, C. E. & Jones, S. R. Fast Scan Cyclic Voltammetry of Dopamine and Serotonin in Mouse Brain Slices. *Electrochemical Methods for Neuroscience* 49–62 (2007) doi:10.1201/9781420005868.ch4.

(54) Hashemi, P., Dankoski, E. C., Petrovic, J., Keithley, R. B. & Wightman, R. M. Voltammetric detection of 5-hydroxytryptamine release in the rat brain. *Anal Chem* 81, 9462–9471 (2009).

(55) Jennings, K. A. A Comparison of the Subsecond Dynamics of Neurotransmission of Dopamine and Serotonin. *ACS Chem Neurosci* 4, 704 (2013).

(56) Pomfret, R., Miranpuri, G. & Sillay, K. The Substitute Brain and the Potential of the Gel Model. *Ann Neurosci* 20, (2013).

(57) Vreeland, R. F. *et al.* Biocompatible PEDOT:Nafion composite electrode coatings for selective detection of neurotransmitters in vivo. *Anal Chem* 87, 2600–7 (2015).

(58) Thompson, C. H., Saxena, A., Heelan, N., Salatino, J. & Purcell, E. K. Spatiotemporal patterns of gene expression around implanted silicon electrode arrays. *J Neural Eng* 18, 045005 (2021).

(59) Parent, K. L. *et al.* Platform to Enable Combined Measurement of Dopamine and Neural Activity. *Anal Chem* 89, 2790–2799 (2017).

# CHAPTER 3 | IN VITRO BIOFOULING PERFORMANCE OF BORON-DOPED DIAMOND MICROELECTRODES FOR SEROTONIN DETECTION USING FAST-SCAN CYCLIC VOLTAMMETRY

## 3.1 INTRODUCTION

Neurotransmission, or the cellular communication among neurons, is driven by both chemical and electrical impulses [1]. Chemical interactions take place when a cell releases neurotransmitters that are detectable by surrounding cells and/or itself [2]. A commonly used method to study neurotransmitter release is fast-scan cyclic voltammetry (FSCV), which allows for the detection of electrochemically active compounds on a sub-second timescale. FSCV is a background-subtracted technique that typically employs carbon fiber microelectrodes (CFMEs) to repeatedly apply brief voltage waveforms to induce oxidation and reduction in analytes of interest. The generated current from the movement of electrons at specific applied potentials allows for identification of the neurotransmitter and the resultant concentration based on the measured current magnitude. Over the last thirty years, FSCV has been developed and optimized for the detection of several common neurotransmitters, including serotonin (5-HT), dopamine (DA), norepinephrine (NE), histamine, and adenosine [3–11].

Recently, our team developed an all-diamond, boron-doped diamond microelectrode (BDDME) for electrochemical measurements [12,13]. Unlike other BDDMEs which are grown on tungsten or platinum metals and insulated with a polymer and CFMEs, this all-diamond electrode is freestanding, insulated with polycrystalline diamond (PCD), and batch-fabricated using wafer processing techniques. Wafer fabrication allows for ease and flexibility to produce numerous custom-fabricated electrode shapes and geometries on a single wafer, all having extremely similar

performances, and removes some of the human error during traditional hand fabrication techniques such as those for CFMEs and other BDDMEs [14–17]. Several studies [12,18–22] have shown BDD to be an extremely versatile material for electrochemical applications due to its (1) wide working potential windows; (2) lower background currents; (3) good mechanical and chemical stability; (4) good electrochemical activity without pre-treatment; and (5) resistance to fouling. However, the nature of the BDD surface in comparison to CFMEs can also yield reduced sensitivity and slower electron transfer kinetics [23,24]. Nonetheless, numerous opportunities remain to more effectively leverage the potential benefits of BDDMEs, and optimization of the applied waveform is an easily implemented first approach to improve results.

Several waveform parameters, including the scan rate, holding potential, switching potential, and frequency, are known to influence the detected current at CFMEs [25]. Much previous work has driven the development of CFMEs to sensitively and selectively detect neurotransmitters of interest; for example, the standard waveform swept from −0.4 V to 1.3 V back to −0.4 V at 400 V $s^{-1}$ and applied at 10 Hz is widely utilized today to detect DA [25]. Similarly, Jackson et al. (1995) developed the N-shaped waveform starting at 0.2 V to 1.0 V to −0.1 V at 1000 V $s^{-1}$ and applied at 10 Hz, specifically to increase and isolate the 5-HT oxidation peak current, while minimizing electrode fouling [26]. Waveform optimization tailored the electrochemical response of 5-HT on the CFMEs surface and has shown that: (1) the rate of adsorption of 5-HT is higher with an N-shaped waveform compared to the triangular waveform; (2) the 5-HT current amplitude is 10 times greater when scanning at 1000 V $s^{-1}$ compared to 100 V $s^{-1}$; (3) an interferent electrochemical couple is less apparent at the faster scan rate of 1000 V $s^{-1}$, and; (4) holding the potential at 0.2 V minimized interference by 5-HT oxidation byproducts which can build-up and polymerize on the electrode surface [26,27].

Modified FSCV waveform parameters provide insight into analyte detection and electrode surface interactions. With the triangular waveform at CFMEs, Heien et al. (2003) demonstrated increased sensitivity of DA and other neurotransmitters, including 5-HT, by extending the switching potential from 1.0 V to 1.4 V [28]. Recently, Venton's group investigated an extended version of the Jackson waveform at CFMEs to attain low electrode fouling and higher sensitivity for measurements in vivo [29]. In particular, the switching potential of the Jackson waveform was extended to 1.3 V, so that the CFME surface could be constantly regenerated [30]. The Jackson waveform was determined to be the most selective for 5-HT, while the extended waveform had increased electrode sensitivity [29]. A key advantage of higher switching potentials is CFME surface activation, facilitated by the breakage of carbon–carbon bonds and addition of edge plane sites to promote analyte adsorption and surface cleaning at the electrode [25,30,31]. In an in vivo setting, such extended waveforms or higher switching potentials could be advantageous where electrode fouling and/or selectivity are prominent issues [29].

A major recognized challenge of in vivo neurotransmitter detection at the CFME is biofouling: the adsorption of biomolecules or proteins at the inserted electrode [25]. Implantation of a chronic electrode facilitates a cascade of immune response in the tissue [32–34]. Protein deposits on the electrode surface can disrupt analyte adsorption, slow electron transfer, and interfere with voltammetric performance [25,34–36]. The detection of 5-HT in vivo is especially challenging because of the added burden of oxidizable, reaction-specific side-products that irreparably foul the CFME surface [27]. The Swain group has reported significantly reduced 5-HT fouling on BDDMEs with amperometric detection compared to bare CFMEs [37] and Nafion-coated CFMEs [38]. The $sp^3$ carbon structure, extended π-electron system, and fewer carbon–

oxygen surface groups make the BDD resistant to high adsorption of molecules, potentially resulting in reduced fouling at the electrode surface [37,38].

In this work, we sought to characterize the in vitro FSCV electrode behavior and biofouling performance of our freestanding BDDME compared to the traditional CFME. First, we report on 5-HT responses at the BDDMEs and CFMEs over a range of FSCV parameters such as scan rate, holding potential, switching potential, frequency, and concentrations; this work is an extension of our previous conference proceeding [39]. Second, we studied the biofouling effects on the 5-HT current at both electrodes with the standard waveform. Third, we investigated biofouling-induced changes to 5-HT responses at both electrodes with the Jackson waveform. We found that the BDDME showed lower electrode fouling with increasing or changing switching potentials, frequency, and analyte concentrations, in comparison with CFMEs. Biofouling effects were significantly less pronounced at the BDDME with the Jackson waveform compared to CFMEs. The CFMEs maintain higher sensitivity and excellent LODs for 5-HT in comparison with BDDMEs for all conditions. These experiments are important steps towards optimizing the detection performance of the BDDME for in vivo neurotransmitter sensing applications.

## 3.2 MATERIALS AND METHODS

### 3.2.1 CHEMICALS

All chemicals were purchased from Sigma-Aldrich, Inc. (St. Louis, MO, USA) and Fisher Scientific International, Inc. (Hampton, NH, USA). Stock solutions of 1 mM 5-HT were prepared in 1 mM perchloric acid and used within 24 h to prevent solution degradation. Diluted solutions of 5-HT were prepared in artificial cerebrospinal fluid (aCSF) (pH 7.4; 20.68 mM Trizma hydrochloride, 4.32 mM Trizma Base, 126 mM NaCl, 2.5 mM KCl, 1.2 mM $NaH_2PO_4$, 2.4 mM

$CaCl_2$, 1.2 mM $MgCl_2$). Solutions of 1 mM ferrocene carboxylic acid (FcCOOH), a highly electroactive compound with a well-documented redox response with FSCV, were prepared in aCSF and used to test for optimal placement of microelectrodes in the flow injection setup before measurements were recorded. For all biofouling experiments, a 4% solution of bovine serum albumin (BSA; 40 $gL^{-1}$ in aCSF, pH 7.4) was freshly prepared before electrode soaking. All solutions were prepared with ultrapure water: 18.2 MΩ.cm, TOC < 5 ppb (Barnstead™ GenPure™ xCAD Plus Ultrapure Water Purification System, Thermo Scientific, Waltham, MA, USA).

### 3.2.2 CARBON FIBER MICROELECTRODE (CFME) FABRICATION

CFMEs were constructed similarly to previously reported methods [30]. Briefly, 7.4 µm Ø, unsized, AS4 carbon fibers (Hexel, Stamford, CT, USA) were aspirated into glass capillaries (World Precision Instruments, Sarasota, FL, USA) using a vacuum pump. These capillaries were pulled with a vertical micropipette puller (Stoelting Co., Wooddale, IL, USA). An electrical connection was made by coating 32 AWG wire wrapping wire with PELCO conductive carbon-based glue (Ted Pella, Inc., Redding, CA, USA) and inserting it into the open end of the capillary and epoxying it in place. The carbon fibers were then cut to an approximate 100–150 µm exposed length measured from the glass seal. All CFMEs, unless otherwise noted, were allowed to stabilize for 20–30 min using the standard cyclic waveform of −0.4 V to 1.3 V at 400 V $s^{-1}$, 60 Hz frequency in aCSF, and then allowed to finish stabilizing for 10 min at 10 Hz before being used for experimentation.

### 3.2.3 BORON-DOPED DIAMOND MICROELECTRODE (BDDME) FABRICATION

This fabrication scheme was based on a previous report [13] with some modifications, described as follows. The fabrication of the BDDMEs is a multi-step chemical vapor deposition process, which includes photolithography, metal masking, and dry etching. The fabrication scheme

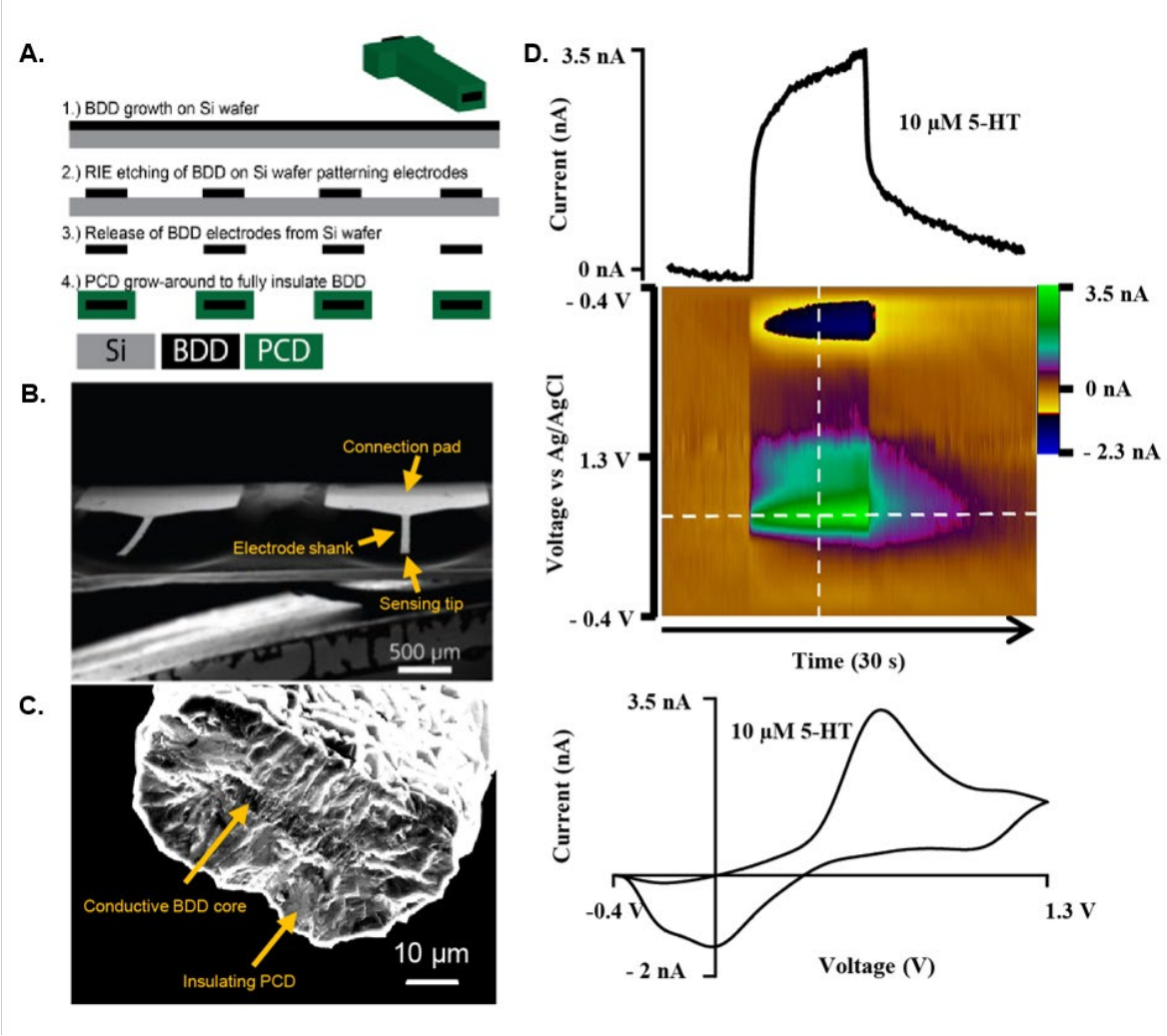


**Figure 3.1.** Representative fabrication scheme and FSCV response of the BDDME. **A**. Fabrication scheme of the BDDME using wafer processing technology, in which the BDD is grown, and insulating PCD is then utilized to encapsulate the BDD core. **B**. Scanning Electron Microscope (SEM) image of the individual, free-standing BDDME showcasing a connection pad and electrode shank. **C**. SEM image of a BDDME sensing tip, with a BDD core area of 123 $\mu m^2$ and polycrystalline diamond (PCD) encapsulation shell with a 15 µm thick layer. **D**. Representative FSCV response of 10 µM 5-HT in aCSF at the BDDME with a flow rate of 750 $\mu L\ min^{-1}$, and an applied waveform of −0.4 V to 1.3 V to −0.4 V at 400 V $s^{-1}$ and 10 Hz repetition rate. Extracted current vs. time trace of the peak oxidation current (**top**) and cyclic voltammogram (**bottom**) showcase the electrochemical response of the BDDME when measuring 5-HT with the BDDME.

(**Figure 3.1A**) represents the basic key wafer processing steps. Briefly, BDD films were grown on a 4″ Ø-500 µm thick single-side polished silicon wafer using a 915 MHz microwave chemical vapor deposition reactor. Synthesis conditions include a microwave power of 9 kW, a 900 °C stage

temperature, a chamber pressure of 60 Torr and a gas chemistry of 2% methane. Diborane was added to the diamond grown at a B/C ratio of 37,500 ppm to ensure conductivity. Following BDD growth, copper was thermally evaporated (Auto 306; Edward, Inc., West Sussex, UK) and patterned via photolithography (ABM-USA, Inc., Jan Jose, CA, USA), followed by wet chemical etching and reactive ion etching. The diamond electrodes were then released from the silicon using an HNA etchant with an $HF:HNO_3:CH_3COOH$ composition of 5:11:6, and fully insulated with polycrystalline microcrystalline diamond using hot filament chemical vapor deposition (HF-CVD). Microcrystalline diamond was grown using a base pressure of 35 Torr and 2% methane on the freestanding released BDDMEs (**Figure 3.1B**). After deposition, the ends of the electrodes were physically cleaved to expose the BDD core, and the electrical connection was made using the conductive carbon glue (Ted Pella, Inc., Redding, CA, USA). Electroactive areas for the diamond cores ranged from 100 to 200 $\mu m^2$ based on a 50 μm wide pattern, and a BDD growth thickness of ~2–4 μm (**Figure 3.1C**).

### 3.2.4 FAST-SCAN CYCLIC VOLTAMMETRY (FSCV) INSTRUMENTATION

A two-electrode setup (a working electrode versus a quasi Ag/AgCl reference electrode) was utilized in a custom flow injection cell for FSCV experiments. A self-constructed potentiostat with a variable gain headstage (50 nA/V, 100 nA/V, 200 nA/V, 500 nA/V, 1 μA/V) was connected to the electrode to carry out measurements. Data were collected using a NI-6363 data acquisition card and HDCV software (Version 4, Department of Chemistry, University of North Carolina, Chapel Hill, NC, USA) [40]. For all experiments, the flow injection system used a TTL voltage-controlled source to switch a six-way HPLC valve to introduce a bolus of test analyte. A flow rate of 0.75 mL $min^{-1}$ was used to deliver aCSF buffer by a NE-1000 syringe pump (New Era Pump Systems, Inc., Farmingdale, NY, USA).

### 3.2.5 WAVEFORM PARAMETER INVESTIGATION

The waveform factors section of the study utilized the "standard" triangular FSCV waveform, −0.4 V to 1.3 V and back at 400 V $s^{-1}$ at 10 Hz as the baseline. The peak oxidative 5-HT current value was used to determine the effects of different waveform parameters. The following parameters were adjusted individually in the HDCV software: frequency, holding potential, switching potential, scan rate, and analyte concentration (0.025 µM up to 100 µM). For non-calibration experiments, baseline 5-HT concentrations were used for the two electrode types, 1 µM for CFMEs and 10 µM for BDDMEs due to differences in electrode sensitivity. Each data value was obtained by averaging the current response across three injections of 5-HT into the flow cell system, unless otherwise stated. An example redox response to 10 µM 5-HT at the BDDME using FSCV is presented in **Figure 3.1D**.

### 3.2.6 BIOFOULING PROTOCOL

The in vitro biofouling of the microelectrodes was performed utilizing protocols published by Singh et al. (2011) [41], with minor changes. Briefly, electrodes were pre-calibrated with 5-HT (0.025 µM to 1 µM 5-HT for the CFMEs, and 0.2 µM to 10 µM 5-HT for the BDDMEs) and placed in BSA for ~12 h. For the duration of BSA exposure, the electrodes were fixed in a beaker containing 4% BSA in aCSF and only the tips were submerged in the solution. After removal, electrodes were post-calibrated with 5-HT, similarly within 24 h. Prior to post-calibration and following placement in the flow injection system, electrodes were positioned in the flow path and the previously measured highest concentration of 5-HT was detected to eliminate the influence of surface refreshing and pre-mature removal of any absorbed BSA (i.e., 1 µM 5-HT at CFMEs and 10 µM 5-HT at BDDMEs). Two waveforms were investigated at both CFMEs and BDDMEs to assess biofouling effects (see Supplementary Materials, **Figure S3.1**)—(1) the standard waveform

and (2) the Jackson waveform. For each waveform condition, batches of freshly fabricated CFMEs and BDDMEs were employed.

### 3.2.7 DATA ANALYSIS

Raw data were extracted using the HDCV analysis software, and exported to a text file. Responses were then analyzed using in-house-developed FSCV analysis software for filtering and analysis. All data were filtered using a Butterworth 4th order lowpass filter at 1660 Hz for scan rates of 400 V $s^{-1}$ and 8000 Hz for scan rates of 1000 V $s^{-1}$. The data was also zero-phase filtered to preserve the phase shift in the current response with respect to the applied potential induced by digital filtering. Graphs were drawn and statistical analysis was carried out using Graphpad Prism.

## 3.3 RESULTS

The peak oxidative 5-HT current was measured at discrete values of scan rate, holding potential, switching potential, frequency, and analyte concentration for both BDDMEs and CFMEs to compare response trends. Biofouling effects were measured with the standard DA waveform and the Jackson waveform on both electrodes.

### 3.3.1 WAVEFORM FACTORS

#### 3.3.1.1 SCAN RATE

In **Figure 3.2A**, the anodic current increases linearly over the entire range of scan rates 100 V $s^{-1}$ to 1000 V $s^{-1}$ at the CFME, indicating an adsorption-controlled process. The BDDME's current response is linear up to 400 V $s^{-1}$, before beginning to plateau. When plotted as the square-root of the scan rate, the slope becomes linear, potentially indicating a diffusion-controlled process (**Figure S3.2A**).

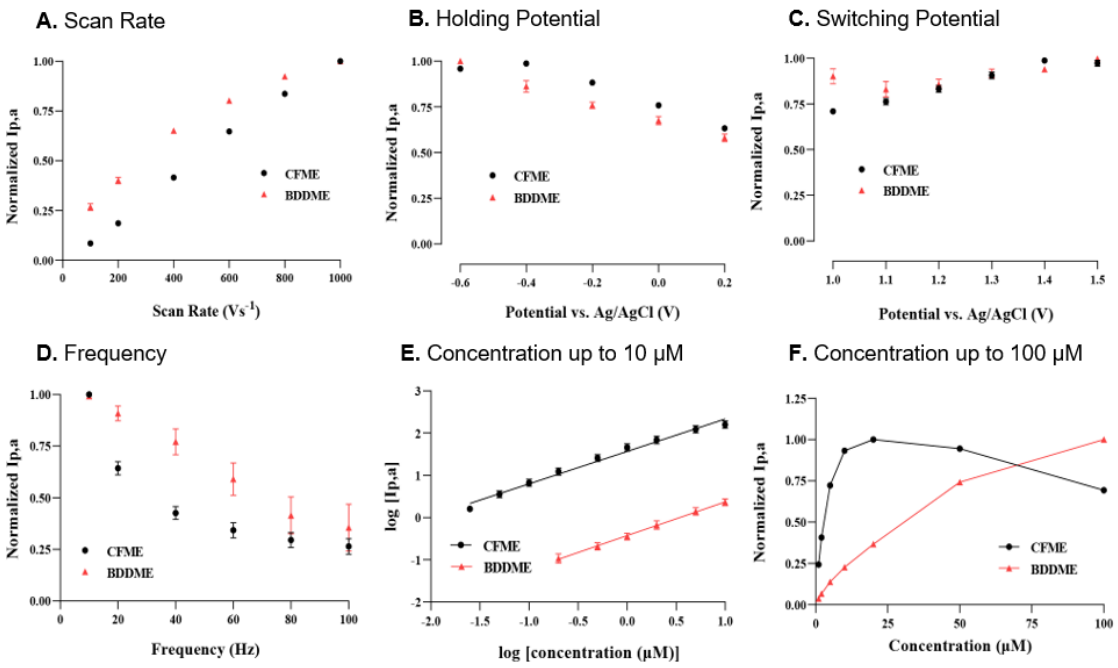


**Figure 3.2.** Factors of the FSCV waveform to determine the peak oxidative response for 5-HT on a CFME and BDDME. **A**. The response of scan rate to peak oxidation, where the scan rate was modified between 100 and 1000 V $s^{-1}$. **B**. The peak current response from changes in the holding potential, varying from −0.6 V to 0.2 V. **C**. 5-HT peak current response to the upper switching potential varying from 1.0 to 1.5 V. **D**. Investigation of the applied waveform application frequency ranging from 10 Hz to 100 Hz. **E**. The response of both the CFME and BDDME to 5-HT varies from 0.05 µM to 1 µM. The non-normalized peak current was plotted as a logarithmic response to better demonstrate the BDDME and CFME response on a comparable scale. **F**. Concentration response from 1 µm to 100 µm, on both the BDDME and CFME to determine the upper detection ranges before sensor saturation. Note that on all plots, peak currents are normalized to the largest current, except in Figure 3.2E where the logarithmic of raw current and concentration are plotted. Data are represented as mean ± SEM CFMEs (n = 5–6) and BDDMEs (n = 5).

### 3.3.1.2 HOLDING POTENTIAL

**Figure 3.2B** demonstrates that the largest oxidative current was measured at −0.6 V, and the peak currents decrease with increasing positive potential for both the BDDME and the CFME. There is one exception, where the CFME has a slight increase in measured response when stepping from −0.6 V to −0.4 V before a continuing decrease.

#### 3.3.1.3 SWITCHING POTENTIAL

Both the BDDME and CFME response to 5-HT differ in response to increasing switching potential (SP) (**Figure 3.2C**). The CFME has an increasing peak current response as the SP is increased up to 1.4 V, with a slight decline at 1.5 V. This trend is only observed in new CFMEs that were previously inactivated, i.e., electrodes have not been subjected to potentials larger than 1.0 V. Conversely, CFMEs that had previously experienced higher SPs show a very slight decreasing trend in response to increasing SP (**Figure S3.2B**). The BDDME maintains a stable anodic peak response for all SPs (with minor fluctuation, but no trend in either direction) regardless of activation and prior use.

#### 3.3.1.4 FREQUENCY

**Figure 3.2D** demonstrates that both microelectrode types exhibit a decreasing peak anodic response with increasing waveform application frequency. The CFME shows an exponential decrease, while the BDDME maintains a linear decrease in peak anodic response. The BDDME application rate indicates a higher resilience in response measurements at higher scanning frequencies than the CFME, further supporting that 5-HT favors a diffusion-controlled process on a BDDME rather than adsorption.

#### 3.3.1.5 CONCENTRATION LOWEST TO 10 µM

Both BDDMEs and CFMEs maintain a linear response to increasing 5-HT concentrations from 0.025/0.2 µM (CFME/BDDME) up to 10 µM. In **Figure 3.2E**, the calibration curves for both electrodes are reported as the logarithmic of raw current vs. logarithmic of concentration to demonstrate the linear responses and measured signal variability. The signal variability between the CFME and BDDME is due to the possible difference in electroactive areas between the

electrodes. The geometric surface area of the CFMEs is estimated to be 1138 to 1578 $\mu m^2$, while the surface area for the BDDME is 123 to 200 $\mu m^2$. The limit of detection (LOD) for the CFME, as determined from the current response of the noise (3 × standard deviation of the noise), was 0.06 μM with a non-logarithmic linear response between 0.02 μM and 0.5 μM, maintaining a sensitivity of 54.59 $nA\mu M^{-1}$ ($R^2 = 0.9937$). Similarly, from the noise response of the electrode, the LOD at BDDMEs was calculated to be 0.52 μM with a linear response 0.2 μM and 5 μM 5-HT and a sensitivity of 0.2901 $nA\mu M^{-1}$ ($R^2 = 0.9951$).

#### 3.3.1.6 CONCENTRATION 1 μM TO 100 μM

**Figure 3.2F** demonstrates that, at concentrations of 5-HT 25 μM, both electrodes lose response linearity. However, the CFME saturates and decreases in the response from 50 μM and 100 μM compared to the BDDME, which maintains an increasing, nonlinear current response up to 100 μM of 5-HT.

### 3.3.2 BIOFOULING EFFECTS

#### 3.3.2.1 STANDARD WAVEFORM

Biofouling-induced changes were studied at both CFMEs and BDDMEs by measuring 5-HT responses on the standard cyclic waveform (−0.4 V to 1.3 V at 400 V $s^{-1}$ and 10 Hz) before and after exposure to BSA. From the calibration response in **Figure 3.2E**, **3.2F**, the 5-HT concentrations for biofouling experiments were chosen as 1 μM at the CFME (**Figure 3.3A–D**) and 10 μM at the BDDME (**Figure 3.3E–H**). **Figure 3.3** shows representative current vs. time traces (I vs. T), color plots, and cyclic voltammograms (CVs) for the CFME and BDDME with the standard waveform. The representative CFME in **Figure 3.3A–D** maintained a 1 μM 5-HT current response of 75.33 nA before biofouling, and a 48.07 nA (a 36.19% decrease) after

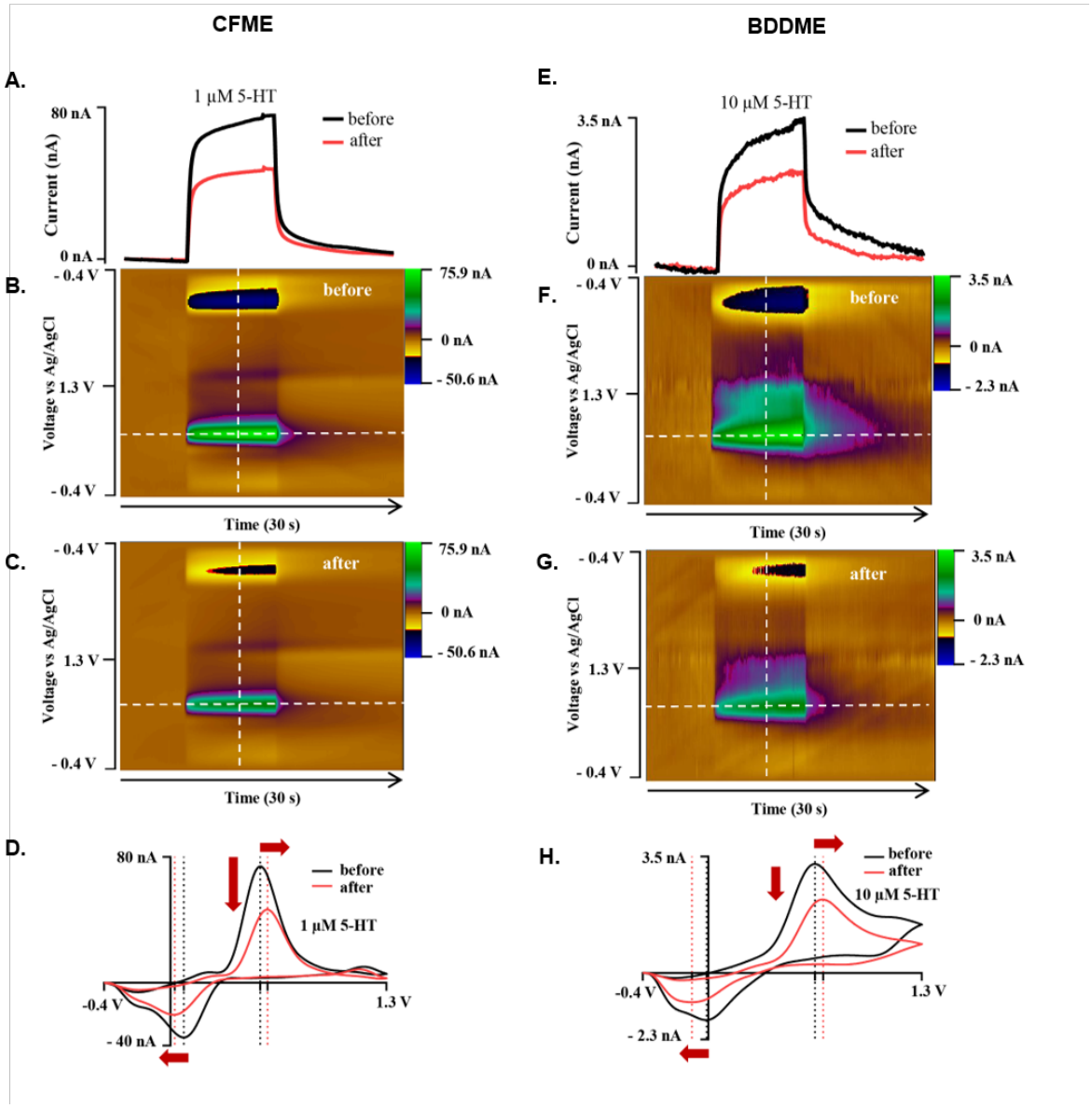


**Figure 3.3.** Representative biofouling effects on the 5-HT response with both the CFME and BDDME using the standard DA waveform from −0.4 V to +1.3V to −0.4 V at a scan rate of 400 V $s^{-1}$ and 10 Hz application frequency. **A**. Current vs. time trace extracted from the color plots (**B**,**C**) for the response of 1 µM 5-HT before and after biofouling the CFME surface. **D**. Extracted voltammogram from the CFME response showing the change in sensitivity from fouling to 1 µM 5-HT. **E**. Current vs. time trace extracted from the color plots (**F**,**G**) for 10 µM 5-HT measured on the BDDME from biofouling the electrode surface. **H**. Extracted cyclic voltammogram from the color plot for the BDDME showcasing the biofouling changes to the measured response. Dashed lines on color plots indicate extracted CV and current vs. time traces. Red arrows in **D** and **H** indicate direction of CV peak shift after biofouling.

biofouling after 12–14 h of soaking in BSA. Similarly, the CV after biofouling showed that the 5-HT oxidation peak decreases and shifts positively from 0.54 V to 0.59 V, while the reduction peak

also decreases and shifts negatively ~0.06 V from 0.08 V to 0.025 V (**Figure 3.3D**). The representative BDDME (**Figure 3.3E–H**) measuring 10 μM 5-HT maintained a 3.52 nA oxidative peak that reduced to 2.35 nA (33% decrease) after biofouling. The 5-HT anodic peak shifted positively from 0.65 V to 0.70 V, while the reduction peak shifted negatively from −0.01 V to −0.1 V (**Figure 3.3H**).

#### 3.3.2.2 JACKSON WAVEFORM

The Jackson waveform (0.2 V to 1.0 V to −0.1 V to 0.2 V at 1000 V $s^{-1}$ and 10 Hz), developed specifically for 5-HT measurement, was employed to understand whether waveform characteristics influence biofouling effects on both the CFME and BDDME. On both the CFME and BDDME, 1 μM and 10 μM of 5-HT were measured both before and after exposure to BSA for 12–14 h on newly fabricated electrodes (**Figure 3.4**). The CFME oxidative current response to 1 μM 5-HT decreased from 45.37 nA to 16.83 nA after BSA exposure (a 62.89% decrease) (**Figure 3.4A–D**). The CV oxidation peak shifted positively from 0.5 V to 0.55 V, and the reduction peak shifted from 0.12 V to 0.05 V (**Figure 3.4D**). The BDDME anodic response for 10 μM 5-HT decreased after exposure to BSA (**Figure 3.4E–H**) from 2.81 nA before biofouling, and reduced by 23.5% to 2.15 nA. The CV oxidative peak shifted from 0.69 V to 0.71 V (**Figure 3.4H**). Due to the increase in the applied scan rate of 1000 V $s^{-1}$, the cathodic sweep was not resolved at the scanned potential window.

#### 3.3.2.3 CALIBRATION CURVES

Both CFMEs and BDDMEs were calibrated before and after biofouling to better understand electrode performance and recovery. **Figure 3.5** demonstrates the linear raw current responses to increasing 5-HT concentrations pre- and post-biofouling at the CFME and BDDME

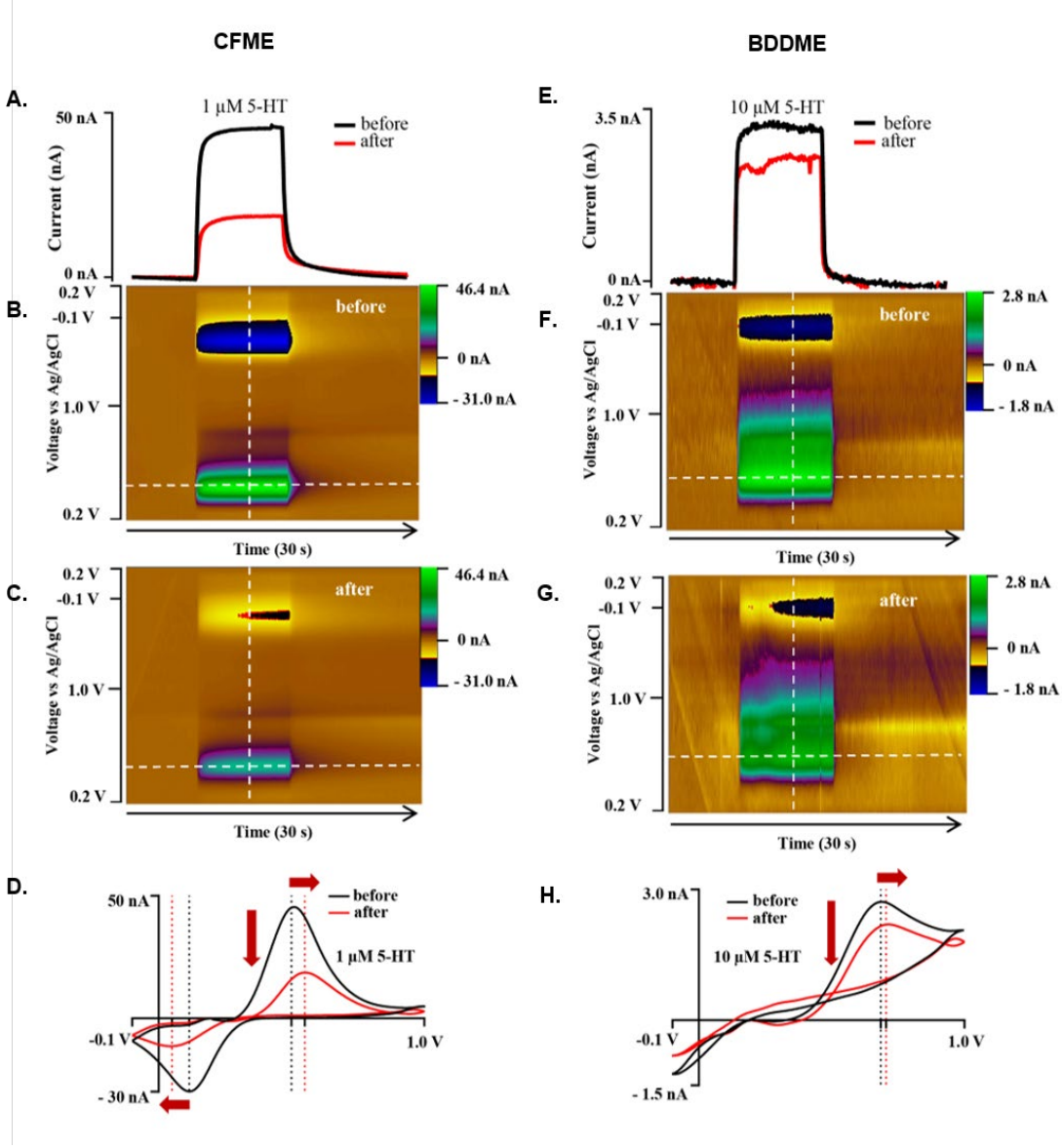


**Figure 3.4.** Representative biofouling effects on the 5-HT response with both the CFME and BDDME using the Jackson waveform 0.2 V to +1.0 V to −0.1 V to 0.2V at a scan rate of 1000 V $s^{-1}$ and 10 Hz application frequency. **A**. Current vs. time trace extracted from the color plots (**B**,**C**) for the response of 1 µM 5-HT before and after biofouling the CFME surface. **D**. Extracted voltammogram from the CFME response showing the change in sensitivity from fouling to 1 µM 5-HT. **E**. Current vs. time trace extracted from the color plots (**F**,**G**) for 10 µM 5-HT measured on the BDDME from before and after biofouling the electrode surface. **H**. Extracted cyclic voltammogram from the color plot for the BDDME showcasing the biofouling changes to the measured response. Dashed lines on color plots indicate extracted CV and current vs. time traces. Red arrows in **D** and **H** indicate direction of CV peaks shift after biofouling.

with the standard and Jackson waveforms. Due to the differences in electrode surface area and

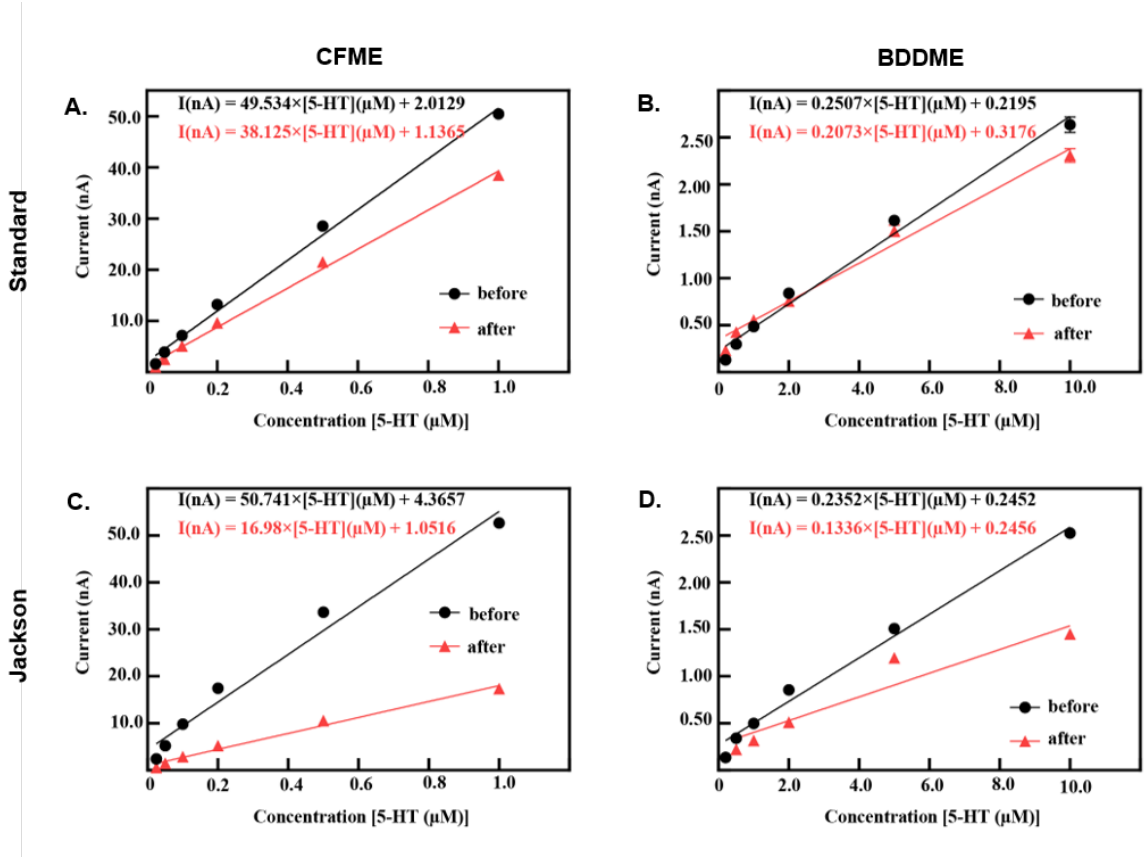


**Figures 3.5.** Calibration curves for both CFME and BDDMEs pre- and post-biofouling. **A,B.** represent 5-HT responses measured using the standard DA waveform before and after biofouling. CFMEs ($n$ = 7) and BDDMEs ($n$ = 2–8). **C**,**D**. Response before and after biofouling on the CFME ($n$ = 7) and BDDME ($n$ = 2–7) to 5-HT measured with the Jackson waveform. Raw currents are plotted as mean ± SEM. Note that some BDDMEs were excluded post-biofouling with both waveforms due to physical issues that resulted in a loss of electrochemical connection between the fiber and conductive pad.

response curves reported in **Figure 3.2E** and 3.**2F**, the 5-HT calibration concentration ranges were chosen as 0.025 μM to 1.0 μM for CFMEs, and 0.2 μM to 10.0 μM for BDDMEs. CFME responses to 5-HT concentrations before and after biofouling on the standard waveform are reported in **Figure 3.5A**. The LOD of 5-HT at the CFME before biofouling was 0.049 μM calculated from the linear best fit equation with a sensitivity of 55.58 nAμM$^{-1}$ ($R^2$ = 0.995). After biofouling, the LOD of 5-HT was maintained at 0.04 μM, but the sensitivity decreased to 42.50 nAμM$^{-1}$ ($R^2$ = 0.997). Before biofouling, the BDDMEs maintained an LOD of 0.26 μM calculated from the linear

**Table 3.1.** Summary of results for 5-HT responses before and after biofouling conditions with the standard waveform.

| Electrode (Standard WF) | LOD * (μM) | Slope * ($nA\mu M^{-1}$) | Measured Range * (μM) | R-Squared * | Biofouling |
|---|---|---|---|---|---|
| CFME | 0.049 | 55.578 | 0.025–0.5 | 0.995 | Before |
| | 0.04 | 42.497 | 0.025–0.5 | 0.997 | After |
| BDDME | 0.26 | 0.385 | 0.2–2.0 | 0.993 | Before |
| | 0.83 | 0.271 | 0.2–2.0 | 0.937 | After |

* CFMEs ($n$ = 7) and BDDMEs ($n$ = 2–8).

**Table 3.2.** Summary of results for 5-HT responses before and after biofouling conditions with the Jackson waveform.

| Electrode (Jackson WF) | LOD * (μM) | Slope * ($nA\mu M^{-1}$) | Measured Range * (μM) | R-Squared * | Biofouling |
|---|---|---|---|---|---|
| CFME | 0.09 | 64.21 | 0.025–0.5 | 0.985 | Before |
| | 0.04 | 42.497 | 0.025–0.5 | 0.997 | After |
| BDDME | 0.4 | 0.383 | 0.2–2.0 | 0.984 | Before |
| | 1.02 | 0.260 | 0.2–2.0 | 0.907 | After |

* CFMEs ($n$ = 7) and BDDMEs ($n$ = 2–7).

best fit equation with a sensitivity of 0.39 $nA\mu M^{-1}$ ($R^2$ = 0.993) (**Figure 3.5B**). After biofouling, the BDDMEs LOD for 5-HT increased to 0.83 μM with a decreased sensitivity of 0.27 $nA\mu M^{-1}$ ($R^2$ = 0.937) (**Table 3.1**).

When using the Jackson waveform for CFME measurements (**Figure 3.5C**), the 5-HT LOD was calculated to be 0.09 μM with a sensitivity of 64.21 $nA\mu M^{-1}$ ($R^2$ = 0.985). After fouling, the CFME had a decrease in sensitivity to 20.52 $nA\mu M^{-1}$ ($R^2$ = 0.988) with an LOD increase of 0.079 μM. The BDDME with the Jackson waveform (**Figure 3.5D**) had an LOD of 0.40 μM and a sensitivity of 0.38 $nA\mu M^{-1}$ ($R^2$ = 0.984). After biofouling, 5-HT LOD increased to 1.02 μM and the sensitivity decreased to 0.26 $nA\mu M^{-1}$ ($R^2$ = 0.907) (**Table 3.2**). It is important to note that some BDDMEs suffered physical issues during biofouling; the electrochemical connection on these

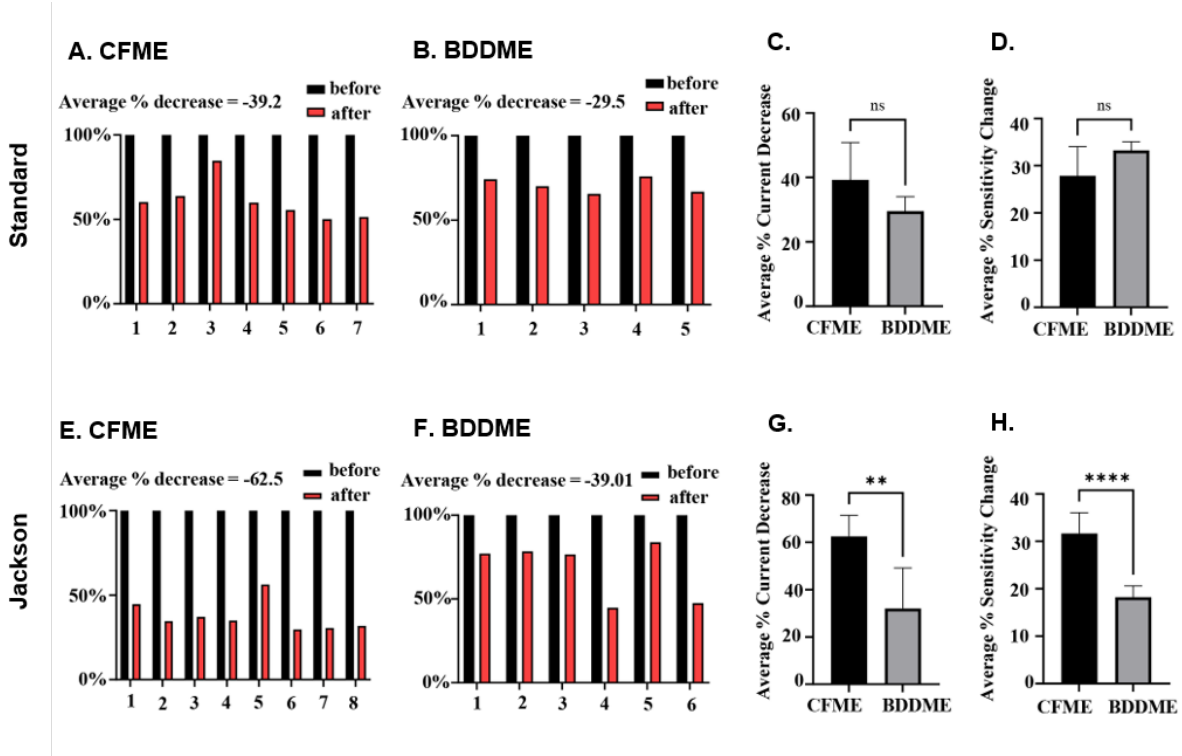


**Figure 3.6. Quantification of biofouling effects on CFMEs and BDDMEs. A**. Individual raw current responses to 1 µM 5-HT at the CFME ($n$ = 7) before and after biofouling with the standard waveform. **B**. Individual raw current response to 10 µM 5-HT at the BDDME ($n$ = 5) before and after biofouling with the standard waveform. **C**. Comparison of average current decrease in 5-HT after biofouling between BDDMEs and CFMEs with the standard waveform; not significant, $p$ = 0.0792. **D**. Average sensitivity decrease after biofouling between BDDMEs and CFMEs with the standard waveform; not significant, $p$ = 0.0885. **E**. Individual raw current responses to 1 µM 5-HT with the CFME ($n$ = 8) before and after biofouling with the Jackson waveform. **F**. Individual raw current response to 10 µM 5-HT with the BDDME ($n$ = 6) before and after biofouling with the Jackson waveform. **G**. Average current decrease in 5-HT after biofouling between BDDMEs and CFMEs with the Jackson waveform; significant, ** $p < 0.05$. **H**. Average sensitivity decrease after biofouling between BDDMEs and CFMEs with the Jackson waveform; significant, **** $p < 0.0001$.

electrodes was weakened, possibly due to contact pad damage or deterioration of carbon glue in the BSA soak model. These electrodes were excluded from the reported datasets.

### 3.3.2.4 STATISTICAL ANALYSIS

The statistical comparison between both CFMEs and BDDMEs with each waveform is shown in **Figure 3.6**. On average, the current response due to biofouling (prior to post-calibration) decreased by −39.2% for the CFMEs when measuring 1 µM 5-HT (**Figure 3.6A**) and −29.5% for

BDDMEs when measuring 10 μM 5-HT (**Figure 3.6B**) with the standard waveform. Although the BDDME showed less percent decrease overall, the average reduction in 5-HT response before vs. after biofouling was not significantly different between the two electrodes (**Figure 3.6C**; Welch's *t*-test, $p = 0.0792$, two-tailed, $t = 2.002$, $df = 8.245$).

When comparing the Jackson waveform, the average current response to 1 μM 5-HT decreased by −62.5% for the CFMEs (**Figure 3.6E**) and by −39.01% for the 10 μM 5-HT on the BDDMEs (**Figure 3.6F**). The overall percentage decrease from before versus after biofouling was significantly different between the two electrodes (**Figure 3.6G**; Welch's *t*-test, $p = 0.0054$, two-tailed, $t = 3.964$, $df = 7.028$). The sensitivity changes between CFMEs and BDDMEs were also significant (Welch's *t*-test, $p < 0.0001$, two-tailed, $t = 6.823$, $df = 9.737$). The BDDME had less of a decrease in sensitivity than CFMEs after biofouling (**Figure 3.6H**) with the Jackson waveform. The average percentage current decrease after biofouling was greater at CFMEs with both waveforms.

## 3.4 DISCUSSION

Successfully and safely maintaining chronic in vivo signals for long periods of time remains a significant challenge for implanted neurochemical sensors [42,43]. Biofouling [36], gliotic cellular encapsulation [32], insertional damage to the device and/or tissue, interferents [44], and polarization of the reference electrode [34] can all undermine the voltammetric response quality in the in vivo environment. We are developing a customizable, all-diamond, microfabricated BDDME to meet these needs, with key advantages for a chronically implanted neurochemical sensor [12]. In this paper, we characterized the current responses on both a CFME and BDDME through varied waveform parameters and biofouling conditions as necessary steps toward characterizing and optimizing detection performance for eventual in vivo usage.

The effects of varying waveform parameters (**Figure 3.2**) largely followed previously reported literature for waveform optimization on a CFME [25,44–46]. Elevated scan rates increased the oxidative current response linearly for the CFMEs, indicating adsorption-controlled processes at this electrode [25]. The sub-linear current response shown on BDDMEs is proportional to the square root of the scan rate, indicating that the background increases faster than the Faradaic currents and kinetics at the electrode may be diffusion-controlled [25] (**Figure S3.2A**). However, the reported data also support potential adsorption-controlled processes on the BDDMEs, as the peak anodic current decreased with increased application frequency of waveform application. Reduced frequency of the applied waveform allows more time for the analyte of interest to adsorb on the electrode surface, enhancing detection [25,47]. It is notable that the attenuation of current with increased frequency is less pronounced on BDDMEs than CFMEs, suggesting that the BDDME measurement of 5-HT is a dual modality measurement. As diamond, which is rich in $sp^3$ carbon, lacks the adsorption sites for other carbon surfaces [48–51], further investigation is warranted on the electron transfer kinetics of the BDDME.

As the holding potential (HP) is decreased, there is a resultant increase in adsorption of 5-HT at the electrode surface [25]. This is observed in the anodic peak current, with the maximum at a HP of −0.6 V for BDDMEs. Similarly, the anodic peak current increased with reduced HP on the CFME, although the current plateaued from −0.4 to −0.6 V, which could be due to the potential window of the CFME in aqueous environments. Near −0.6 V, oxygen reduction would begin to interfere with 5-HT measurements [11,25]. As catecholamines are inherently positively charged at physiological pH, negative HPs are favorable and promote more adsorption due to the electrostatic charge difference [52]. As mentioned, 5-HT is a complex molecule that resides in a reduced state and forms side products upon oxidization that polymerize and foul the carbon fiber

surface for subsequent measurements [27,29]. Previous works have shown that holding at less negative potentials mitigated this fouling effect at CFMEs [26,27]. Furthermore, very negative HPs can facilitate oxygen reduction at CFMEs that may interfere with the recorded analyte current [25]. While CFMEs require adjustments in this parameter for optimal 5-HT detection, BDDMEs may allow for more flexibility due to its resistance to fouling [37] and wide working potential [23].

When a CFME becomes activated through applied potentials above 1.0 V, the current increase is a one-time occurrence, and is non-repeatable for a given CFME. The Wightman group has shown that the CFME surface etches at potentials over 1.0 V [53] and higher switching potentials (~1.3 V) irreversibly etch the electrode surface [30]. Initial exposure to a high potential activates the CFME surface and promotes adsorption at defect sites [25,30]. Our data corroborate this effect, as electrodes that had experienced 1.4 V previously showed a decreasing current with increasing switching potential values from 1.0 V to 1.5 V (**Figure S3.2B**). The caveat to this phenomenon is that the CFME surface will etch away at a non-trivial rate and the surface becomes too small to be effective, particularly in a chronic setting [25,30]. Conversely, at the BDDME, the current response is relatively stable for all switching potentials regardless of prior exposure to higher potential values. Due to its carbon structure and lack of oxygen groups, the BDDME surface may not etch to the same degree as the CFME, suggesting a potential for greater stability in a chronic in vivo setting [12,54].

Analyte concentration vs. oxidative current responses are important to investigate, as detected in vivo signals can fall within the linear range of the in vitro calibrated current curves, allowing the amount of neurotransmitter release to be estimated [25]. The BDDME exhibits a linear oxidative current response from 0.2 μM to 10 μM of 5-HT, while CFME is sensitive to lower concentrations and displays linearity over 0.02 μM to 1 μM of 5-HT. The 5-HT LOD for

BDDMEs was 0.52 μM and 0.06 μM for CFMEs, calculated from the linear best fit equation of the respective calibration ranges. There are two possible reasons for the higher LOD and lower sensitivity at BDDMEs compared to CFMEs: (1) the estimated geometric surface area of our BDDME (123 to 200 $\mu m^2$) is 10 times smaller than that of the CFME (1138 to 1578 $\mu m^2$), and (2) the $sp^3$ carbon structure and lack of carbon–oxygen functional groups prevent surface adsorption of 5-HT at the electrode. The latter is a well-known tradeoff for BDDMEs, and resistance to the high adsorption of analytes has been discussed as a beneficial feature for reducing surface fouling [12,18,37]. In fact, at higher concentrations of 5-HT (1 μM to 100 μM), a fouling effect is especially evident at CFMEs and not observed on the BDDMEs (**Figure 3.2F**). Unlike at the BDDME, the 5-HT responses on the CFME began to decrease rather than plateau after 20 μM, suggesting that the surface was possibly irreversibly fouled. Jackson et al. (1995), as well as Hashemi et al. (2009), showed that 5-HT oxidation, even at 400 V $s^{-1}$, forms byproducts that polymerize and create layers at the electrode surface [26,27], limiting electron transfer and decreasing sensitivity, thereby changing the response of the analyte with time and resulting in accelerated fouling at large concentration exposures [29]. This effect is not observed in the calibration of the BDDMEs, again suggesting potential for greater signal stability and resistance to byproduct fouling. At the same time, the smaller electroactive surface area and lower 5-HT sensitivity of the BDDME could be a major challenge for in vivo detection. Further research will focus on increasing the electroactive area to enable lower concentration detection.

While the Jackson waveform was developed to "outrun" polymerization of the byproducts of 5-HT oxidation, the in vivo environment presents additional detection barriers posed by non-specific adsorption of proteins and subsequent cellular encapsulation of the electrode surface resulting in biofouling [55,56]. As expected, our BSA soak model of biofouling reduced the

detected current on both CFMEs and BDDMEs, in accordance with previous reports. Singh et al. (2011) investigated 1 μM DA response at the bare CFME before and after biofouling by exposing electrodes to a common fouling agent (Bovine Serum Albumin, BSA) and brain tissue (in vivo and in vitro) [41]. The electrode sensitivity to DA decreased significantly in each biofouling condition (60–70% reduction after in vivo brain tissue cycling) [41], which is reasonably well-aligned with our overall detected in vitro 5-HT current decrease of ~40–60% at the CFMEs (**Figure 3.6A,E**). Along with reduced sensitivity, the faradaic peaks shifted in the cyclic voltammograms and calibration curves show signal instability for all after-soak conditions in our experiments. These features are indicative of electrode fouling [21], thereby supporting the view that BSA soaking effectively replicated an in vitro biofouling effect on both CFMEs and BDDMEs.

The lower average 5-HT percent current decrease detected at BDDMEs (−39.01% decrease) in comparison to that at CFMEs (−62.5% decrease) with the N-shaped Jackson waveform (**Figure 3.6E,F**) likely reflects a combination of factors: (1) it has been suggested that BDD is less prone to biofouling [18,37,38], which may be partially attributable to its less adsorptive surface character [27], and (2) 5-HT anodic current responses are less sensitive to switching potentials from 1.0 V to 1.5 V at the BDDME compared to those at the CFME (as observed in **Figure 3.2C** and **Figure S3.2B**). The latter could indicate that the BDDME does not require as much surface refreshing as the CFME for accurate signal measurements in a fouled setting. Another observation to support this idea is that the BDDMEs biofouled more with the Jackson waveform (−39.01% decrease) than with the standard waveform (−29.5% decrease), but not to the same extent as the CFMEs. The CFMEs biofouled much more with the Jackson waveform (−62.5% decrease) than with the standard waveform (−39.2%). Since the Jackson

waveform only scans up to 1.0 V, the CFME surface was not regenerated [30], and possibly experienced more fouling than with the standard waveform which scans up to 1.3 V. The Venton group developed an extended waveform to address this issue at CFMEs and showed reduced electrode fouling when the switching potential of the Jackson waveform was set to 1.3 V compared to 1.0 V [29].

Scanning at higher potentials may also influence electrode recovery after biofouling, as observed in our data where calibration curves for after-soak conditions were steeper with the standard waveform in comparison with the Jackson waveform for both electrodes. The curves demonstrate that after biofouling, the sensitivity to 5-HT concentrations was reduced at both CFMEs and BDDMEs. However, with continuous sweeping of waveforms, both electrodes were able to closely recover to the original current responses with the standard waveform, but neither recovered with the Jackson waveform (**Figure 3.5**). The average percent sensitivity decrease after biofouling at BDDMEs was significantly lower than that at CFMEs with the Jackson waveform (**Figure 3.6H**), further indicating that BDDMEs may not require as much surface cleaning as CFMEs post-fouling. Indeed, as summarized in **Tables 3.1 and 3.2**, BDDME sensitivity decreased from 0.385 $nA\mu M^{-1}$ to 0.271 $nA\mu M^{-1}$ (29% decrease) with the standard waveform, and from 0.383 $nA\mu M^{-1}$ to 0.260 $nA\mu M^{-1}$ (32% decrease) with the Jackson waveform—relatively similar sensitivity decreases of ~30% for both waveforms The CFME sensitivity drops from 55.58 $nA\mu M^{-1}$ to 42.50 $nA\mu M^{-1}$ (−23% decrease) with the standard waveform, and from 64.21 $nA\mu M^{-1}$ to 20.52 $nA\mu M^{-1}$ (−68% decrease) with the Jackson waveform. Nevertheless, it is important to note that the CFME maintains a lower, more stable LOD for 5-HT in each condition with both waveforms.

Overall the reduced sensitivity and higher LODs of 5-HT are an important limitation of the BDDME, as evidenced in our data by the comparatively smaller peak oxidative currents relative to responses detected on CFMEs. This is an important consideration for transfer to the in vivo environment, where neurotransmitters are especially challenging to detect: in addition to fouling and interferents, levels of neurotransmitters in the intact brain are typically in the sub-micromolar range (e.g., stimulus-evoked 5-HT levels reportedly measured at 12.7 ± 1.60 nM in the rat brain [57). Furthermore, the estimated geometric surface area of the rectangular BDDME is roughly 10 times smaller than the cylindrical CFME in this study. This could be a major challenge in vivo, as large-surface-area microelectrodes allow for sampling from numerous sites/neurons to capture a detectable signal [27]. Further, the BSA fouling conditions shifted the LOD of 5-HT to higher concentrations for BDDMEs, which could suggest that the electroactive surface was blocked due to protein adsorption at the electrode face.

Several possible modifications to the electrode could enhance results, including increasing the electroactive surface area, and modification of the surface of the diamond. The Chestek group, in their CFME-parylene fabrication, utilized a pulsed green laser to remove and burn parylene-c insulation on carbon fiber electrodes to expose even tips with increased surface areas [58]. Similarly, a laser cutting system could be employed to selectively remove PCD, creating a cylinder-style electrode of all-diamond, exposing the conductive diamond core (**Figure 3.1E**) and increasing the surface area of the electrode. Furthermore, in this study, we identified potential parameter modifications that could be used to optimize results on the BDDME in accordance with previous literature [25]. Modifications to the switching and holding potentials in waveforms, such as in the extended Jackson waveform and extended hold serotonin waveform developed by the Venton group [29], could reduce fouling and improve BDDME sensitivity to 5-HT in future

studies. Similarly, experimentation with the "sawhorse" waveform devised by Kiethley et al. (2011) [59], with scan rates above 1000 V $s^{-1}$ to increase CFME sensitivity, could help tackle low sensitivity at BDDMEs. However, a more comprehensive report on the kinetics and processes controlling analyte detection at the BDDME surface may be necessary to solidify limitations of the electrode. For in vivo 5-HT detection, it may be crucial to assess a key downstream metabolite, 5-hydroxyindoleactic acid (5-HIAA), for presence and interference, along with biofouling effects on the 5-HT oxidative current at the BDDME. Pretreatment of the BDDME with cation exchange polymers (e.g., Nafion) could further reduce fouling and isolate 5-HT responses among interferents in the in vivo environment [27].

## 3.5 CONCLUSION

This study is the first account of FSCV waveform parameter investigation and in vitro biofouling performance of the freestanding BDDME for 5-HT detection. The results from this work can guide future improvements in electrode fabrication and electrochemical detection of 5-HT at the BDDME, particularly for chronic in vivo settings. Our BDDME is unique in its design as a discrete, microfabricated device with the potential to reduce fouling and have better long-term stability in vivo. The BDDME demonstrated greater stability and reduced fouling over changing switching potentials, waveform frequencies, and analyte concentrations. Furthermore, biofouling-induced effects on the peak anodic 5-HT current were less prominent at the BDDME, especially with the Jackson waveform, compared to the CFME. Meanwhile, the CFME displayed excellent LODs for 5-HT and maintained linear responses at lower ranges of concentration in the waveform as well as biofouling experiments. The BDDME suffers from issues of low sensitivity and a small geometric surface area that could present major challenges for in vivo detection of 5-HT. The

results from this work could guide modified electrode fabrication geometries and waveform strategies to optimize the performance of the BDDME as a chronic in vivo neurochemical sensor.

## 3.6 SUPPLEMENTARY MATERIALS

**A. Standard Waveform (triangular)**

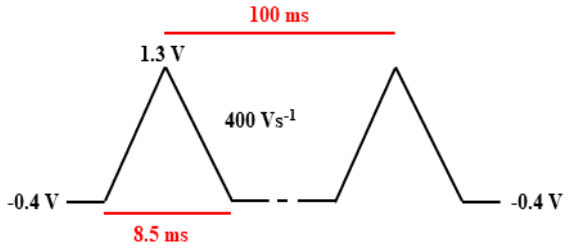


**B. Jackson Waveform (N-shaped)**

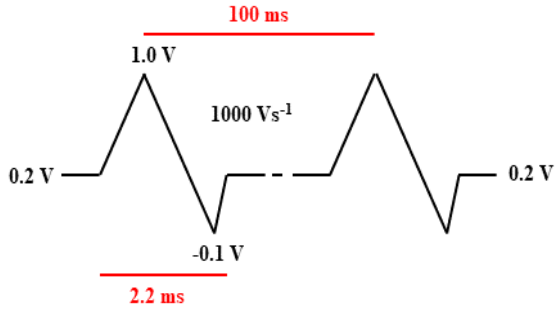


**Figure S3.1.** Diagrammatic view of standard and Jackson waveform. **A.** Standard waveform scans at 400 $Vs^{-1}$ while holding at a negative potential of -0.4 V, ramping up to 1.3 V and back down to -0.4 V in 8.5 ms. The waveform repeats at a frequency of 10 Hz. **B.** Jackson waveform begins at a positive potential of 0.2 V, sweeps up to 1.0 V and back down to -0.1V before returning to 0.2 V in 2.2 ms at 1000 $Vs^{-1}$ and 10 Hz.

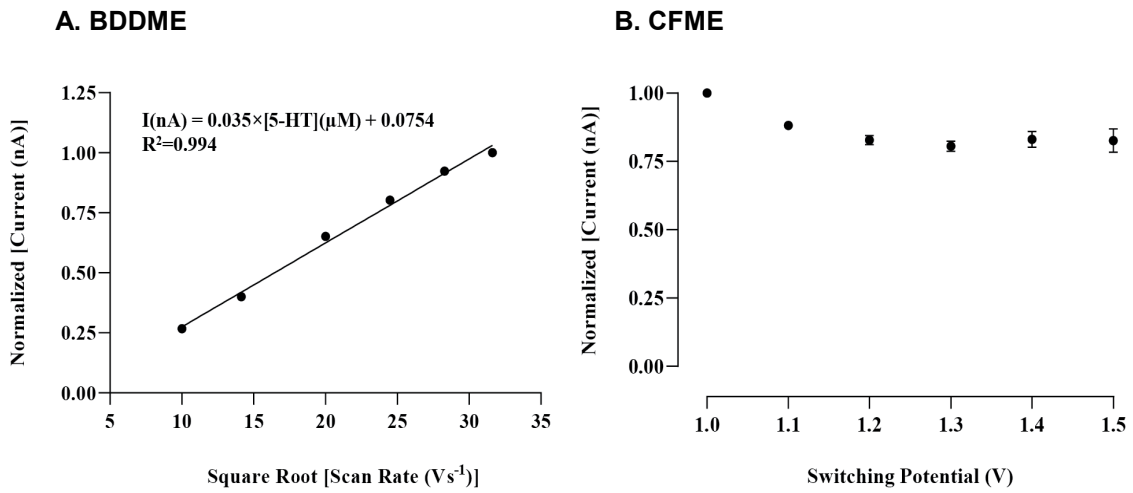


**Figure S3.2.** Further investigation of 5-HT oxidative response to scan rate at BDDMEs, and to increasing switching potential at inactivated CFMEs. **A.** 5-HT anodic peak response plotted against square root of scan rate to demonstrate possible diffusion-controlled kinetics at electrode surface, $R^2$=0.9939. **B.** Oxidative 5-HT responses at previously activated CFMEs with increasing switching potentials show a decreasing trend where 1.0 V has maximum response.

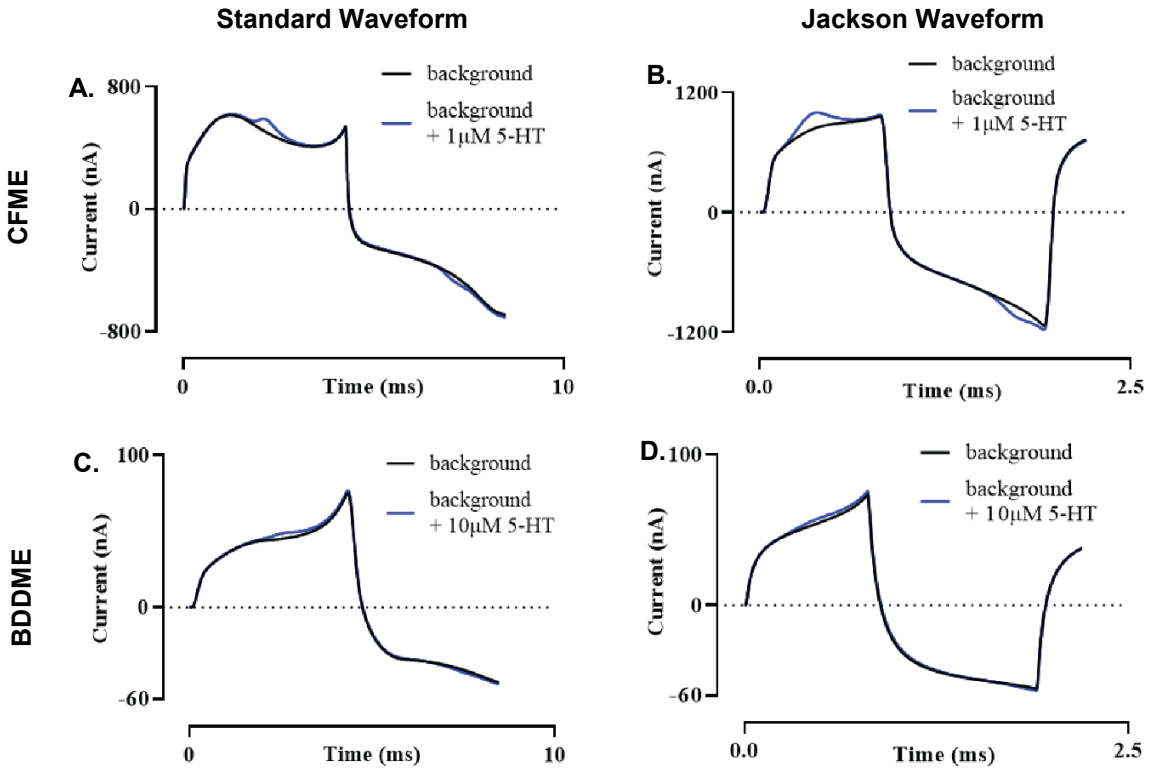


**Figure S3.3.** Background + faradaic currents at CFMEs and BDDMEs. **A. & B.** Faradaic current of 1 μM 5-HT current plotted over background current for CFME with standard and Jackson waveforms, respectively. **D. & C.** Faradaic current of 10 μM 5-HT plotted over background current for BDDME with standard and Jackson waveforms, respectively.

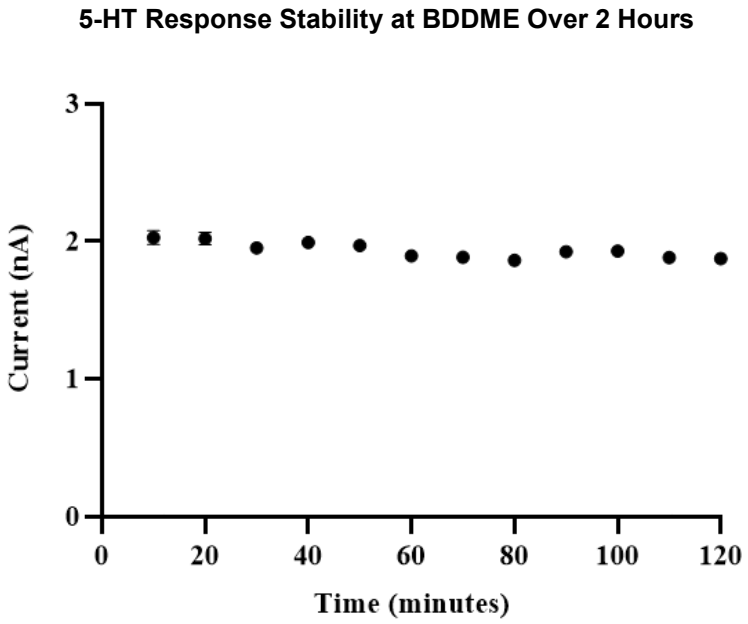


**Figure S3.4.** Response stability over 2 hours at the BDDME with the Jackson waveform. Current responses to injections of 10 µM 5-HT administered every 8-10 minutes for 120 mins (current variation < 10%). Data are represented as mean ± SEM for BDDME (*n*=1).

## REFERENCES


(1) Pereda, A.E.; Purpura, D.P. Electrical Synapses and Their Functional Interactions with Chemical Synapses. *Nat. Rev. Neurosci.* **2014**, *15*, 250–263. https://doi.org/10.1038/nrn3708.

(2) Jabeen, S.; Thirumalai, V. Neural Circuits: The Interplay between Electrical and Chemical Synaptogenesis. *J. Neurophysiol.* **2018**, *120*, 1914. https://doi.org/10.1152/JN.00398.2018.

(3) Bunin, M.A.; Prioleau, C.; Mailman, R.B.; Wightman, R.M. Release and Uptake Rates of 5-Hydroxytryptamine in the Dorsal Raphe and Substantia Nigra Reticulata of the Rat Brain. *J. Neurochem.* **2002**, *70*, 1077–1087. https://doi.org/10.1046/j.1471-4159.1998.70031077.x.

(4) Park, J.; Takmakov, P.; Wightman, R.M. In Vivo Comparison of Norepinephrine and Dopamine Release in Rat Brain by Simultaneous Measurements with Fast-Scan Cyclic Voltammetry. *J. Neurochem.* **2011**, *119*, 932–944. https://doi.org/10.1111/j.1471-4159.2011.07494.x.

(5) Samaranayake, S.; Abdalla, A.; Robke, R.; Wood, K.M.; Zeqja, A.; Hashemi, P. In Vivo Histamine Voltammetry in the Mouse Premammillary Nucleus. *Analyst* **2015**, *140*, 3759–3765. https://doi.org/10.1039/C5AN00313J.

(6) Borgus, J.R.; Wang, Y.; DiScenza, D.J.; Venton, B.J. Spontaneous Adenosine and Dopamine Cotransmission in the Caudate-Putamen Is Regulated by Adenosine Receptors. *ACS Chem. Neurosci.* **2021**, *12*, 4371–4379. https://doi.org/10.1021/acschemneuro.1c00175.

(7) Vickrey, T.L.; Condron, B.; Venton, B.J. Detection of Endogenous Dopamine Changes in *Drosophila melanogaster* Using Fast-Scan Cyclic Voltammetry. *Anal. Chem.* **2009**, *81*, 9306–9313. https://doi.org/10.1021/ac901638z.

(8) Makos, M.A.; Han, K.-A.; Heien, M.L.; Ewing, A.G. Using In Vivo Electrochemistry to Study the Physiological Effects of Cocaine and Other Stimulants on the *Drosophila melanogaster* Dopamine Transporter. *ACS Chem. Neurosci.* **2010**, *1*, 74–83. https://doi.org/10.1021/cn900017w.

(9) Shin, M.; Field, T.M.; Stucky, C.S.; Furgurson, M.N.; Johnson, M.A. Ex Vivo Measurement of Electrically Evoked Dopamine Release in Zebrafish Whole Brain. *ACS Chem. Neurosci.* **2017**, *8*, 1880–1888. https://doi.org/10.1021/acschemneuro.7b00022.

(10) Jones, L.J.; McCutcheon, J.E.; Young, A.M.J.; Norton, W.H.J. Neurochemical Measurements in the Zebrafish Brain. *Front. Behav. Neurosci.* **2015**, *9,* 246. https://doi.org/10.3389/fnbeh.2015.00246.

(11) Kennedy, R.T.; Jones, S.R.; Wightman, R.M. Simultaneous Measurement of Oxygen and Dopamine: Coupling of Oxygen Consumption and Neurotransmission. *Neuroscience* **1992**, *47*, 603–612. https://doi.org/10.1016/0306-4522(92)90169-3.

(12) Purcell, E.; Becker, M.; Guo, Y.; Hara, S.; Ludwig, K.; McKinney, C.; Monroe, E.; Rechenberg, R.; Rusinek, C.; Saxena, A.; et al. Next-Generation Diamond Electrodes for Neurochemical Sensing: Challenges and Opportunities. *Micromachines* **2021**, *12*, 128. https://doi.org/10.3390/mi12020128.

(13) Rusinek, C.A.; Guo, Y.; Rechenberg, R.; Becker, M.F.; Purcell, E.; Verber, M.; McKinney, C.; Li, W. All-Diamond Microfiber Electrodes for Neurochemical Analysis. *J. Electrochem. Soc.* **2018**, *165*, G3087–G3092. https://doi.org/10.1149/2.0141812jes.

(14) Suzuki, A.; Ivandini, T.A.; Yoshimi, K.; Fujishima, A.; Oyama, G.; Nakazato, T.; Hattori, N.; Kitazawa, S.; Einaga, Y. Fabrication, Characterization, and Application of Boron-Doped Diamond Microelectrodes for in Vivo Dopamine Detection. *Anal. Chem.* **2007**, *79*, 8608–8615. https://doi.org/10.1021/ac071519h.

(15) Ramsson, E.S.; Cholger, D.; Dionise, A.; Poirier, N.; Andrus, A.; Curtiss, R. Characterization of Fast-Scan Cyclic Voltammetric Electrodes Using Paraffin as an Effective Sealant with in Vitro and in Vivo Applications. *PLoS ONE* **2015**, *10*, e0141340. https://doi.org/10.1371/journal.pone.0141340.

(16) Huffman, M.L.; Venton, B.J. Carbon-Fiber Microelectrodes for in Vivo Applications. *Analyst* **2009**, *134*, 18–24. https://doi.org/10.1039/b807563h.

(17) Schulte, A.; Chow, R.H. A Simple Method for Insulating Carbon-Fiber Microelectrodes Using Anodic Electrophoretic Deposition of Paint. *Anal. Chem.* **1996**, *68*, 3054–3058. https://doi.org/10.1021/ac960210n.

(18) Dong, H.; Wang, S.; Galligan, J.J.; Swain, G.M. Boron-Doped Diamond Nano/Microelectrodes for Bio-Sensing and in Vitro Measurements. *Front. Biosci. (Sch. Ed.)* **2011**, *3*, 518. https://doi.org/10.2741/s169.

(19) Yence, M.; Cetinkaya, A.; Ozcelikay, G.; Kaya, S.I.; Ozkan, S.A. Boron-Doped Diamond Electrodes: Recent Developments and Advances in View of Electrochemical Drug Sensors. *Crit. Rev. Anal. Chem.* **2022**, *52*, 1122–1138. https://doi.org/10.1080/10408347.2020.1863769.

(20) Fan, B.; Rusinek, C.A.; Thompson, C.H.; Setien, M.; Guo, Y.; Rechenberg, R.; Gong, Y.; Weber, A.J.; Becker, M.F.; Purcell, E.; et al. Flexible, Diamond-Based Microelectrodes Fabricated Using the Diamond Growth Side for Neural Sensing. *Microsyst. Nanoeng.* **2020**, *6*, 42. https://doi.org/10.1038/s41378-020-0155-1.

(21) Puthongkham, P.; Venton, B.J. Recent Advances in Fast-Scan Cyclic Voltammetry. *Analyst* **2020**, *145*, 1087–1102. https://doi.org/10.1039/C9AN01925A.

(22) Bennet, K.E.; Tomshine, J.R.; Min, H.-K.; Manciu, F.S.; Marsh, M.P.; Paek, S.B.; Settell, M.L.; Nicolai, E.N.; Blaha, C.D.; Kouzani, A.Z.; et al. A Diamond-Based Electrode for Detection of Neurochemicals in the Human Brain. *Front. Hum. Neurosci.* **2016**, *10*, 102. https://doi.org/10.3389/fnhum.2016.00102.

(23) Bennett, J.A.; Wang, J.; Show, Y.; Swain, G.M. Effect of Sp[Sup 2]-Bonded Nondiamond Carbon Impurity on the Response of Boron-Doped Polycrystalline Diamond Thin-Film Electrodes. *J. Electrochem. Soc.* **2004**, *151*, E306. https://doi.org/10.1149/1.1780111/XML.

(24) Fischer, A.E.; Show, Y.; Swain, G.M. Electrochemical Performance of Diamond Thin-Film Electrodes from Different Commercial Sources. *Anal. Chem.* **2004**, *76*, 2553–2560. https://doi.org/10.1021/AC035214O.

(25) Venton, B.J.; Cao, Q. Fundamentals of Fast-Scan Cyclic Voltammetry for Dopamine Detection. *Analyst* **2020**, *145*, 1158. https://doi.org/10.1039/c9an01586h.

(26) Jackson, B.P.; Dietz, S.M.; Wightman, R.M. Fast-Scan Cyclic Voltammetry of 5-Hydroxytryptamine. *Anal. Chem.* **1995**, *67*, 1115–1120. https://doi.org/10.1021/ac00102a015.

(27) Hashemi, P.; Dankoski, E.C.; Petrovic, J.; Keithley, R.B.; Wightman, R.M. Voltammetric Detection of 5-Hydroxytryptamine Release in the Rat Brain. *Anal. Chem.* **2009**, *81*, 9462–9471. https://doi.org/10.1021/AC9018846.

(28) Heien, M.L.A.V.; Phillips, P.E.M.; Stuber, G.D.; Seipel, A.T.; Wightman, R.M. Overoxidation of Carbon-Fiber Microelectrodes Enhances Dopamine Adsorption and Increases Sensitivity. *Analyst* **2003**, *128*, 1413–1419. https://doi.org/10.1039/B307024G.

(29) Dunham, K.E.; Venton, B.J. Improving Serotonin Fast-Scan Cyclic Voltammetry Detection: New Waveforms to Reduce Electrode Fouling. *Analyst* **2020**, *145*, 7437–7446. https://doi.org/10.1039/D0AN01406K.

(30) Takmakov, P.; Zachek, M.K.; Keithley, R.B.; Walsh, P.L.; Donley, C.; McCarty, G.S.; Wightman, R.M. Carbon Microelectrodes with a Renewable Surface. *Anal. Chem.* **2010**, *82*, 2020–2028. https://doi.org/10.1021/ac902753x.

(31) Gonon, F.G.; Fombarlet, C.M.; Buda, M.J.; Pujol, J.F. Electrochemical Treatment of Pyrolytic Carbon Fiber Electrodes. *Anal. Chem.* **1981**, *53*, 1386–1389. https://doi.org/10.1021/AC00232A020/ASSET/AC00232A020.FP.PNG_V03.

(32) Salatino, J.W.; Ludwig, K.A.; Kozai, T.D.Y.; Purcell, E.K. Glial Responses to Implanted Electrodes in the Brain. *Nat. Biomed. Eng.* **2017**, *1*, 862–877. https://doi.org/10.1038/S41551-017-0154-1.

(33) Polikov, V.S.; Tresco, P.A.; Reichert, W.M. Response of Brain Tissue to Chronically Implanted Neural Electrodes. *J. Neurosci. Methods* **2005**, *148*, 1–18. https://doi.org/10.1016/j.jneumeth.2005.08.015.

(34) Seaton, B.T.; Hill, D.F.; Cowen, S.L.; Heien, M.L. Mitigating the Effects of Electrode Biofouling-Induced Impedance for Improved Long-Term Electrochemical Measurements In Vivo. *Anal. Chem.* **2020**, *92*, 6334–6340. https://doi.org/10.1021/acs.analchem.9b05194.

(35) Wisniewski, N.; Moussy, F.; Reichert, W.M. Characterization of Implantable Biosensor Membrane Biofouling. *Fresenius J. Anal. Chem.* **2000**, *366*, 611–621. https://doi.org/10.1007/s002160051556.

(36) Kuhlmann, J.; Dzugan, L.C.; Heineman, W.R. Comparison of the Effects of Biofouling on Voltammetric and Potentiometric Measurements. *Electroanalysis* **2012**, *24*, 1732–1738. https://doi.org/10.1002/elan.201200194.

(37) Patel, B.A.; Bian, X.; Quaiserová-Mocko, V.; Galligan, J.J.; Swain, G.M. In Vitro Continuous Amperometric Monitoring of 5-Hydroxytryptamine Release from Enterochromaffin Cells of the Guinea Pig Ileum. *Analyst* **2007**, *132*, 41–47. https://doi.org/10.1039/B611920D.

(38) Singh, Y.S.; Sawarynski, L.E.; Michael, H.M.; Ferrell, R.E.; Murphey-Corb, M.A.; Swain, G.M.; Patel, B.A.; Andrews, A.M. Boron-Doped Diamond Microelectrodes Reveal Reduced Serotonin Uptake Rates in Lymphocytes from Adult Rhesus Monkeys Carrying the Short Allele of the 5-HTTLPR. *ACS Chem. Neurosci.* **2010**, *1*, 49–64. https://doi.org/10.1021/cn900012y.

(39) Gupta, B.; Perillo, M.L.; Christensen, I.E.; Siegenthaler, J.R.; Rochenberg, R.; Becker, M.F.; Li, W.; Purcell, E.K. Waveform Development for Neurotransmitter Detection on Novel Boron-Doped Diamond Microelectrodes. In Proceedings of the 11th International IEEE Engineering in Medicine & Biology Society (EMBS) Conference on Neural Engineering, Baltimore, MD, USA, 25–27 April 2023.

(40) Bucher, E.S.; Brooks, K.; Verber, M.D.; Keithley, R.B.; Owesson-White, C.; Carroll, S.; Takmakov, P.; McKinney, C.J.; Wightman, R.M. Flexible Software Platform for Fast-Scan Cyclic Voltammetry Data Acquisition and Analysis. *Anal. Chem.* **2013**, *85*, 10344–10353.

(41) Singh, Y.S.; Sawarynski, L.E.; Dabiri, P.D.; Choi, W.R.; Andrews, A.M. Head-to-Head Comparisons of Carbon Fiber Microelectrode Coatings for Sensitive and Selective Neurotransmitter Detection by Voltammetry. *Anal. Chem.* **2011**, *83*, 6658. https://doi.org/10.1021/AC2011729.

(42) Boschen, S.L.; Trevathan, J.; Hara, S.A.; Asp, A.; Lujan, J.L. Defining a Path Toward the Use of Fast-Scan Cyclic Voltammetry in Human Studies. *Front. Neurosci.* **2021**, *15,* 1548. https://doi.org/10.3389/FNINS.2021.728092.

(43) Siegenthaler, J.; Gushiken, B.; Hill, D.; Cowen, S.; Heien, M. Moving Fast-Scan Cyclic Voltammetry toward FDA Compliance with Capacitive Decoupling Patient Protection. *ACS Sens.* **2020**, *5*, 1890–1899. https://doi.org/10.1021/acssensors.9b02249.

(44) Bucher, E.S.; Wightman, R.M. Electrochemical Analysis of Neurotransmitters. *Annu. Rev. Anal. Chem.* **2015**, *8*, 239–261. https://doi.org/10.1146/ANNUREV-ANCHEM-071114-040426.

(45) Jarosova, R.; Douglass, A.D.; Johnson, M.A. Optimized Sawhorse Waveform for the Measurement of Oxytocin Release in Zebrafish. *Anal. Chem.* **2022**, *94*, 2942–2949. https://doi.org/10.1021/acs.analchem.1c04879.

(46) Ross, A.E.; Venton, B.J. Sawhorse Waveform Voltammetry for Selective Detection of Adenosine, ATP, and Hydrogen Peroxide. *Anal. Chem.* **2014**, *86*, 7486–7493. https://doi.org/10.1021/AC501229C/SUPPL_FILE/AC501229C_SI_001.PDF.

(47) Shao, Z.; Jill, B.; Zestos, A.G.; Wonnenberg, P.M.; George, A. Review—Recent Advances in FSCV Detection of Neurochemicals via Waveform and Carbon Microelectrode Modification. *J. Electrochem. Soc.* **2021**, *168*, 057520. https://doi.org/10.1149/1945-7111/AC0064.

(48) Bath, B.D.; Michael, D.J.; Trafton, B.J.; Joseph, J.D.; Runnels, P.L.; Wightman, R.M. Subsecond Adsorption and Desorption of Dopamine at Carbon-Fiber Microelectrodes. *Anal. Chem.* **2000**, *72*, 5994–6002. https://doi.org/10.1021/ac000849y.

(49) Baluchová, S.; Mamaloukou, A.; Koldenhof, R.H.J.M.; Buijnsters, J.G. Modification-Free Boron-Doped Diamond as a Sensing Material for Direct and Reliable Detection of the Antiretroviral Drug Nevirapine. *Electrochim. Acta* **2023**, *450*, 142238. https://doi.org/10.1016/J.ELECTACTA.2023.142238.

(50) Tyszczuk-Rotko, K.; Jaworska, I.; Jędruchniewicz, K. Application of Unmodified Boron-Doped Diamond Electrode for Determination of Dopamine and Paracetamol. *Microchem. J.* **2019**, *146*, 664–672. https://doi.org/10.1016/J.MICROC.2019.01.064.

(51) Teófilo, R.F.; Ceragioli, H.J.; Peterlevitz, A.C.; Da Silva, L.M.; Damos, F.S.; Ferreira, M.M.C.; Baranauskas, V.; Kubota, L.T. Improvement of the Electrochemical Properties of "as-Grown" Boron-Doped Polycrystalline Diamond Electrodes Deposited on Tungsten Wires Using Ethanol. *J. Solid State Electrochem.* **2007**, *11*, 1449–1457. https://doi.org/10.1007/S10008-007-0319-Z/TABLES/2.

(52) Szeitz, A.; Bandiera, S.M. Analysis and Measurement of Serotonin. *Biomed. Chromatogr.* **2018**, *32*, e4135. https://doi.org/10.1002/BMC.4135.

(53) Rodeberg, N.T.; Sandberg, S.G.; Johnson, J.A.; Phillips, P.E.M.; Wightman, R.M. Hitchhiker's Guide to Voltammetry: Acute and Chronic Electrodes for in Vivo Fast-Scan Cyclic Voltammetry. *ACS Chem. Neurosci.* **2017**, *8*, 221–234. https://doi.org/10.1021/acschemneuro.6b00393.

(54) Rao, T.N.; Yagi, I.; Miwa, T.; Tryk, D.A.; Fujishima, A. Electrochemical Oxidation of NADH at Highly Boron-Doped Diamond Electrodes. *Anal. Chem.* **1999**, *71*, 2506–2511. https://doi.org/10.1021/AC981376M.

(55) Hanssen, B.L.; Siraj, S.; Wong, D.K.Y. Recent Strategies to Minimise Fouling in Electrochemical Detection Systems. *Rev. Anal. Chem.* **2016**, *35*, 1–28. https://doi.org/10.1515/revac-2015-0008.

(56) Wisniewski, N.; Reichert, M. Methods for Reducing Biosensor Membrane Biofouling. *Colloids Surf. B Biointerfaces* **2000**, *18*, 197–219. https://doi.org/10.1016/S0927-7765(99)00148-4.

(57) Hersey, M.; Samaranayake, S.; Berger, S.N.; Tavakoli, N.; Mena, S.; Nijhout, H.F.; Reed, M.C.; Best, J.; Blakely, R.D.; Reagan, L.P.; et al. Inflammation-Induced Histamine Impairs the Capacity of Escitalopram to Increase Hippocampal Extracellular Serotonin. *J. Neurosci.* **2021**, *41*, 6564–6577. https://doi.org/10.1523/JNEUROSCI.2618-20.2021.

(58) Welle, E.J.; Patel, P.R.; Woods, J.E.; Petrossians, A.; della Valle, E.; Vega-Medina, A.; Richie, J.M.; Cai, D.; Weiland, J.D.; Chestek, C.A. Ultra-Small Carbon Fiber Electrode Recording Site Optimization and Improved in Vivo Chronic Recording Yield. *J. Neural. Eng.* **2020**, *17*, 026037. https://doi.org/10.1088/1741-2552/AB8343.

(59) Keithley, R.B.; Takmakov, P.; Bucher, E.S.; Belle, A.M.; Owesson-White, C.A.; Park, J.; Wightman, R.M. Higher Sensitivity Dopamine Measurements with Faster-Scan Cyclic Voltammetry. *Anal. Chem.* **2011**, *83*, 3563–3571. https://doi.org/10.1021/ac200143v.

# CHAPTER 4 | SPATIAL TRANSCRIPTOMICS TO IDENTIFY NOVEL BIOMARKERS AT THE BRAIN-ELCTRODE INTERFACE

## 4.1 INTRODUCTION

Implantable electrode arrays in the brain are increasingly used in research and clinical settings to study and treat a variety of neurological conditions[1–7]. Such treatments can rely on the detection of stable signals to guide neuromodulation, brain computer interfaces (BCIs) or other assistive technology. Electrophysiological recordings using implantable electrodes have previously revealed a trend in signal decline over weeks and months following implantation[8–11]. Additional undesirable effects including insertional trauma, shifting stimulation thresholds, and off-target consequences have been observed across such long-term studies. Deeper investigations of the device-tissue interface are needed to better under the chronic foreign-body tissue response to implanted electrode arrays, justifying the use of newer and more sophisticated techniques[12–16].

Conventional histology is routinely employed to assess neuronal density and astrocytic expression of glial fibrillary acidic protein (GFAP) to characterize the biological response and tissue health post device implantation[17]. Yet, traditional histology is relatively low throughput due to the pre-selection of a few biomarkers at a time to provide limited information on the biological mechanisms affecting signal quality[18]. The use of high throughput RNA-sequencing and spatial transcriptomics techniques to map transcriptional changes in cells surrounding devices[19] can reveal novel information about both recording and stimulating electrodes[20–23].

Initial work employing silicon microelectrodes by Thompson et al. using laser capture microscopy extracted interfacial (≤100 μm from device site) and distal tissue (~500 μm from device site) samples for RNA-sequencing, presenting hundreds of differentially expressed genes

(DEGs) when comparing tissue close to implanted electrodes relative to non-implanted naïve tissues[23]. Certain DEGs, distinguished according to known cellular and molecular mechanisms, were significantly upregulated or downregulated across timepoints (24 hours, 1 week, and 6 weeks) such as reactive microglia/inflammation *(*e,g*., Gpnmb, Cx3cr1*, *Tnfrsf1a*, *C3*), oligodendrocyte metabolism and myelin maintenance (e.g., *Olig2*, *Plp1*, *Tf, Mbp*, *Cnp, Fth1*), neuronal function and plasticity (e.g., *Nefh, Camk2a*, *Snap25, Arc*), astrocyte activation and fibrosis (e.g., *Gfap, Aqp4, Vim, Ptbp1 Best1*), lysosomal activity (*Ctss, Ctsb*), proliferation (*Csf1r*), and phagocytosis (*Dock8*). These RNA-seq results, along with others[24–27], support that cellular and molecular changes (as gene expression differences) are involved in the biological environment around implanted electrodes in the brain. For example, high expression of inflammatory and phagocytic genes via reactive microglia extended out to 6-weeks post-implantation, reinforcing the knowledge of neurotoxic mechanisms. A steady upregulation in oligodendrocyte genes associated with cellular identity, iron metabolism, and myelination[28–30] possibly suggests a demand for metabolically taxing remyelination and oligodendrocyte turnover at the device interface. Decreased regulation of neuronal genes related with synaptic function and dendritic spine maintenance potentially verify neuron damage/dysfunction-associated roles contributing to reduced signal quality[31].

Newer spatial transcriptomics methods offering whole-tissue section mapping of gene expression levels can further extend these initial findings[21]. Whitsitt et al. (2021) implanted nonfunctional, single shank, silicon microelectrode arrays in rat motor cortices for 24-hours ($n$ = 1 rat), 1-week ($n$ = 1 rat) and 6-week ($n$ = 1 rat) timepoints post-implantation[21]. The spatial transcriptomics assay (10x Genomics, Visium) enabled fresh frozen tissue to be mounted on microscope slides containing capture sites of spatially barcoded, RNA-binding oligonucleotides.

Sections were immunostained for neuronal nuclei (NeuN) and GFAP, and imaged prior to tissue permeabilization, cDNA synthesis, RNA sequencing and analysis. Each time point presented thousands of significant DEGs in comparisons of either implanted versus unimplanted tissue sections (24-hour timepoint), and areas near (≤ 150 μm) versus far (≥ 500 μm) from the device tract (1-week and 6-week timepoints). A unique observation was that previously reported DEGs extended over a large area of the tissue landscape, over 3.0 mm from the injury site, at 24-hours. Gene expression became consolidated by 6-weeks, indicating a progression from an acute to chronic foreign body tissue response. Interestingly, the device-reactive astrocytes expressed similar genes to the glia limitans, indicating widespread activation of astrocytes across cortex. Overall, spatial transcriptomics of the whole device-tissue interface at each time point revealed significant DEGs that could be further analyzed to uncover prominent biological processes at play.

In this work, we extend the RNA-sequencing results reported previously by conducting spatial transcriptomics on a larger dataset ($n$ = 10 rats, 5 rats per time point) of rats implanted with silicon microelectrode arrays for 1-week and 6-week. Differential gene expression analysis revealed that: (1) more genes are upregulated near the device at 6-weeks than previously thought while maintaining consolidated expression patterns surrounding the device compared to 1-week animals, and (2) certain groups of genes, such as apoptosis-related and chemokine signaling genes, are more prominent near the device site at 6-weeks compared to 1-week samples. Further, electrophysiological recordings were collected from functional devices implanted in $n$ = 7 rats up to 6 weeks. The datasets collected here can be used in further downstream computational network analyses targeted to reveal biomarkers of interest at the electrode-tissue interface.

## 4.2 METHODS AND MATERIALS

### 4.2.1 SURGICAL IMPLANTATION, BRAIN EXTRACTION AND TISSUE SECTIONING

Previously published methods were followed for surgical implantation of devices and brain extraction[21,32]. Briefly, single-shank, planar silicon Michigan-style microelectrode arrays (A1×16-3 mm-100-703-CMLP, 15 µm thickness, NeuroNexus Inc, Ann Arbor, MI) were implanted in the motor cortices of adult, male Sprague Dawley rats (~12 weeks old). Rats were anaesthetized under isoflurane (~2.0 % in oxygen) and devices were stereotaxically lowered in the M1 region of motor cortices (+3.0 mm AP, +2.5 mm ML from Bregma, and 2.0 mm deep from cortex). Functional devices, capable of recording electrophysiological activity, were grounded by wrapping exposed stainless-steel wires around the bone screws. A head cap of dental acrylic was made to close the surgical site and secure the device in place. Meloxicam (2 mg/kg, subcutaneously) and bupivacaine (topically) were administered as post-operative analgesics. Rats were implanted for 1-week (total $n$ = 5 rats) and 6-week ($n$ = 7 rats) time points. Non-functional devices were implanted in $n$ = 4 rats ($n$ = 1 rat for 1-week time point, $n$ = 3 rats for 6-week time point), and functional devices were implanted in $n$ = 8 rats ($n$ = 4 rats for 1-week time point, $n$ = 4 rats for 6-week time point). At the terminal timepoint, rats were euthanized by an overdose intraperitoneal delivery of sodium pentobarbital. Cardiac perfusions with 100 mL of sterile Dulbecco's Phosphate Buffered Saline (Sigma-Aldrich, D8537-100ML) were carried out post euthanasia, and brains were rapidly extracted after decapitation. Brains were cryo-embedded immediately after removal in a chamber containing dry ice. Brain tissue was cryosectioned at a depth ~1000 µm from the cortical surface. One tissue section of the implanted hemisphere from each animal was mounted in the designated capture area of the Visium Spatial Gene Expression slide (10x Genomics, Pleasanton CA). Each tissue section was trimmed prior to mounting to fit within the fiducial frame boundaries of the

Visium capture areas. All animal procedures were approved by the Michigan State University Animal Care and Use Committee.

### 4.2.2 IMMUNOHISTOCHEMISTRY (IHC) AND SPATIAL TRANSCRIPTOMICS WORKFLOW

The spatial transcriptomics assay, along with IHC, was followed based on the vendor protocol (10x Genomics), and as reported previously. Briefly, the spatial gene expression platform by 10x Genomics offers a Visium Spatial Gene Expression slide containing four capture areas (6.5 × 6.5 mm) marked by fluorescent fiducial frames. Each capture area further consists of ~5000 spatially barcoded oligonucleotides, organized as spots (each with a 55 μm diameter) placed 100 μm apart (center-to-center), to capture mRNA from mounted tissue.

In the workflow, immunohistochemistry and imaging is performed prior to sequencing in order to overlay the ST data on immunostained wide-field images. Tissue sections placed on the Visium Spatial Gene Expression slide were fixed in chilled methanol (at -20° Celsius) and blocked with Bovine Serum Albumin (BSA). Tissue was immunostained for GFAP primary antibody (Mouse Monoclonal GFAP antibody, 1:400, Millipore Sigma, St. Loius, Mo, Cat. #: A11034) and neuronal nuclei (NeuN) primary antibody (rabbit Polyclonal NeuN antibody, 1:100, Abcam, Cambridge, MA, Cat. #: 104225). Secondary antibodies of AlexaFluor 647 (Anti-mouse IgG, Invitrogen, Eugene, OR Cat. #: A21235) for conjugation to GFAP primary, and AlexaFluor 488 (Anti-rabbit IgG, Invitrogen, Eugene, OR, Cat. #: A11034) for conjugation for NeuN primary were used. A counterstain of Hoechst 33342 (1:10000, Life Technologies Corp, Eugene, OR, Cat. #: H3570) was employed to label all nuclei. After staining, the Visium slide was cover slipped as per the protocol, and tissue imaging was conducted at the Michigan State University Center for Advanced Microscopy. A Leica Stellaris 5 CLSM confocal microscope with a motorized

headstage was employed to image individual tiles (10x magnification) of each capture area containing tissue. A final wide-field image was generated by reconstructing, or stitching, the individual image tiles via the automated Leica software.

After imaging, the coverslip on the Visium Spatial Gene Expression slide was removed, and subsequent steps for tissue permeabilization and complementary DNA (cDNA) synthesis were performed. Briefly, tissue sections on the Visium slide were enzymatically permeabilized to release and capture the poly-adenylated mRNA of cells overlying the spots (containing barcoded oligonucleotides) in the capture areas. The optimal permeabilization time was determined in a prior experiment as 18 minutes. Next, reagents for reverse transcription were added to the slide to extend the capture oligo based on the bound mRNA sequence. A series of template switching and second strand synthesis then produced a spatially barcoded, full-length cDNA from the captured mRNA. This was followed by denaturation and cDNA transfer from each capture area into a corresponding DNA/RNA LoBind microcentrifuge tube, producing 4 sample tubes for each capture area containing tissue. A small amount (~1 uL) of the cDNA from each sample was transferred to a quantitative PCR (qPCR) plate for amplification. Based on the qPCR amplification plot, a quantification cycle (Cq) value was recorded for each sample at ~25% of the peak fluorescence value. The Cq value determined the number of cycles needed for further cDNA amplification of the samples, ensuring adequate mass for library construction. After amplification, the cDNA was cleaned up using SPRIselect (Beckman Coulter Inc, Brea, CA), and samples were transferred to new microcentrifuge tubes for library construction and sequencing.

### 4.2.3 RNA SEQUENCING AND DIFFERENTIAL EXPRESSION

Samples containing cleaned cDNA were delivered to the University of Michigan Advanced Genomics core for library preparation and sequencing. Assessment of cDNA quality was carried

out using the Tapestation 2200 (Agilent) device. Based on the vendor protocol (10x Genomics), cDNA was prepared into a library for subsequent sequencing. The LabChip GX (PerkinElmer) was used for assessment of the prepared libraries. The final libraries were pooled, and paired-end sequencing was performed using the Illumina NovaSeq 6000 system. Raw sequencing data were converted into de-multiplexed Fastq files with the Bcl2fastq2 Conversion Software. Lastly, the SpaceRanger pipeline (10x Genomics) was employed to align the sequencing reads to a reference genome and produce count matrices that were used to quantify the number of reads related to each gene. The AGGR function in SpaceRanger (10x Genomics) was employed to aggregate the dataset presented in this work.

The sequenced data were made available in .cloupe files, accessible by the 10x Genomics software "Loupe Browser", and raw .fastq files. The .cloupe files can combine spatial-barcodes in the sequencing data with the wide-field immunostained image (.tif) of a capture area (**Figure 4.1**) for a visual representation of gene expression on a stained tissue section. This is facilitated by the fiducial frame (visible on the red channel, 594 nm, while imaging) that defines a capture area, matching the sequencing reads to their corresponding location on the Visium slide. Once a .cloupe file is loaded in Loupe Browser, the gene expression (overlaid on IHC images) can be analyzed by selecting clusters of spots manually. The gene expression levels between clusters can be compared to generate lists of differentially expressed genes (DEGs) demonstrating upregulation and/or downregulation of detected genes, i.e. differential expression analysis. These DEG lists generated by LoupeBrowser contain values with the $Log_2$Fold Change (LFC), and a *p*-value, adjusted using the Benjamin-Hochberg correction for multiple values, for each gene. The software also uses a correction factor for differences in number of spots selected in comparisons[33]. The LFC is a ratio of normalized mean gene Unique Molecular Identifier (UMI) counts in a cluster relative to other

selected clusters. It is important to note that RNA sequencing identifies counts of gene transcripts in each spot of the capture area in a Visium slide, and these reads (tagged with a spatial barcode) also have a UMI that identify individual molecules of RNA, ensuring that each count can be matched to its original molecule. A single count contributing to the differential expression analysis must have a UMI, spatial barcode and gene annotation (recognizing which gene that RNA molecule belongs to). Differential expression analysis of genes and representative spatial gene expression images reported in this work were generated by loading an aggregated dataset in the Loupe Browser software by 10x Genomics.

Volcano plots to visualize DEGs were created using GraphPad Prism 10.4.1. DEGs with LFC $\geq 0.6$ or $\leq -0.6$, and adjusted p-value $< 0.05$ were considered significant. The p-value was transformed to $-\log_{10}$(p-value) following convention for better visualization of the data. The volcano plot x-axis was plotted to contain the LFC, and y-axis was plotted with adjusted p-values. Significance thresholds are indicated by dotted lines, and significant DEGs are highlighted in red in the volcano plots.

### 4.2.4 ELECTROPHYSIOLOGY

Electrophysiological data collection and analysis of recordings were conducted based on previously published methods[34]. Briefly, electrophysiological recordings were taken post-implantation at 24hrs, 1 week and weekly thereafter until the terminal time point immediately before euthanasia. A RZ2 BioAmp Processor (Tucker-Davis Technologies, Alachua, FL) was connected to the 16-channel planar Michigan-style electrodes at the time of recordings to collect extracellular spiking activity. Rats were lightly anesthetized (~1%) during the interval of the recording session and placed inside of a grounded faraday cage to minimize noise interference.

Wideband data was collected at ~48 kHz over short intervals (~5 minutes) for each recording session.

Data processing was done offline using Matlab, as reported previously, to extract average amplitudes of multiunit activity (MUA) and local field potential (LFP) across the 16 channels of the implant for each time point per animal. MUA was calculated using the algorithm described in the report by Whitsitt et al. (2024) with minor modifications[34]. To minimize correlated noise effects, the common average reference (CAR) was calculated and subtracted from each recording[35]. A band-pass filter at 500-6000 Hz was then applied to the CAR-subtracted signals. For each sample outside the bounds of ±3.5 × standard deviations (STD), a 2.4 ms window was extracted after centering to the absolute minimum of the signal. The remaining data was excluded as noise. The root mean square (RMS) value of the noise floor across 16 sites on the array was evaluated to detect and exclude data from potentially damaged recording sites[34,35]. From the stored signal snippets, the peak-to-peak value generated from the average of the positive deflections (samples > 3.5 × STD) and negative deflections (samples < -3.5 × STD) was calculated to generate the mean MUA amplitude of a given recording site. These values were further averaged across all viable channels to calculate the overall average MUA amplitude collected by the implanted electrode. For LFP signals, a 60 Hz notch filter was applied to the raw data from each channel to eliminate residual 60 Hz noise, followed by band pass filtering at 1-300 Hz. The LFP amplitude for each channel was calculated as 6 times the STD of the filtered data and averaged across the channels to generate a mean LFP amplitude per implanted device.

For each time point (1-week or 6-week), average MUA and average LFP amplitude values were generated per recording day for each animal. For example, a 1-week animal underwent two recording sessions (at 24 hr post-implantation, and at 1 week or terminal point), generating average

MUA and average LFP values at each session. The mean of average MUA and average LFP for each time point (day) across animals ($n$ = 7 rats) was plotted as the final average MUA and LFP in amplitude vs time plots to demonstrate chronic signal recordings. Recordings from $n$ = 1 rat for 6 weeks, were excluded from the dataset due to high noise and outlier effects.

## 4.3 RESULTS AND DISCUSSION

### 4.3.1 ELECTROPHYSIOLOGICAL RECORDINGS

Signal variability and quality decline in chronic recordings with implanted electrodes have been reported previously by our lab and other research groups[34,36]. In this work, functional silicon Michigan probes were implanted in a subset of rat brains (total functional electrophysiology implants $n$ = 7 rats: $n$ = 4 rats implanted for 1 week, and $n$ = 3 rats implanted for up to 6 weeks) that were extracted for spatial transcriptomics. **Figure 4.1** demonstrates chronic electrophysiological recordings as average LFP and MUA amplitudes from implanted rats over 42 days, or 6 weeks. A general decline in LFP and MUA amplitudes is observed over the recording time course, with a slight rise (or "signal rebound") in LFP signal amplitude at the ~ 1-week time point, followed by a gradual decrease over subsequent weeks. The signal rebound is also reflected in the MUA amplitude during the first two weeks, accompanied by a somewhat quick decrease and steadying of the signal over the remaining weeks. This signal rebound potentially arises from the tissue response to initial device insertion and injury, such as blood-brain-barrier (BBB) breach and protein adsorption. It has been reported that microglia and early-responder cells migrate towards the device within minutes post-implantation, suggesting that cellular activity around the implant is increased within the acute phase of the foreign body response. This additional cellular

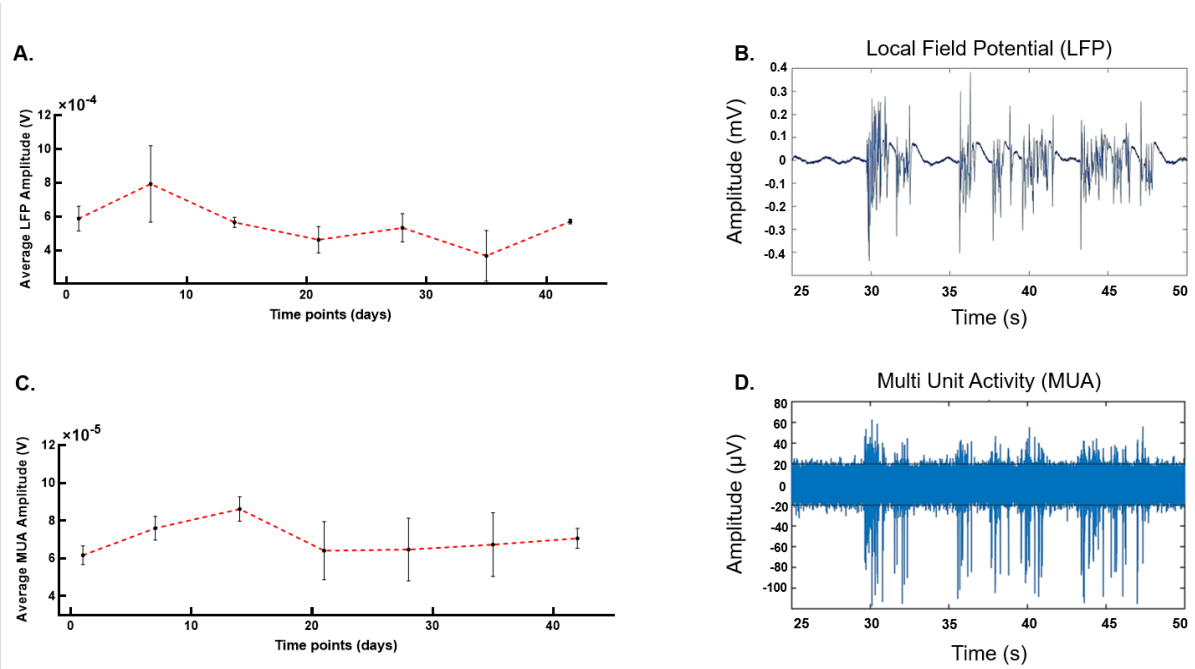


**Figure 4.1.** Chronic electrophysiological recordings taken from rat motor cortices implanted with silicon Michigan probes over 6 weeks. **A, C**. Average LFP amplitudes and MUA amplitudes, respectively, recorded weekly from each rat post-implantation. Data recordings shown here were included from $n = 4$ rats implanted for 1 week, and $n = 3$ rats implanted for 6 weeks. Error bars indicate standard error of mean recordings among animals. **B, D.** Representative signal snippets of LFP, and extracted MUA recordings over 25 seconds for a 6-week rat, taken 24 hours post implantation. Electrophysiological recordings were taken at 24 hours, and weekly post-implantation up till terminal time point (1 week or 6 week) from each animal.

activity could potentially contribute to the overall LFP signal and MUA amplitude recorded during the early weeks post-implantation.

As the tissue response transitions into the chronic phase, functional and structural changes of cells in the local region surrounding implanted electrodes have been reported[31]. Seminal works have shown that neuronal population and density is decreased around chronically implanted devices over time[17]. As the tissue stabilizes and facilitates glial encapsulation of the electrode[14], extracellular sources contributing to the signals detected by the implanted device may be decreased, resulting in the general signal decay observed in the recordings shown in **Figure 4.1A and B**. Errors bars at each data point represent variability in individual electrode performance, yet

the decreasing trend in signal recording quality is maintained across implanted animals supporting that other cellular and molecular factors affecting device longevity are at play in the biological environment.

### 4.3.2 IHC AND SPATIAL TRANSCRIPTOMICS OF THE ELECTRODE-INTERFACE OF THE PRIMARY MOTOR CORTEX

In 2021, Whitsitt et al. reported the first spatial transcriptomics study of the device-tissue interface with a limited sample size containing $n = 3$ rats, one for each time point of 24-hours, 1-week and 6-weeks post-implantation. Yet, comparisons between implanted and non-implanted, naïve tissue sections had presented 5811 DEGs at 24-hours, 2422 DEGs at 1-week and 513 DEGs at 6-weeks post-implantation. Further significant DEGs ($p$ value $< 0.05$) were found when comparing regions near ($\leq 150$ μm) and far ($\geq 500$ μm) from device injury site within 1-week (1056 DEGs) and 6-week samples (163 DEGs). The current study extends the findings of these preliminary results and reports an assessment of DEGs in multiple tissue sections implanted for 1-week ($n = 5$ rats) and 6-weeks ($n = 5$ rats). An immediate observation in the 2021 report, due to the high spatial resolution of this RNA-sequencing method, was that the spatial expression pattern of DEGs at the 24-hour time point extends past 500 μm and up to the edge of the tissue section for many genes. A within tissue comparison of genes in the 24-hour sample was not conducted in the 2021 study for this reason, and this time point was excluded from the current work for similar reasons: the differential expression of genes at the 24-hour timepoint seems to be overwhelmed by initial device insertion and immediate damage response extending over the entire tissue section. To present reliable comparisons between the acute phase and chronic phase of the foreign body response to implanted devices, this study proceeds with an investigation of DEGs at the 1-week and 6-week timepoints from tissue sections extracted from a larger sample size.

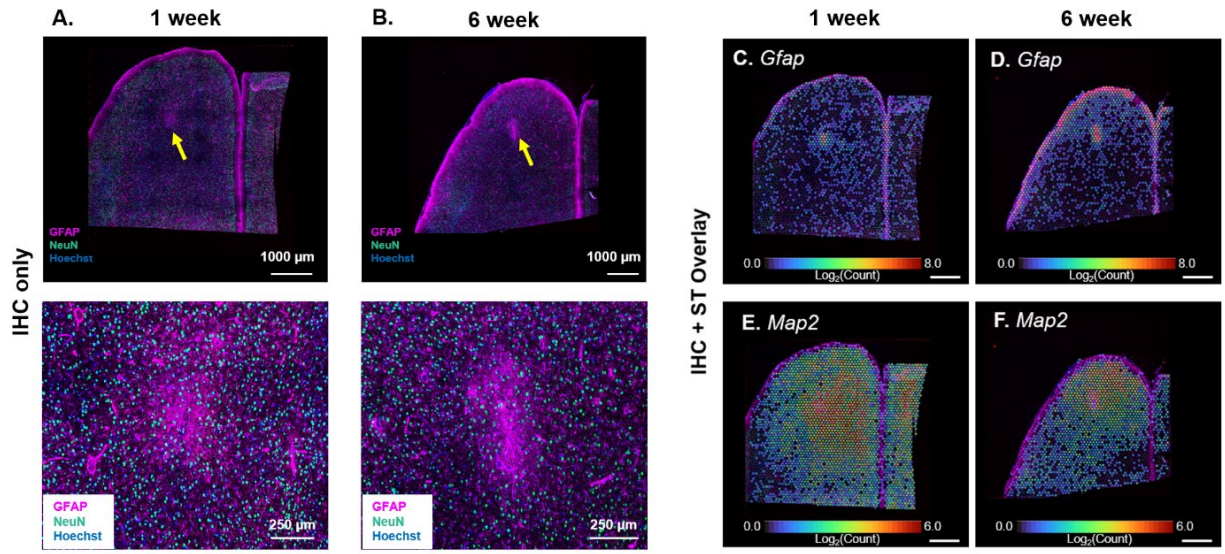


**Figure 4.2.** Immunohistochemistry and spatial transcriptomics of conventional markers of the tissue response around brains implanted electrodes for 1-week and 6-weeks. Representative **A.** 1-week and **B.** 6-week tissue sections immunostained for glial fibrillary protein (GFAP: magenta), neuronal nuclei (NeuN: green) and Hoechst (universal nuclei counterstain: blue). GFAP is highly expressed near at the implant site at both time points, and NeuN expression decreases at 6-weeks. Bottom panels of **A.** and **B.** show closer view of the respective injury site. Representative spatial transcriptomics data overlaid on IHC images to show differential gene expression of *Gfap* and *Map2* at **C, E.** 1-week and **D, F.** 6-week implanted tissue. Scale bars are 1000 µm.

A powerful aspect of the Visium spatial gene expression (10x Genomics) platform is the visualization of gene expression patterns collected by spatially barcoded oligo spots overlaid on conventionally immunostained images. Representative wide-field histological images of 1-week and 6-week tissue sections immunostained for GFAP, NeuN and Hoechst are shown in **Figure 4.2A** and **2B**, with the bottom panel offering a zoomed in view of the respective implant site or device tract. The expression of GFAP, a commonly used glial protein marker to assess tissue response at the device-tissue interface, is increased around and at the implant site in tissue sections of both time points. Similarly, NeuN, a widely employed histological neuronal marker for

investigating brain tissue health, is visually increased at the 1-week time point, but somewhat decreased at the 6-week timepoint in immunostained images. The overlay of spatial transcriptomics on wide-field stained images (**Figure 4.2C-F**) can offer insight into the gene expression patterns of similar conventionally used markers. As shown, *Gfap* differential gene expression at the 1-week time point is upregulated at the implant site, and somewhat spread out within a close (~500 μm) radius surrounding the injury. At the 6-week time point, the *Gfap* gene expression appears more consolidated, possibly indicative of a glial encapsulation of the device facilitated by the chronic foreign body reaction. Gene expression of microtubule-associated protein 2 (*Map2*) can be used as a marker for neuronal cells[37], especially due to its involvement in microtubule stabilization and crosslinking to maintain neuronal structure, function and development. In the 1-week timepoint, gene expression on *Map2* is upregulated and more widespread across the tissue section, surrounding the device tract. Meanwhile, the extent of *Map2* gene expression appears decreased around the implanted site in the 6-week timepoint, potentially supporting previously reported neuronal density reduction or loss around chronically implanted devices.

Manual selections of the spatially mapped regions of the ST tissue sections are possible via the analysis software LoupeBroswer (10x Genomics), enabling investigations of groups of DEGs at selected locations within and between tissue samples. Assessments of various areas in the tissue samples were carried out between sections as well as within tissue sections at each timepoint. Groups, or clusters, were generated by manually selecting regions in tissue sections for differential expression analysis via LoupeBrowser (10x Genomics). Novel significantly upregulated and/or downregulated genes were found in lists of DEGs generated for: (1) near implant site (< ~300 μm) comparisons between 1-week and 6-week tissue (63 significant DEGs); and (2) near (< ~300 μm)

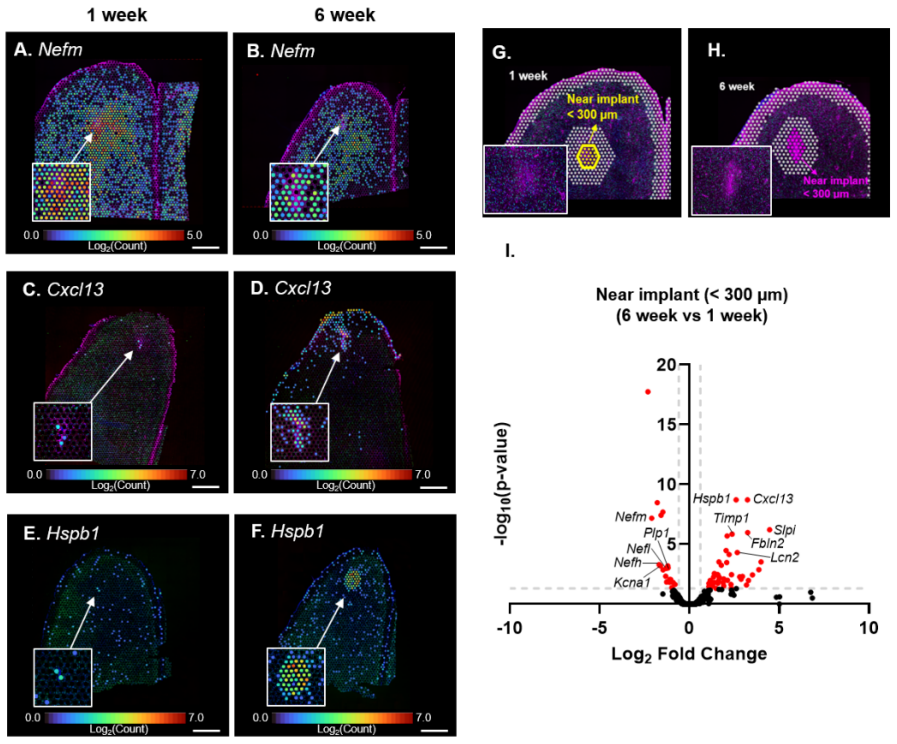


| 6 weeks vs 1 week near implant | |
|---|---|
| Gene Name | $Log_2$ Fold Change |
| | 6 week |
| *ENSRNOG00000068039* | -2.322 |
| ***Cxcl13*** | **3.226** |
| ***Hspb1*** | **2.593** |
| *ENSRNOG00000062930* | -1.796 |
| *AABR07000398.1* | -1.481 |
| *AABR07015057.1* | -1.579 |
| ***Nefm*** | **-2.108** |
| *Slpi* | 4.460 |
| *Fbln2* | 3.235 |
| *Timp1* | 2.377 |
| *Igfbp2* | 2.094 |
| *S100a6* | 2.034 |
| *Lcn2* | 2.665 |
| *Tuba1c* | 2.201 |
| *Fcrl2* | 1.637 |
| *MGC105649* | 3.982 |
| *Cp* | 2.077 |
| *Nefh* | -1.694 |
| *Tspo* | 1.776 |
| *Kcna1* | -1.621 |
| *Pcp4* | -1.211 |
| *Plp1* | -1.197 |
| *Nefl* | -1.293 |
| *Ccl6* | 3.867 |
| *Ermn* | -1.473 |
| *C1qc* | 1.379 |
| *RT1-CE16* | 1.548 |
| *Hbb* | 2.343 |
| *S100a9* | 3.505 |
| *Vim* | 1.584 |
| *Tmeff1* | -1.323 |
| *S100a8* | 2.947 |
| *Srgn* | 2.795 |
| *Chi3l1* | 1.337 |
| *Clec2g* | 1.664 |
| *Gmfg* | 1.907 |
| *Ccl2* | 2.877 |
| *Pclo* | -1.102 |
| *Ina* | -1.050 |
| *Arhgap5* | -1.056 |

**Figure 4.3.** Differentially expressed genes (DEGs) near the 6-week implant site relative to near the 1-week implant site. **A, C, E.** Visualization of gene expression of specific genes differentially expressed at the 1-week tissue section compared to the same genes differentially expressed in **B, D, F** 6-week tissue sections. Near sites were manually selected to compare regions in **G.** 1-week tissue sections (yellow spots), and **H.** 6-week tissue sections (pink spots). Near- regions were kept < ~300 µm around the center of the device. **I.** All DEGs (total: 1789 genes, singificant: 63 genes) can be seen on the I. volcano plot, while the the top 40 DEGS are listed in the table on the right. Significance $p$-value < 0.05, total $n$ = 10 rats ($n$ = 5 rats per time point). Scale bars are 1000 µm.

implant vs far (> ~500 µm) from implant comparisons within 1-week (25 significant DEGs), and 6-week (151 significant DEGs) tissue samples. In the results reported here, each timepoint (1-week or 6-weeks) contained tissue sections from $n$ = 5 implanted rats. Specific significant DEGs are discussed based on publicly available gene databases[38,39], and previously known associations of cellular expression and interactions.

#### 4.3.2.1 NEAR IMPLANT SITE COMPARISONS BETWEEN 1-WEEK AND 6-WEEK TISSUE

Differential expression analysis of near implant sites (< ~300 μm, manually selected as shown in **Figure 4.3G,H**) between 1-week and 6-week tissue samples revealed 63 significant DEGs (*p*adj-value < 0.05). **Figure 4.3A-F** show the spatial gene expression overlaid on IHC images for the known top three significant DEGs. The volcano plot (**Figure 4.3I**), accompanied by a list of top 40 significant DEGs, reports the differential expression analysis of near 6-week implants relative to 1-week implants. Neurofilament medium chain (*Nefm*) is significantly downregulated (*Nefm*; LFC: -2.108, *p*-value: 6.63E−08) at 6-weeks relative to 1-week near the implant. *Nefm* is a protein encoding gene for neurofilament involved in maintaining neuronal structure integrity. This gene along with other similar filament protein encoding genes, *Nefl* and *Nefh*, appear to be significantly downregulated at 6-weeks near implant. Increased expressions of these proteins have been related to neuronal damage[40], suggesting that down-regulation at 6-weeks may be indicative controlled damage and/or neuronal structural changes. This follows previous findings suggesting a decrease in neuronal and neuron function associated genes near chronic implants. An interesting finding is the high upregulation of the B lymphocyte chemoattractant Cxcl13 (*Cxcl13*; LFC: +3.225, *p*-value: 1.93E−09) near implant sites in 6-week tissue compared to 1-week. This gene encodes for a chemokine (signaling proteins secreted by cells involved in the immune system to direct movement of other cells) to specifically attract B cells that are part of the adaptive immune system, and been suggested as a therapeutic target involved in central nervous system disorders[41]. Elevated expressions of this gene, linked to mediating glial activation and neuropathic pain[42], suggest a shift to tissue maintenance and immune defense at 6-weeks compared to 1-week near the implant. The consolidated upregulation of Heat Shock Protein Family B (Small)

Member 1 (*Hspb1*; LFC: +2.593, *p*-value: 1.93E−09) near the implant of the representative 6-week section (**Figure 4.3F**) is another interesting finding, as this gene is expressed under environmental stress conditions to maintain cellular protein homeostasis and cell survival[43]. Overall, while the spatial extent and expression of some genes (*Gfap*, *Nefm*, *Map2*) seem more widespread in the tissue sections at the 1-week implant, these results (evident in **Figure 4.3I**) suggest that more genes, with various functions, are upregulated and consolidated near the implant at 6-weeks relative to 1-week.

#### 4.3.2.2 NEAR IMPLANT VS. FAR FROM IMPLANT SITE COMPARISONS WITHIN 1-WEEK AND 6-WEEK TISSUE

Differential expression analysis within tissue sections for near (< ~300 µm) vs far (> ~500 µm) from the implant site revealed (1) 25 significant DEGs (*p*adj-value < 0.05) in 1-week tissue sections; and (2) 151 significant DEGs (*p*adj-value < 0.05) in 6-week implants. Near implant sites (< ~300 µm) were kept consistent, while far from implant regions were selected as the area surrounding the implant > ~500 µm from the device tract as shown in **Figure 4.4D**. The area around the device selected as the far region was kept within a < 2 mm radius from the device tract in order to minimize whole-tissue effects that may include cellular processes prominent in other brain regions. In 1-week tissue sections, high upregulation of Secreted Phosphoprotein1 (**Figure 4.4B**, *Spp1*; LFC +8.380, *p*-value:1.60E−25) is prominent near the implant site compared to far regions. *Spp1* expression has been related to cytokine activity to mediate cell signaling in the immune system, indicating that the tissue response in these sections may be more inflammation focused. Interestingly, disease associated microglia expressing *Spp1* have been shown to ultimately be removed from the injured brain[44]. *Spp1* is also significantly upregulated (*Spp1*; LFC

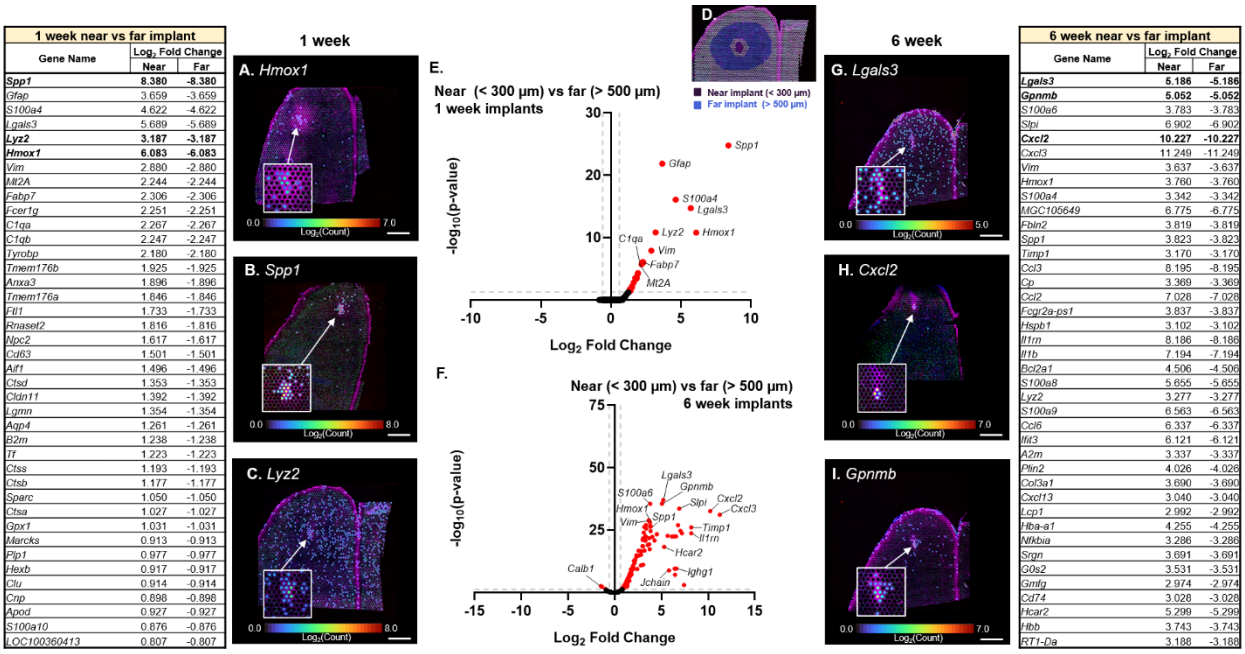


| 1 week near vs far implant | | |
|---|---|---|
| Gene Name | Log2 Fold Change | |
| | Near | Far |
| ***Spp1*** | **8.380** | **-8.380** |
| *Gfap* | 3.659 | -3.659 |
| *S100a4* | 4.622 | -4.622 |
| *Lgals3* | 5.689 | -5.689 |
| ***Lyz2*** | **3.187** | **-3.187** |
| ***Hmox1*** | **6.083** | **-6.083** |
| *Vim* | 2.880 | -2.880 |
| *Mt2A* | 2.244 | -2.244 |
| *Fabp7* | 2.306 | -2.306 |
| *Fcer1g* | 2.251 | -2.251 |
| *C1qa* | 2.267 | -2.267 |
| *C1qb* | 2.247 | -2.247 |
| *Tyrobp* | 2.180 | -2.180 |
| *Tmem176b* | 1.925 | -1.925 |
| *Anxa3* | 1.896 | -1.896 |
| *Tmem176a* | 1.846 | -1.846 |
| *Ftl1* | 1.733 | -1.733 |
| *Rnaset2* | 1.816 | -1.816 |
| *Npc2* | 1.617 | -1.617 |
| *Cd63* | 1.501 | -1.501 |
| *Aif1* | 1.496 | -1.496 |
| *Ctsd* | 1.353 | -1.353 |
| *Cldn11* | 1.392 | -1.392 |
| *Lgmn* | 1.354 | -1.354 |
| *Aqp4* | 1.261 | -1.261 |
| *B2m* | 1.238 | -1.238 |
| *Tf* | 1.223 | -1.223 |
| *Ctss* | 1.193 | -1.193 |
| *Ctsb* | 1.177 | -1.177 |
| *Sparc* | 1.050 | -1.050 |
| *Ctsa* | 1.027 | -1.027 |
| *Gpx1* | 1.031 | -1.031 |
| *Marcks* | 0.913 | -0.913 |
| *Plp1* | 0.977 | -0.977 |
| *Hexb* | 0.917 | -0.917 |
| *Clu* | 0.914 | -0.914 |
| *Cnp* | 0.898 | -0.898 |
| *Apod* | 0.927 | -0.927 |
| *S100a10* | 0.876 | -0.876 |
| *LOC100360413* | 0.807 | -0.807 |

| 6 week near vs far implant | | |
|---|---|---|
| Gene Name | Log2 Fold Change | |
| | Near | Far |
| ***Lgals3*** | **5.186** | **-5.186** |
| ***Gpnmb*** | **5.052** | **-5.052** |
| *S100a6* | 3.783 | -3.783 |
| *Slpi* | 6.902 | -6.902 |
| ***Cxcl2*** | **10.227** | **-10.227** |
| *Cxcl3* | 11.249 | -11.249 |
| *Vim* | 3.637 | -3.637 |
| *Hmox1* | 3.760 | -3.760 |
| *S100a4* | 3.342 | -3.342 |
| *MGC105649* | 6.775 | -6.775 |
| *Fbln2* | 3.819 | -3.819 |
| *Spp1* | 3.823 | -3.823 |
| *Timp1* | 3.170 | -3.170 |
| *Ccl3* | 8.195 | -8.195 |
| *Cp* | 3.369 | -3.369 |
| *Ccl2* | 7.028 | -7.028 |
| *Fcgr2a-ps1* | 3.837 | -3.837 |
| *Hspb1* | 3.102 | -3.102 |
| *Il1rn* | 8.186 | -8.186 |
| *Il1b* | 7.194 | -7.194 |
| *Bcl2a1* | 4.506 | -4.506 |
| *S100a8* | 5.655 | -5.655 |
| *Lyz2* | 3.277 | -3.277 |
| *S100a9* | 6.563 | -6.563 |
| *Ccl6* | 6.337 | -6.337 |
| *Ifit3* | 6.121 | -6.121 |
| *A2m* | 3.337 | -3.337 |
| *Plin2* | 4.026 | -4.026 |
| *Col3a1* | 3.690 | -3.690 |
| *Cxcl13* | 3.040 | -3.040 |
| *Lcp1* | 2.992 | -2.992 |
| *Hba-a1* | 4.255 | -4.255 |
| *Nfkbia* | 3.286 | -3.286 |
| *Srgn* | 3.691 | -3.691 |
| *G0s2* | 3.531 | -3.531 |
| *Gmfg* | 2.974 | -2.974 |
| *Cd74* | 3.028 | -3.028 |
| *Hcar2* | 5.299 | -5.299 |
| *Hbb* | 3.743 | -3.743 |
| *RT1-Da* | 3.188 | -3.188 |

**Figure 4.4.** Differentially expressed genes (DEGs) near relative to far from the implant for 1-week implanted tissue and 6-week implanted tissue. Spatial transcriptomics revealing highly upregulated genes near vs far regions in **A, B, C.** 1-week implanted tissue, and **G, H, I.** 6-week implanted tissue. D. Respresentative image of manually selected near vs far regions in a spatial transcriptomics tissue section. Total DEGs were reduced **E.** near the 1-week implant (total: 991 genes, singificant: 25 genes), and increased **F.** near the 6-week implant (total: 1829 genes, signficant: 151 genes). Lists of top 40 DEGs for each time point are shown in tables. Significance $p$-value < 0.05, total $n$ = 10 rats ($n$ = 5 rats per time point). Scale bars are 1000 µm.

+3.823, $p$-value:4.96E−27) within 6-week tissue sections, presenting maintained expression in the foreign body response to implanted electrodes. Similarly, upregulated gene expression of Heme Oxygenase 1 (**Figure 4.4A**, *Hmox1*; LFC +6.083, $p$-value:1.58E−11) has been related to the adaptive immune response, protecting cells in stress conditions including oxidative stress and hypoxia[45]. Gene expression of *Hmox1* is also significantly upregulated at near implant sites vs far regions in 6-week tissue sections (*Hmox1*; LFC +3.760, $p$-value:7.06E−29) reflecting that expression levels of some genes are maintained to a certain degree across acute and chronic phases of the tissue response. Another immune-system related gene encoding for Lysozyme 2 **(Figure 4.4C**, *Lyz2*; LFC +3.187, $p$-value:1.436E−11), crucial for microbial defense and innate immune

response[46], is upregulated near the implant compared to far regions in 1-week tissue sections as well as within 6-week tissue sections (*Lyz2*; LFC +3.277, *p*-value:2.756E−23). Meanwhile, significant upregulation of an apoptosis regulating gene encoding for Galectin-3[47] (*Lgals*; LFC: +5.689, *p*-value:1.82E−15 at 1-week, and LFC: +5.186, *p*-value: 9.20E−38 at 6-weeks, **Figure 4.4G**) is evident near the implant compared to far regions within both 1-week and 6-week tissue sections. *Lgals3* is involved in the innate immune response as well as inhibition of apoptosis, and abnormal expression of *Lgals3* is associated with certain cancers and inflammatory diseases[48,49]. Similarly, *S100a4* (and other *S100a* family genes), encoding for calcium-binding protein A4 is also involved in regulating apoptosis, and irregular expressions of this gene have been related to cancer[50]. This gene is significantly upregulated near the device site within 1-week and 6-week samples (*S100a4*; LFC: +4.622, *p*-value:8.19E−17 at 1-week, and LFC: +3.342, *p*-value:9.621E−28 at 6-weeks). Significant upregulation of Glycoprotein NMB encoding gene (**Figure 4.4I**, *Gpnmb*; LFC: 5.052, *p*-value:2.50E−36) is present near implant sites within 6-week samples, but not within 1-week tissue sections. *Gpnmb* is expressed in immune cells regulating the immune response, and overexpression of this gene has also been linked to various cancers, potentially playing an immunosuppressive role[51]. Corresponding to the differential expression results of near implant 6-week vs 1-week tissue section, a subset of genes encoding for chemokines (**Figure 4.4H**, *Cxcl2*; LFC: +10.227, *p*-value:2.51E−33, *Cxcl3;* LFC: +11.249, *p*-value: 6.67E−32, *Ccl3;* LFC: +8.195, *p*-value: 8.28E−27, and *Ccl2;* LFC: +7.028, *p*-value: 2.00E−25) are significantly upregulated near the device site within 6-week tissue samples, that are not significantly present near the injury within 1-week tissue sections. This is an interesting finding potentially indicative of a chronic FBR, inducing a migration of immune cells, to the device tract, that is not present during the acute response. Overall, these results support that more genes are

significantly upregulated and consolidated near the 6-week implant site than previously reported, while within 1-week tissue sections had relatively less genes (25 significant DEGs) near vs far from the implant site indicating a more widespread tissue response. Further, the chronic tissue response, near 6-week implants, showed high upregulation of apoptosis and cancer-related genes as well as a subset of genes encoding for chemokines specifically. The trend of numerous upregulated genes, with an absence of downregulated genes, is curious and notable in the volcano plots (**Figure 4.4E**,**F**) visualizing all DEGs near vs far from implant site regions within 1-week and 6-weeks tissue sections. These findings also suggest that certain genes, or groups of genes, may be employing related mechanisms of expression, and an analysis of these connections may uncover novel markers indicative of the tissue response to implanted electrodes.

## 4.4 CONCLUSION

This study extends previous RNA-sequencing results published by our research group by employing a larger dataset and focused comparisons of 1-week vs 6-week implanted tissue sections. Here, it was found that a greater number of genes is upregulated at 6-weeks near the device implant compared to 1-week, and that certain types of genes, or subsets of genes, might be upregulated or downregulated in a similar fashion, demonstrating the need for more sophisticated analysis of these large datasets. The newer technique of spatial transcriptomics employed here provides the advantages of (1) near-cellular scale resolution of the whole-transcriptome profile of genes over the whole-tissue section, (2) improved RNA-quality by employing fresh-frozen tissue and PBS-perfused brains, and (3) combination of immunohistochemistry and spatial transcriptomics in the same tissue section to relate conventional protein markers and gene expression changes.

At the same time, certain limitations exist in the results reported here which should be considered for future experiments and analyses. This dataset can be extended to include a naïve, not-implanted sample (or the preliminary naïve sample collected by Whitsitt et al. 2021[21]), which could present added information on baseline gene expression results and comparisons. Further, manual selection of near vs far regions in tissue sections is a first and convenient approach to run initial differential expression analysis as done in this study; however, more sophisticated computational approaches could better analyze this data with added uniformity of tissue region selections (discussed further in Chapter 5 of this dissertation). Far regions could be prone to including genes, or groups of genes, predominantly expressed in other brain regions, thereby complicating results.

Future work to expand and accurately present this data is discussed in Chapter 5 of this dissertation. Briefly, this dataset along with previous similar RNA-seq data can be analyzed together to produce a more robust sample set, and train or assess the performance of novel computational models adopting network analysis of the data. Gene ontology (GO) analyses of the DEGs generated here could further reveal highly enriched GO terms and active biological processes involved.

## REFERENCES


(1) Willsey, M. S.; Shah, N. P.; Avansino, D. T.; Hahn, N. V.; Jamiolkowski, R. M.; Kamdar, F. B.; Hochberg, L. R.; Willett, F. R.; Henderson, J. M. A High-Performance Brain–Computer Interface for Finger Decoding and Quadcopter Game Control in an Individual with Paralysis. *Nat Med* **2025**, *31* (1), 96–104. https://doi.org/10.1038/s41591-024-03341-8.

(2) BrainGate Trials. Publications. *https://www.braingate.org/publications/* (2025).

(3) Quinn, E. J.; Blumenfeld, Z.; Velisar, A.; Koop, M. M.; Shreve, L. A.; Trager, M. H.; Hill, B. C.; Kilbane, C.; Henderson, J. M.; Brontë-Stewart, H. Beta Oscillations in Freely Moving Parkinson's Subjects Are Attenuated during Deep Brain Stimulation. *Mov Disord* **2015**, *30* (13), 1750–1758. https://doi.org/10.1002/mds.26376.

(4) Nijhuis, H. J. A.; Hofsté, W.-J.; Krabbenbos, I. P.; Dietz, B. E.; Mugan, D.; Huygen, F. First Report on Real-World Outcomes with Evoked Compound Action Potential (ECAP)-Controlled Closed-Loop Spinal Cord Stimulation for Treatment of Chronic Pain. *Pain Ther* **2023**, *12* (5), 1221–1233. https://doi.org/10.1007/s40122-023-00540-y.

(5) Collinger, J. L.; Wodlinger, B.; Downey, J. E.; Wang, W.; Tyler-Kabara, E. C.; Weber, D. J.; McMorland, A. J. C.; Velliste, M.; Boninger, M. L.; Schwartz, A. B. High-Performance Neuroprosthetic Control by an Individual with Tetraplegia. *Lancet* **2013**, *381* (9866), 557–564. https://doi.org/10.1016/S0140-6736(12)61816-9.

(6) Yin, Z.; Jiang, Y.; Merk, T.; Neumann, W.-J.; Ma, R.; An, Q.; Bai, Y.; Zhao, B.; Xu, Y.; Fan, H.; Zhang, Q.; Qin, G.; Zhang, N.; Ma, J.; Zhang, H.; Liu, H.; Shi, L.; Yang, A.; Meng, F.; Zhu, G.; Zhang, J. Pallidal Activities during Sleep and Sleep Decoding in Dystonia, Huntington's, and Parkinson's Disease. *Neurobiol Dis* **2023**, *182*, 106143. https://doi.org/10.1016/j.nbd.2023.106143.

(7) Evangelisti, S.; Boessenkool, S.; Pflanz, C. P.; Basting, R.; Betts, J. F.; Jenkinson, M.; Clare, S.; Muhammed, K.; LeHeron, C.; Armstrong, R.; Klein, J. C.; Husain, M.; Nemeth, A. H.; Hu, M. T.; Douaud, G. Subthalamic Nucleus Shows Opposite Functional Connectivity Pattern in Huntington's and Parkinson's Disease. *Brain Commun* **2023**, *5* (6). https://doi.org/10.1093/braincomms/fcad282.

(8) Chestek, C. A.; Gilja, V.; Nuyujukian, P.; Foster, J. D.; Fan, J. M.; Kaufman, M. T.; Churchland, M. M.; Rivera-Alvidrez, Z.; Cunningham, J. P.; Ryu, S. I.; Shenoy, K. V. Long-Term Stability of Neural Prosthetic Control Signals from Silicon Cortical Arrays in Rhesus Macaque Motor Cortex. *J Neural Eng* **2011**, *8* (4). https://doi.org/10.1088/1741-2560/8/4/045005.

(9) Perge, J. A.; Homer, M. L.; Malik, W. Q.; Cash, S.; Eskandar, E.; Friehs, G.; Donoghue, J. P.; Hochberg, L. R. Intra-Day Signal Instabilities Affect Decoding Performance in an Intracortical Neural Interface System. *J Neural Eng* **2013**, *10* (3), 036004. https://doi.org/10.1088/1741-2560/10/3/036004.

(10) Kozai, T. D. Y.; Catt, K.; Li, X.; Gugel, Z. V.; Olafsson, V. T.; Vazquez, A. L.; Cui, X. T. Mechanical Failure Modes of Chronically Implanted Planar Silicon-Based Neural Probes for Laminar Recording. *Biomaterials* **2015**, *37*, 25–39. https://doi.org/10.1016/J.BIOMATERIALS.2014.10.040.

(11) McCreery, D. B.; Agnew, W. F.; Bullara, L. A. The Effects of Prolonged Intracortical Microstimulation on the Excitability of Pyramidal Tract Neurons in the Cat. *Ann Biomed Eng* **2002**, *30* (1), 107–119. https://doi.org/10.1114/1.1430748.

(12) Gupta, B.; Saxena, A.; Perillo, M. L.; Wade-Kleyn, L. C.; Thompson, C. H.; Purcell, E. K. Structural, Functional, and Genetic Changes Surrounding Electrodes Implanted in the Brain. *Acc Chem Res* **2024**, *57* (9), 1346–1359. https://doi.org/10.1021/acs.accounts.4c00057.

(13) Thompson, C. H.; Riggins, T. E.; Patel, P. R.; Chestek, C. A.; Li, W.; Purcell, E. Toward Guiding Principles for the Design of Biologically-Integrated Electrodes for the Central Nervous System. *J Neural Eng* **2020**, *17* (2), 021001. https://doi.org/10.1088/1741-2552/ab7030.

(14) Salatino, J. W.; Ludwig, K. A.; Kozai, T. D. Y.; Purcell, E. K. Glial Responses to Implanted Electrodes in the Brain. *Nat Biomed Eng* **2017**, *1* (11), 862–877. https://doi.org/10.1038/S41551-017-0154-1.

(15) Cabrera, L.; Sadle, C.; Purcell, E. Neuroethical Considerations of High-Density Electrode Arrays. *Nat Biomed Eng* **2019**, *3* (8), 586–589. https://doi.org/10.1038/s41551-019-0407-2.

(16) Grill, W. M. *Signal Considerations for Chronically Implanted Electrodes for Brain Interfacing*; 2008.

(17) Biran, R.; Martin, D. C.; Tresco, P. A. Neuronal Cell Loss Accompanies the Brain Tissue Response to Chronically Implanted Silicon Microelectrode Arrays. *Exp Neurol* **2005**, *195* (1), 115–126. https://doi.org/10.1016/J.EXPNEUROL.2005.04.020.

(18) Michelson, N. J.; Vazquez, A. L.; Eles, J. R.; Salatino, J. W.; Purcell, E. K.; Williams, J. J.; Cui, X. T.; Kozai, T. D. Y. Multi-Scale, Multi-Modal Analysis Uncovers Complex Relationship at the Brain Tissue-Implant Neural Interface: New Emphasis on the Biological Interface. *J Neural Eng* **2018**, *15* (3). https://doi.org/10.1088/1741-2552/AA9DAE.

(19) Marx, V. Method of the Year: Spatially Resolved Transcriptomics. *Nat Methods* **2021**, *18* (1), 9–14. https://doi.org/10.1038/s41592-020-01033-y.

(20) Whitsitt, Q. A.; Koo, B.; Celik, M. E.; Evans, B. M.; Weiland, J. D.; Purcell, E. K. Spatial Transcriptomics as a Novel Approach to Redefine Electrical Stimulation Safety. *Front Neurosci* **2022**, *16*. https://doi.org/10.3389/fnins.2022.937923.

(21) Whitsitt, Q. A.; Patel, B.; Hunt, B.; Purcell, E. K. A Spatial Transcriptomics Study of the Brain-Electrode Interface in Rat Motor Cortex. *bioRxiv* **2021**, 2021.12.03.471147. https://doi.org/10.1101/2021.12.03.471147.

(22) Thompson, C. H.; Evans, B. M.; Zhao, D. X.; Purcell, E. K. Spatiotemporal Expression of RNA-Seq Identified Proteins at the Electrode Interface. *Acta Biomater* **2023**, *164*, 209–222. https://doi.org/10.1016/j.actbio.2023.04.028.

(23) Thompson, C. H.; Saxena, A.; Heelan, N.; Salatino, J.; Purcell, E. K. Spatiotemporal Patterns of Gene Expression around Implanted Silicon Electrode Arrays. *J Neural Eng* **2021**, *18* (4), 045005. https://doi.org/10.1088/1741-2552/abf2e6.

(24) Ereifej, E. S.; Rial, G. M.; Hermann, J. K.; Smith, C. S.; Meade, S. M.; Rayyan, J. M.; Chen, K.; Feng, H.; Capadona, J. R. Implantation of Neural Probes in the Brain Elicits Oxidative Stress. *Front Bioeng Biotechnol* **2018**, *6*. https://doi.org/10.3389/fbioe.2018.00009.

(25) Wellman, S. M.; Li, L.; Yaxiaer, Y.; McNamara, I.; Kozai, T. D. Y. Revealing Spatial and Temporal Patterns of Cell Death, Glial Proliferation, and Blood-Brain Barrier Dysfunction Around Implanted Intracortical Neural Interfaces. *Front Neurosci* **2019**, *13*. https://doi.org/10.3389/fnins.2019.00493.

(26) Golabchi, A.; Wu, B.; Li, X.; Carlisle, D. L.; Kozai, T. D. Y.; Friedlander, R. M.; Cui, X. T. Melatonin Improves Quality and Longevity of Chronic Neural Recording. *Biomaterials* **2018**, *180*, 225–239. https://doi.org/10.1016/j.biomaterials.2018.07.026.

(27) Prasad, A.; Xue, Q.-S.; Dieme, R.; Sankar, V.; Mayrand, R. C.; Nishida, T.; Streit, W. J.; Sanchez, J. C. Abiotic-Biotic Characterization of Pt/Ir Microelectrode Arrays in Chronic Implants. *Front Neuroeng* **2014**, *7*. https://doi.org/10.3389/fneng.2014.00002.

(28) Chen, K.; Wellman, S. M.; Yaxiaer, Y.; Eles, J. R.; Kozai, T. DY. In Vivo Spatiotemporal Patterns of Oligodendrocyte and Myelin Damage at the Neural Electrode Interface. *Biomaterials* **2021**, *268*, 120526. https://doi.org/10.1016/j.biomaterials.2020.120526.

(29) Wellman, S. M.; Guzman, K.; Stieger, K. C.; Brink, L. E.; Sridhar, S.; Dubaniewicz, M. T.; Li, L.; Cambi, F.; Kozai, T. D. Y. Cuprizone-Induced Oligodendrocyte Loss and Demyelination Impairs Recording Performance of Chronically Implanted Neural

Interfaces. *Biomaterials* **2020**, *239*, 119842. https://doi.org/10.1016/j.biomaterials.2020.119842.

(30) Chen, K.; Cambi, F.; Kozai, T. D. Y. Pro-Myelinating Clemastine Administration Improves Recording Performance of Chronically Implanted Microelectrodes and Nearby Neuronal Health. *Biomaterials* **2023**, *301*, 122210. https://doi.org/10.1016/j.biomaterials.2023.122210.

(31) Gregory, B. A.; Thompson, C. H.; Salatino, J. W.; Railing, M. J.; Zimmerman, A. F.; Gupta, B.; Williams, K.; Beatty, J. A.; Cox, C. L.; Purcell, E. K. Structural and Functional Changes of Deep Layer Pyramidal Neurons Surrounding Microelectrode Arrays Implanted in Rat Motor Cortex. *Acta Biomater* **2023**, *168*, 429–439. https://doi.org/10.1016/j.actbio.2023.07.027.

(32) Thompson, C. H.; Saxena, A.; Heelan, N.; Salatino, J.; Purcell, E. K. Spatiotemporal Patterns of Gene Expression around Implanted Silicon Electrode Arrays. *J Neural Eng* **2021**, *18* (4). https://doi.org/10.1088/1741-2552/ABF2E6.

(33) *LoupeBrowser | 10xGenomics*. https://www.10xgenomics.com/support/software/loupe-browser/latest (accessed 2025-04-12).

(34) Whitsitt, Q.; Saxena, A.; Patel, B.; Evans, B. M.; Hunt, B.; Purcell, E. K. Spatial Transcriptomics at the Brain-Electrode Interface in Rat Motor Cortex and the Relationship to Recording Quality. *J Neural Eng* **2024**, *21* (4), 046033. https://doi.org/10.1088/1741-2552/ad5936.

(35) Ludwig, K. A.; Miriani, R. M.; Langhals, N. B.; Joseph, M. D.; Anderson, D. J.; Kipke, D. R. Using a Common Average Reference to Improve Cortical Neuron Recordings From Microelectrode Arrays. *J Neurophysiol* **2009**, *101* (3), 1679–1689. https://doi.org/10.1152/jn.90989.2008.

(36) Patel, P. R.; Welle, E. J.; Letner, J. G.; Shen, H.; Bullard, A. J.; Caldwell, C. M.; Vega-Medina, A.; Richie, J. M.; Thayer, H. E.; Patil, P. G.; Cai, D.; Chestek, C. A. Utah Array Characterization and Histological Analysis of a Multi-Year Implant in Non-Human Primate Motor and Sensory Cortices. *J Neural Eng* **2023**, *20* (1), 014001. https://doi.org/10.1088/1741-2552/acab86.

(37) Soltani, M. H.; Pichardo, R.; Song, Z.; Sangha, N.; Camacho, F.; Satyamoorthy, K.; Sangueza, O. P.; Setaluri, V. Microtubule-Associated Protein 2, a Marker of Neuronal Differentiation, Induces Mitotic Defects, Inhibits Growth of Melanoma Cells, and Predicts Metastatic Potential of Cutaneous Melanoma. *Am J Pathol* **2005**, *166* (6), 1841–1850. https://doi.org/10.1016/S0002-9440(10)62493-5.

(38) *GeneCards: The Human Gene Database*. https://www.genecards.org/ (2025).

(39) Gene | NIH National Library of Medicine.

(40) Gordon, B. A. Neurofilaments in Disease: What Do We Know? *Curr Opin Neurobiol* **2020**, *61*, 105–115. https://doi.org/10.1016/j.conb.2020.02.001.

(41) Irani, D. N. Regulated Production of CXCL13 within the Central Nervous System. *J Clin Cell Immunol* **2016**, *7* (5). https://doi.org/10.4172/2155-9899.1000460.

(42) Wu, X.-B.; Cao, D.-L.; Zhang, X.; Jiang, B.-C.; Zhao, L.-X.; Qian, B.; Gao, Y.-J. CXCL13/CXCR5 Enhances Sodium Channel Nav1.8 Current Density via P38 MAP Kinase in Primary Sensory Neurons Following Inflammatory Pain. *Sci Rep* **2016**, *6* (1), 34836. https://doi.org/10.1038/srep34836.

(43) Singh, M. K.; Shin, Y.; Ju, S.; Han, S.; Choe, W.; Yoon, K.-S.; Kim, S. S.; Kang, I. Heat Shock Response and Heat Shock Proteins: Current Understanding and Future Opportunities in Human Diseases. *Int J Mol Sci* **2024**, *25* (8). https://doi.org/10.3390/ijms25084209.

(44) Lan, Y.; Zhang, X.; Liu, S.; Guo, C.; Jin, Y.; Li, H.; Wang, L.; Zhao, J.; Hao, Y.; Li, Z.; Liu, Z.; Ginhoux, F.; Xie, Q.; Xu, H.; Jia, J.-M.; He, D. Fate Mapping of Spp1 Expression Reveals Age-Dependent Plasticity of Disease-Associated Microglia-like Cells after Brain Injury. *Immunity* **2024**, *57* (2), 349-363.e9. https://doi.org/10.1016/j.immuni.2024.01.008.

(45) Poss, K. D.; Tonegawa, S. Reduced Stress Defense in Heme Oxygenase 1-Deficient Cells. *Proc Natl Acad Sci U S A* **1997**, *94* (20), 10925–10930. https://doi.org/10.1073/pnas.94.20.10925.

(46) Ferraboschi, P.; Ciceri, S.; Grisenti, P. Applications of Lysozyme, an Innate Immune Defense Factor, as an Alternative Antibiotic. *Antibiotics (Basel)* **2021**, *10* (12). https://doi.org/10.3390/antibiotics10121534.

(47) Perillo, N. L.; Pace, K. E.; Seilhamer, J. J.; Baum, L. G. Apoptosis of T Cells Mediated by Galectin-1. *Nature* **1995**, *378* (6558), 736–739. https://doi.org/10.1038/378736a0.

(48) Farhad, M.; Rolig, A. S.; Redmond, W. L. The Role of Galectin-3 in Modulating Tumor Growth and Immunosuppression within the Tumor Microenvironment. *Oncoimmunology* **2018**, *7* (6), e1434467. https://doi.org/10.1080/2162402X.2018.1434467.

(49) Li, C.-H.; Chang, Y.-C.; Chan, M.-H.; Yang, Y.-F.; Liang, S.-M.; Hsiao, M. Galectins in Cancer and the Microenvironment: Functional Roles, Therapeutic Developments, and Perspectives. *Biomedicines* **2021**, *9* (9). https://doi.org/10.3390/biomedicines9091159.

(50) Bresnick, A. R.; Weber, D. J.; Zimmer, D. B. S100 Proteins in Cancer. *Nat Rev Cancer* **2015**, *15* (2), 96–109. https://doi.org/10.1038/nrc3893.

(51) Lazaratos, A.-M.; Annis, M. G.; Siegel, P. M. GPNMB: A Potent Inducer of Immunosuppression in Cancer. *Oncogene* **2022**, *41* (41), 4573–4590. https://doi.org/10.1038/s41388-022-02443-2.

# CHAPTER 5 | CONCLUSIONS AND FUTURE WORK

## 5.1 OVERVIEW

This dissertation adds to the basic science understanding of the biological response to implanted electrodes by uncovering details on two sources contributing to signal instability and device longevity: (1) protein adsorption, commonly termed "biofouling", at the acute microelectrode surface, and (2) cellular encapsulation of chronic devices. The studies described employ a variety of techniques and devices to assess each of these sources from a multifaceted perspective, consistent with the nature of the biological response.

Protein adsorption, or biofouling, was investigated by employing the adsorption dependent technique of fast-scan cyclic voltammetry (FSCV) offering high temporal resolution to study neurotransmitters on a biologically relevant timescale. Benchtop testing and development of a freestanding boron-doped diamond microelectrode (BDDME) was carried out to ultimately assess the electrode as a candidate for chronic biosensing. The results demonstrate that the BDDME provides higher resistance to biofouling in vitro when compared with the current standard carbon fiber electrode (CFME).

Cellular encapsulation and tissue response to chronic silicon Michigan-style microelectrode arrays were studied using extracellular electrophysiology, immunohistochemistry, and the high throughput RNA-sequencing technique of spatial transcriptomics. These experiments were carried out in rats implanted for up to 6 weeks to capture the acute as well as chronic phase of the foreign body response (FBR). Novel insights on specific differentially expressed genes (DEGs) between rats implanted for 1-week and 6-week were uncovered, while overall comparisons supported that a greater number of genes, than previously thought, are consolidated

and upregulated near the implant at 6-weeks. Further, different individual genes, or groups of genes, may be expressing in similar patterns as the tissue response transitions from acute to chronic FBR. These results provide large datasets of genes that can be used for further analysis in computational models.

Together, these findings offer numerous potential avenues to explore in future studies uncovering more details that will add to a greater understanding of the tissue response to implanted electrodes. The implications of these results, and future work based on this foundation, can guide the use of implantable technology in research and clinical settings. Specific developments for next studies are discussed in the following sections, with particular focus on in vivo neurochemical sensing and analyses of collected chronic data.

## 5.2 STRATEGIES TO IMPROVE BDDME PERFORMANCE FOR IN VIVO NEUROCHEMICAL SENSING

Development of the BDDME as chronic sensor requires further work optimizing the device as a sensitive and resilient implant. The freestanding BDDME is advantageous due to its batch fabrication technique, producing numerous devices that are scalable and customizable based on the experiment. Ongoing collaborations with Dr. Wen Li and Fraunhofer USA Center Midwest – Coatings and Diamond Technologies Division are aimed at improving the device based on the assessments provided in this dissertation. Such alterations include redesigning the freestanding BDDME as an array, similar to the Michigan probe, connected to a multi-channel head stage to sample from multiple sites and increase electrochemical detection area at the electrode. Testing with surface treatments, such as polymer poly(3-4,-ethylenedioxythiophene) (PEDOT)[1] often paired with Nafion, could further enhance conductivity and biocompatibility of the electrode.

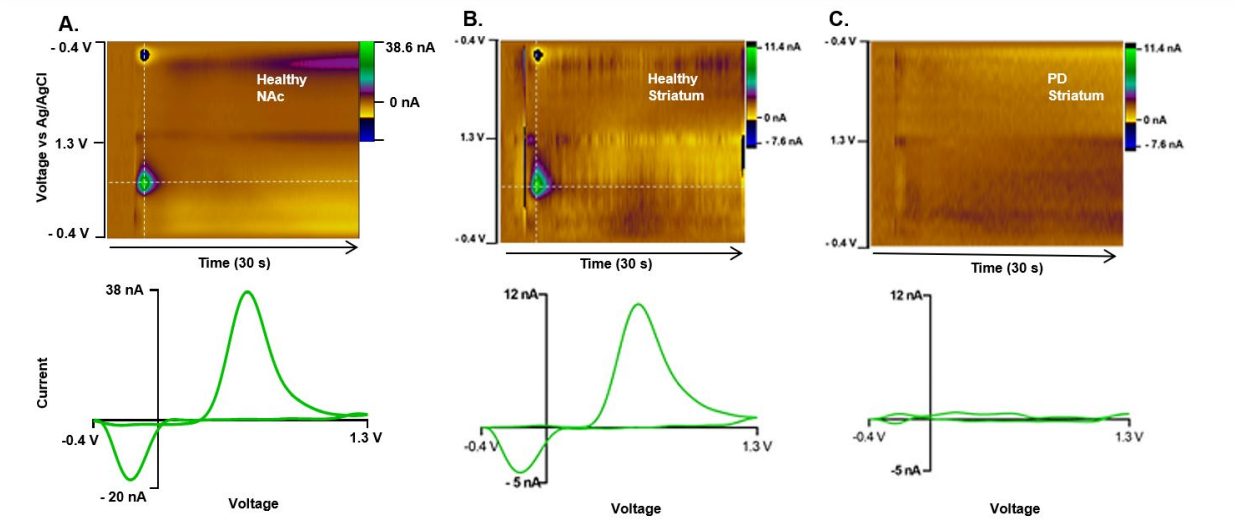


**Figure 5.1.** In vivo detection of stimulation evoked dopamine (DA) in the rat brain using FSCV. **A.** Real-time DA release detected at the CFME implanted in the nucleus accumbens (NAc) in a healthy rat brain. **B.** In vivo DA signal in the healthy striatum of a hemi-parkinsonian model that received 6-hydroxydopamine (6-OHDA) in the contralateral lesioned hemisphere. **C.** Absence of DA detection at the CFME implanted in the diseased hemisphere of the 6-OHDA lesion model. Sitmulation was evoked by placing a stainless steel stimtrode in the medial forebrain bundle in each experiment. The 6-OHDA rat models were provided by Dr. Caryl Sortwell's group at the MSU Grand Rapids Research Center.

Additionally, packaging of the probe to withstand brain micromotion, and bending stiffness assessments could prove especially advantageous for chronic in vivo preparation of the device.

For in vivo neurochemical sensing with FSCV, we have conducted preliminary experiments in a newly setup surgical station for detecting real-time stimulation evoked neurotransmitter release in acute and chronic experiments in the rat brain. **Figure 5.1** provides FSCV data collected in acute experiments (~5-6 hours) to detect dopamine (DA) in healthy and diseased models, such as the hemi-parkinsonian 6-hydroxydopamine (6-OHDA) rat model. While the 6-OHDA lesioned model is useful for studying neurodegenerative conditions, such as Parkinson's disease (PD), newer transgenic models may be more useful in chronic chemical sensing studies. Rapid neurotoxin-induced DA loss can lack the hallmark of misfolded, aggregated

forms of α-synuclein (aSyn) found in the accumulation of Lewy Bodies and Lewy Neurites characterizing PD. A pre-formed fibril (PFF) model, developed by the Sortwell group at the Michigan State University College of Human Medicine campus, more closely mimics the protracted synucleinopathy and neurodegeneration involved in PD[2]. Employing such rat models in future in vivo neurochemical sensing, with the CFME and developed BDDME, will build upon the work presented in this dissertation.

## 5.3 SPATIAL TRANSCRIPTOMICS DATA TO IMPROVE BIOMARKER IDENTIFICATION

Larger datasets with increased sample sizes and a variety of conditions can be analyzed with sophisticated computational methods to develop more meaningful interpretations of novel biomarkers. The results reported in *Chapter 4. Spatial Transcriptomics to Identify Novel Biomarkers at the Brain-Electrode Interface* are a subset of a larger dataset containing RNA-sequencing results using a similar approach. The larger dataset includes added samples of spatial transcriptomics of not implanted, naïve tissue sections, and at tissue collected at the 24-hour timepoint. Studies exploring computational network analyses, such as Differential Co-Expression (DiffCoEx)[3], of spatial transcriptomics data can be carried out to assess the best approach of data handling and revealing biomarkers of interest. Additionally, deeper investigations of cellular and molecular changes and recorded signal quality can provide novel information on the relationship between electrophysiological signals and gene expression at the device-tissue interface. An initial assessment of such interactions has been carried out in a recent report by Whitsitt et al. (2024) to uncover potential mechanisms and biomarkers related to recording quality[4]. Similar computational approaches could be applied to the dataset reported in this work to extend findings of genes strongly related to electrophysiological and histological metrics, uncovering potential biomarkers

associated with recording quality and the biological tissue response. Lastly, gene expression mapping using spatial transcriptomics offered by the Visium platform (10x genomics) has not only provided an initial whole-tissue outlook of the tissue response surrounding implanted electrodes, but also illuminated conditions that could benefit from single-cell resolution techniques for greater accuracy of subcellular level changes in the implanted brain. Future studies exploring device-related or brain region specific effects could be carried out with high-performance in situ analysis, employing single-cell sequencing techniques such as multiplexed error robust in-situ hybridization (MERFISH), or the Xenium platform (10x genomics).

## REFERENCES


(1) Cui, X. & Martin, D. C. Electrochemical deposition and characterization of poly(3,4-ethylenedioxythiophene) on neural microelectrode arrays. *Sens Actuators B Chem* **89**, 92–102 (2003).

(2) Patterson, J. R. *et al.* Time course and magnitude of alpha-synuclein inclusion formation and nigrostriatal degeneration in the rat model of synucleinopathy triggered by intrastriatal α-synuclein preformed fibrils. *Neurobiol Dis* **130**, 104525 (2019).

(3) Moore, M. G., Thompson, C. H., Reimers, M. A. & Purcell, E. K. Differential Co-Expression Analysis of RNA-Seq Data Reveals Novel Potential Biomarkers of Device-Tissue Interaction. in *2022 44th Annual International Conference of the IEEE Engineering in Medicine & Biology Society (EMBC)* 3072–3076 (IEEE, 2022). doi:10.1109/EMBC48229.2022.9871437.

(4) Whitsitt, Q. *et al.* Spatial transcriptomics at the brain-electrode interface in rat motor cortex and the relationship to recording quality. *J Neural Eng* **21**, 046033 (2024).